ACCELERATOR PHYSICS, AND INSTRUMENTATION

OVERVIEW OF THE COUPLED CYCLOTRON PROJECT

Richard C. York, H. Blosser, F. Marti, T. Grimm, H. Laumer, D. Lawton, P. Miller
D. Morrissey, D. Pudvay, B. Sherrill, X. Wu, J. Vincent, A. Zeller

The National Superconducting Cyclotron Laboratory (NSCL) has pursued plans to significantly increase both primary and radioactive beam intensities. By coupling the laboratory's two superconducting cyclotrons (K500 and K1200, $K=EA/q^2$), it will be possible to take advantage of the much greater intensities of the lower charge states from the ion source without sacrificing the final beam energy. Beam from an Electron Cyclotron Resonance (ECR) ion source will be accelerated in the K500 and then transported to the K1200 where it will be stripped to a higher charge state and accelerated to final energy. The primary beam intensities will be increased orders of magnitude to levels of $\leq 10^{13}$ particles/sec. The maximum energy of the heaviest ions will be increased several times relative to the ~30 MeV/u presently available while the maximum energy of the lighter ions ($A \leq$~40) will remain at ≤200 MeV/u. These increases in the primary beam intensities combined with the proposed larger capacity fragment separator will yield radioactive beam intensities a factor of approximately 10^3 greater than presently available at NSCL.

The upgrade will consist of increasing the focusing in the ECR-to-K500 injection channel to maintain beam brightness and intensity, refurbishing the K500 to increase operational reliability, installing a coupling line between the K500 and K1200, installing a stripping foil system in and improving the extraction system of the K1200, and replacing the present A1200 fragment separator with a much higher efficiency device (A1900). Figure 1 shows the present and proposed NSCL accelerator area.

Although the S800 project has been the top laboratory priority after operations, significant progress has been made to the Coupled Cyclotron Project. A proposal was submitted to NSF in the fall of 1994 and received very favorable reviews. In July of 1995, a prestigious, international technical group was impaneled by NSF to review the technical aspects of the proposal and gave both the design and NSCL personnel high marks. The Long Range Plan of the Nuclear Science Advisory Committee specifically identified the NSCL upgrade as a high priority.

A detailed analysis has been done on the ECR to K500 coupling line, the mechanical design completed, and hardware implementation begun. [1] The line will be commissioned during 1996.

A new second harmonic central region was designed, fabricated, and tested in the K500 [2], and simulations to more accurately determine the extracted beam dynamics have been made. [3] In addition, the K500 was operated to experimentally determine certain design assumptions relevant to the Coupled Cyclotron Project [4] and to more clearly identify those systems which will require implementation of the more reliable, K1200-like engineering solutions.

A preliminary prototype of the K1200 stripping foil transport was constructed and successfully tested in the high magnetic field environment of the K500 in the presence of rf. In order to improve the present operational performance as well as to provide a basis for the further improvements necessary for the more intense Coupled Cyclotron Project beams, experiments have been performed on and hardware improvements made to the K1200 extraction system. [5,6] A design analysis has been done for the K500 to K1200 coupling line. [5]

Radioactive beams are created at the NSCL by the technique of in-flight separation. A primary beam is placed on a thin ($\Delta E/E \approx 10\%$) production target. The radioactive species produced have a significant forward momentum and a downstream magnetic chicane is used to select a particular species which is then used to perform nuclear physics experiments. The present fragment separator has a momentum limit of approximately 1.5 GeV/c and a case-specific capture efficiency which is generally a

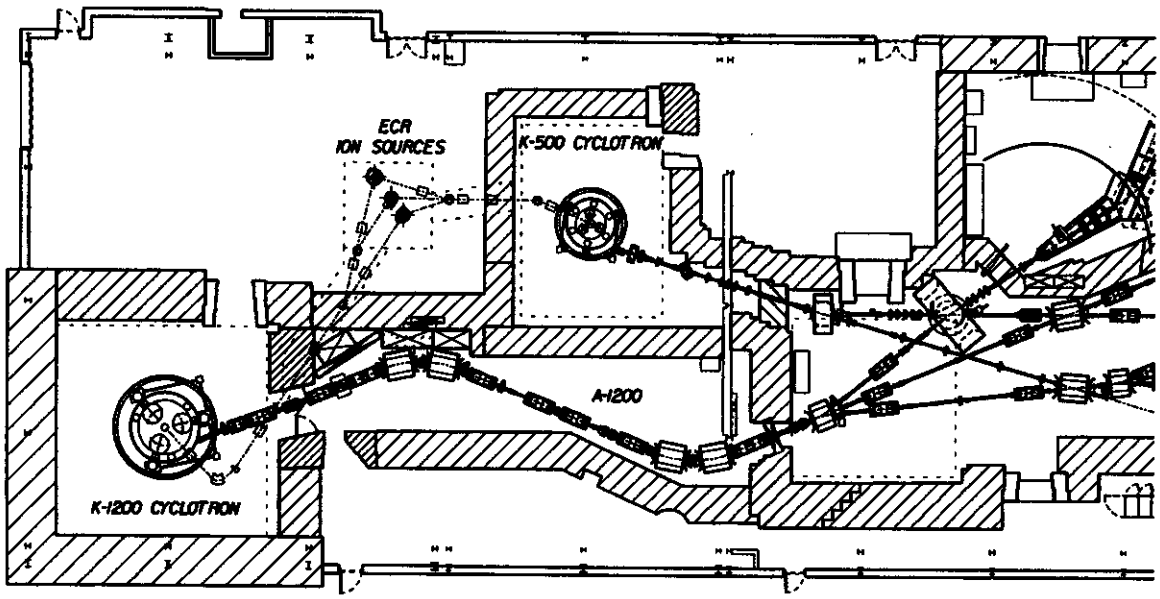

Present Cyclotron Layout

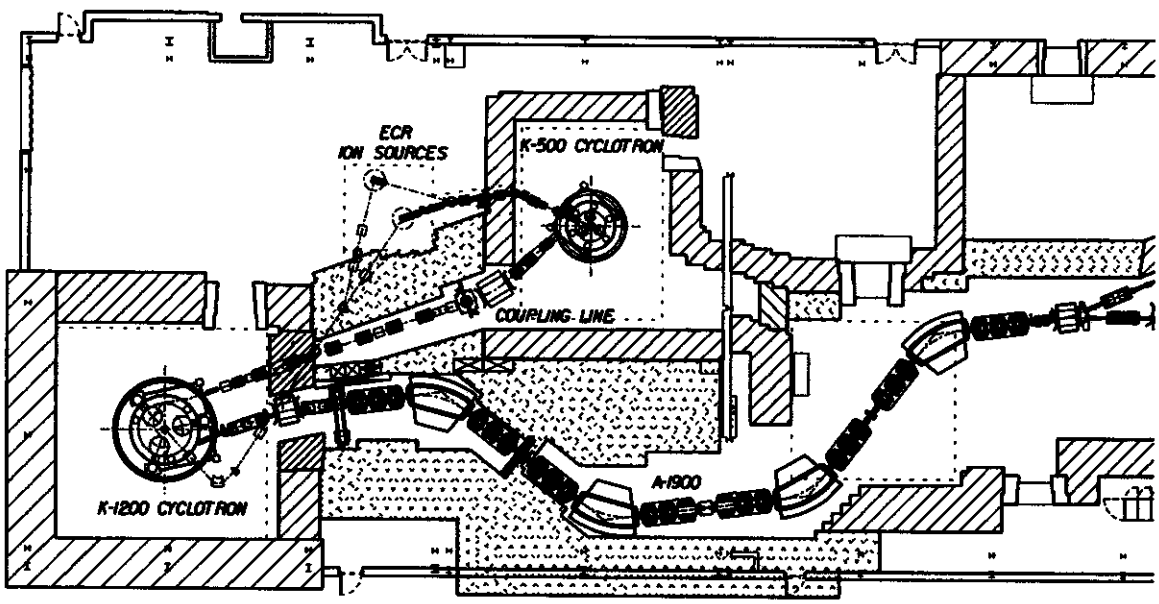

Coupled Cyclotron Layout

Figure 1. Present and proposed NSCL accelerator area layout.

few percent. The upgrade will include a new fragment separator which will have a momentum limit of approximately 1.9 GeV/c and a capture efficiency approaching 100%. The initial proposal specified a magnetic configuration utilizing high field, cos(2θ) quadrupoles. A new lattice has been developed

which will allow the use of quadrupoles of the same type as those developed for the first two elements of S800 spectrometer (Q1/Q2) thereby reducing the possible technical risk while maintaining the system performance parameters. Detailed performance estimates are being determined through particle tracking and engineering designs for the required magnetic elements have been initiated. Prototyping of the A1900 quadrupole package will begin during 1996.

The laboratory cryogenic capacity is in the process of being increased significantly in order to support the increased cryogenic loads of the S800 spectrometer system, to improve laboratory operations reliability by providing a larger cryogenic margin, and to support the anticipated increased heat loads of the proposed new fragment separator. [8]

References

1. X. Wu et al., "ECR-to-K500 Injection Line for Coupled Cyclotron Project", these proceedings.
2. S. Snyder et al., "Calculations and Measurements in the K500 Central Region", these proceedings.
3. F. Marti et al., "K500 Extraction System Studies", these proceedings.
4. T. Grimm et al., "K500 Operation for Coupled Cyclotron Development", these proceedings.
5. D. Pudvay et al., "A Liquid Cooled High Voltage Feedthrough for the K1200 Cyclotron", these proceedings.
6. P. Miller et al., "Electrostatic Deflector Development", these proceedings.
7. X. Wu et al., "K500 to K1200 Coupling Line for Coupled Cyclotron Project", these proceedings.
8. H. Laumer et al., "Cryogenic Upgrade," these proceedings.

K500 TO K1200 COUPLING LINE FOR COUPLED CYCLOTRON PROJECT

X. Wu, D. Lawton, F. Marti, R.C. York and T. Grimm

The K500 to K1200 coupling line is required to transport beams from the extraction port of the K500 cyclotron to the injection port of the K1200 cyclotron for Coupled Cyclotron Project.[1,2] It is to provide matching of the six-dimentional phase space obtained from the K500 to that required for the K1200, and to maintain the beam bunch length while satisfying the geometric constraints of the existing K500 and K1200 configuration. Table I lists the beam parameters for selected primary beams required for the K500 to K1200 coupling line.[3] Fig. 1 shows the detail of the proposed K500 to K1200 coupling line.

Table I. Parameter List for Selected Primary Beams

ION	A	Q	Beam Energy(MeV/u)	Beam Intensity(pnA)
O	16	3	16.7	1,235
Ar	40	7	15.3	745
Kr	84	14	14	202
Xe	129	21	12.9	83
U	238	28	6.9	25

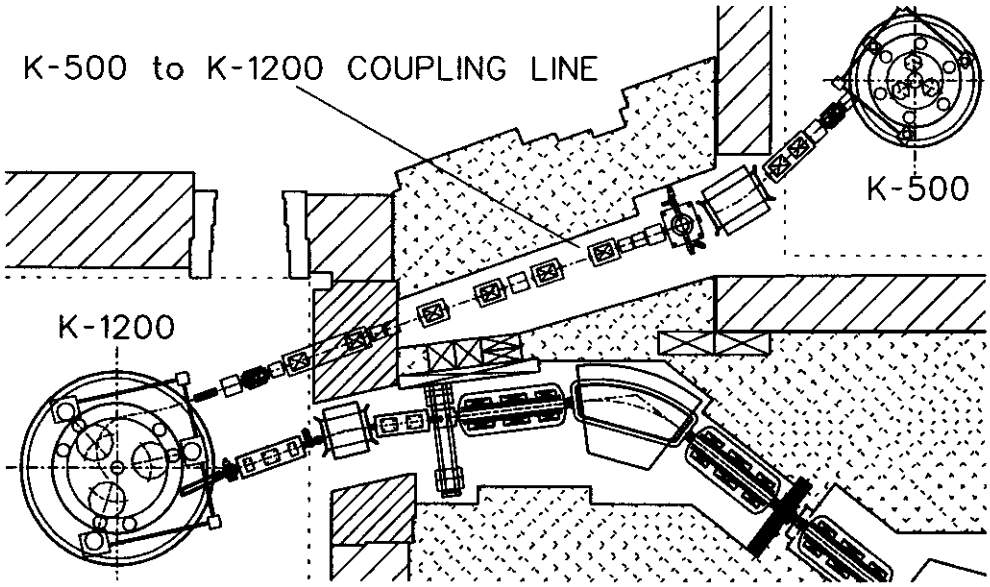

Fig. 1: Proposed K500 to K1200 Coupling Line.

The proposed K500 to K1200 coupling requires that the K500 be rotated 120° clockwise from its present position. Two small dipoles (±1.5°) at either end of system will allow small corrections to the extracted K500 and the injected K1200 trajectories needed to correct for the different magnetic fields and different beam transported. A single large dipole (~20°) is used to properly arrange the horizontal centroid of the beam trajectory between the two cyclotrons. Eight superconducting quadrupoles will be used to accomplish the mapping of the transverse phase space extracted from the K500 to that required for injection into K1200 and provide the beam focusing during the beam transport.

Table II shows the extracted beam parameters from the K500 in Twiss notation. These values are based on a K500 extraction simulation using measured values for the K500 magnetic field.[4] The range of parameters given in the table covers virtually all the extracted phase space from the K500 cyclotron.

Table II. K500 Output Machine Functions.

Beam	β_x (m)	α_x	η_x (m)	η'_x	β_y (m)	α_y	$\eta_y\eta'_y$
1	3.02	-0.1	-10	0.2	13.35	-6.53	0
2	9.55	-2.49	1	2	15.9	-1.04	0
3	8.34	1.34	-14.8	0.2	3.27	-4.61	0
4	8.51	1.61	2	2	9.32	-878	0

Table III shows the machine functions required for injection into the K1200 for selected primary beams, also in the form of Twiss notation. They are given at the matching point, 4.84 m from the position of the stripping foil in the central region of the K1200. These values were derived from the K1200 stripping injection simulation.[5]

Table III. K1200 Input Machine Functions.

Beam	β_x (m)	α_x	η_x (m)	η'_x	β_y (m)	α_y	$\eta_y\eta'_y$
^{16}O	303.4	73.5	-11.7	2.83	5.82	0.82	0
^{40}Ar	258.5	71.1	-11.5	2.72	4.59	1.22	0
^{84}Kr	114.9	27.3	-10.5	2.79	23.27	9.97	0
^{129}Xe	129.7	32.1	-10.5	2.58	18.96	8.11	0
^{238}U	197.9	48.1	-10.9	2.56	10.78	3.83	0

Table IV defines a matrix relationship between the input to coupling line (K500 output - vertical columns) and its output (K1200 input - horizontal rows). The significant differences of dispersions (η_x,η'_x) of the extracted beams from the K500 and machine functions (β_x, α_x, β_y, α_y) of beams required for the K1200 injection increase the difficulty of matching the six-dimensional transverse phase space from the K500 to K1200. The beam extracted from the K500 will have p/q $\leq$ 1 GeV/c and a transverse emittance of $\leq 3\ \pi$ mm-mrad in both planes.

Table IV. Coupling Line Optics Parameter Matrix.

K1200K500	^{16}O	^{40}Ar	^{84}Kr	^{129}Xe	^{238}U
1	CPL11	CPL12	CPL13	CPL14	CPL15
2	CPL21	CPL22	CPL23	CPL24	CPL25
3	CPL31	CPL32	CPL33	CPL34	CPL35
4	CPL41	CPL42	CPL43	CPL44	CPL45

The required quadrupole values (k1 = B_{pole}[kG]/Bρ[kG-m]) are given in Table V for an ^{16}O beam (cases: CPL11, CPL21, CPL31 and CPL41). The required quadrupole values for other beams are similar to that listed in the table. The optics solutions require a field of 6.8 kG for quadrupoles with a radial aperture of 6.35 cm.

Other hardware required in the K500 to K1200 coupling line includes: 6 corrector dipoles to provide central orbit corrections; 4 beam diagnostic boxes consisting of Faraday cups, profile monitors,

bunch length probes and emittance measurement devices to provide adequate beam diagnostics for the coupling operation.

Table V. Coupling Line Optics Parameter Matrix.

CaseQuadrupole	CPL11	CPL21	CPL31	CPL41
QK5F1	1.191	-0.846	0.496	2.978
QK5F2	-1.501	1.863	-0.204	-1.878
QK12F1	0.103	0.343	-0.843	-0.326
QK12F2	-0.162	-0.644	0.044	-0.028
QK12F3	-0.036	-0.175	0.268	0.396
QK12F4	0	0	0	0
QK12F5	-1.712	0.062	-2.329	0.071
QK12F6	1.488	0.781	1.621	0.565

The control of the longitudinal beam bunch length is required because of the correlation of the K1200 extraction efficiency and the beam bunch length. This correlation is uncertain due to model dependent simulation assumptions. Prudent planning dictates the proposed coupling line design using an rf system to control the beam bunch length.

An $^{16}O^{3+}$ beam with current of 1 pμA and energy of 16.7 MeV/u was simulated through the K500 to K1200 coupling line. The beam was assumed to have a FWHM bunch length of ± 1.5° and an initial longitudinal distribution obtained from space charge simulation in the K500. Preliminary simulation results indicate that an rf system working at the 4th harmonic with a peak gap voltage of 193 kV will have a bunch length increase in the coupling line of ≤ 0.1% and an energy spread increase of ≤10 %.

References

1. York, H. Blosser, T. Grimm, D. Lawton, F. Marti, J. Vincent, X. Wu, and A. Zeller, "Proposed Upgrade of NSCL", Proc. of the 1995 Particle Accelerator Conference, (1995)
2. "The K500 K1200 - A Coupled Cyclotron Facility at the National Superconducting Cyclotron Laboratory", July, 1994, Michigan State University, East Lansing, Michigan, MSUCL-939.
3. Wu, "K500 to K1200 Coupling Line", NSF Site Review of K500 K1200 Project, July, 1995, Michigan State University, East Lansing, Michigan.
4. Johnson and F. Marti, "Survey of Beam Dynamics at Extraction in the K500 Cyclotron", NSCL-CCP2-1994 (1994).
5. Johnson and F. Marti, "Survey of Injected Beam parameters at the K1200 Cyclotron", NSCL-CCP6-1995 (1995).

ECR TO K500 INJECTION LINE FOR COUPLED CYCLOTRON PROJECT

X. Wu, D. Lawton, F. Marti, R.C. York and T. Grimm

An element of the Coupled Cyclotron Project (CCP) will be the installation of a new transport system between the ECR's and the K500.[1,2,3] The new injection line will transport beams to the K500 central region, maintain the beam brightness by controlling the space charge effect, and match the transverse phase of the ECR to that required for injection into K500. The design criteria are a rigidity of ≤ 17 MeV/c, Q/A < 0.2, an ECR voltage $V_{ecr} \leq 30$ kV, and a transmission efficiency >50% for a transverse emittance (both planes) $\leq 75\ \pi$ mm-mrad. Table I shows the estimated ECR beam intensities for selected primary beams specific to the CCP.

Table I. Parameter List for Selected Primary Beams

ION	A	Q	Beam Intensity(pmA)
O	16	3	50
Ar	40	7	30
Kr	84	14	8
Xe	129	21	3.2
U	238	28	1

The existing injection line consists of 3 parts, a vertical deflective system used as the mass analysis system, a horizontal segment to transport beam beneath the K500 cyclotron and a final vertical segment to inject the beam into the K500 central region. Fig. 1 shows the layout of existing ECR to K500 injection line. Previously, the injection line was operated at 10 kV. For $^{16}O^{4+}$, transmission efficiencies to the K500 central region of 11 and 75% were achieved for beam intensities of 12 and 1.7 pμA respectively. Improvement in performance is required to achieve the objectives of the Coupled Cyclotron Project.

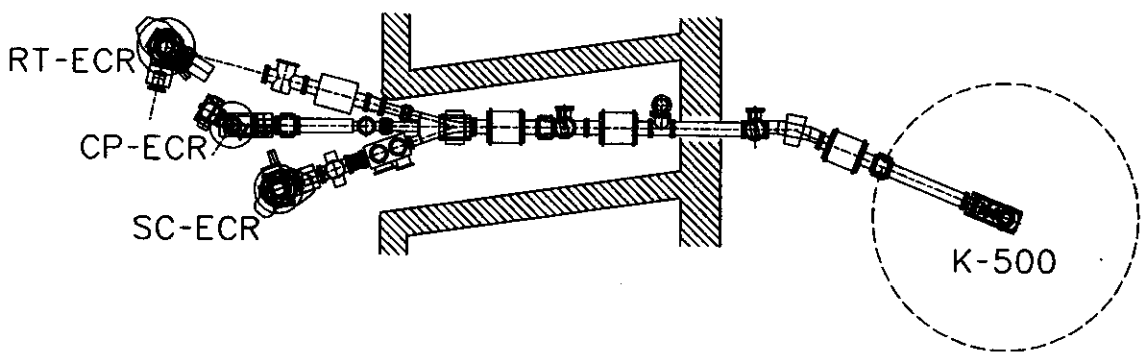

Fig. 1: The Layout of Existing ECR to K500 Injection Line.

The existing injection line was operated between the fall of 1994 and the fall 1995. An $^{16}O^{4+}$ beam at 20 kV was used to perform the injection studies for the Coupled Cyclotron Project. Improvements made to the existing injection line included: installing a new K500 spiral inflector increasing the aperture from 4 mm to 6 mm, adding a new adjustable circular aperture system outside Superconducting ECR to control the beam emittance coming out of the source, and increasing the focusing by using greater capacity solenoid magnet power supplies. As a result, a transmission efficiency to the K500 central region of 90% was achieved for a beam current of 37.5 pμA of $^{16}O^{4+}$ beam with an ECR voltage of 20 kV. This compares favorably with the CCP requirements of a 50% transmission for a beam of 25 pμA.

To further improve the ECR to K500 injection line performance and to support the transport of the CCP higher rigidity beams, a new injection line was designed and is being constructed. Fig. 2 shows the

layout of the new ECR to K500 injection line. The SCECR will remain in its present location and be the primary ion source for K500 injection. The RTECR will be upgraded to High B mode and also used for K500 injection. The major modifications from the existing injection line are in the horizontal segment. New support stands for the beamline elements will be used to provide better beamline alignment control. The focusing will be increased to provide better control of the beam under the influence of space charge forces and to improve transverse phase space matching. An additional solenoid magnet and two electrostatic quadrupole doublets will be added in the horizontal segment of injection line. A new beam diagnostics box will be used to measure the transverse beam emittance in both planes and to monitor the beam spot using a phosphor screen and a TV camera. A rotary wire scanner will also be used to provide beam profile measurement in both planes without interrupting the beam injection to K500. To reduce the influence of the K500 Cyclotron stray magnetic fields on the injection beam, the 90 degree bending magnet beneath the K500 Cyclotron will be replaced by a electrostatic deflector and the horizontal bending magnet will be positioned further away from the K500 Cyclotron at a point inside the wall between ECR and K500 vaults. Magnetic shielding consisting of one inch thick steel plates will also be used to shield the horizontal section of the injection line inside the K500 vault region. In addition, steering magnets, phosphor screens, TV cameras, vacuum gate valves and pumps will also be added to enhance the operation of new ECR to K500 injection line. In order to transport the higher rigidity CCP beams, some of the magnet power supplies will be upgraded.

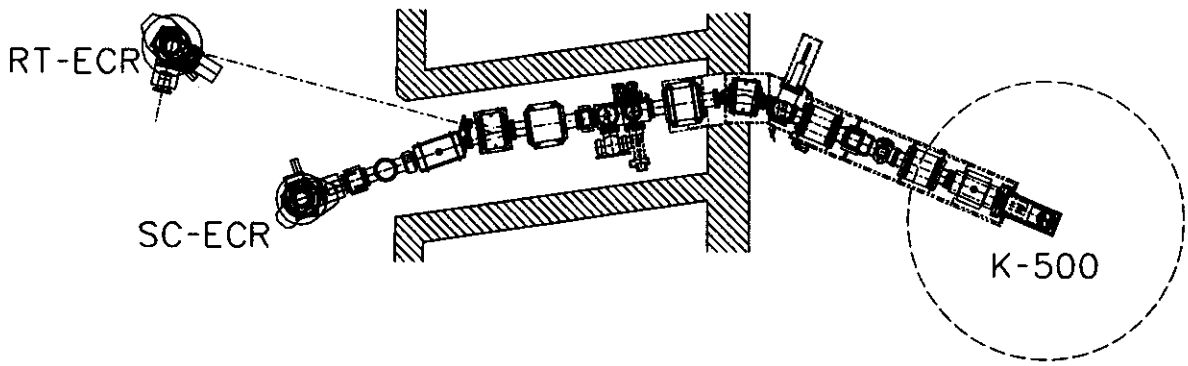

Fig. 2: The Layout of the New ECR to K500 Injection Line.

The physics design for the New ECR to K500 Injection Line was completed in October 1995, and mechanical design and fabrication of the required beamline components was started soon after. The prototype electrostatic quadrupole doublet was fabricated and satisfactorily tested in the existing injection line. Alternative types of phosphor screen materials were also tested to determine those appropriate for this application.

Presently, the major beamline components are being fabricated. The installation of new ECR to K500 injection line will begin in the near future with completion scheduled for summer of 1996.

References

1. R.C. York, H. Blosser, T. Grimm, D. Lawton, F. Marti, J. Vincent, X. Wu, and A. Zeller, "Proposed Upgrade of NSCL", Proc. of the 1995 Particle Accelerator Conference, (1995)
2. "The K500 K1200 - A Coupled Cyclotron Facility at the National Superconducting Cyclotron Laboratory", July, 1994, Michigan State University, East Lansing, Michigan, MSUCL-939.
3. X. Wu, "ECR to K500 Injection Line", NSF Site Review of K500⊗K1200 Project, July, 1995, Michigan State University, East Lansing, Michigan.

PROGRESS ON RADIATION SAFETY ISSUES IN THE COUPLED CYCLOTRON PROJECT

R.M. Ronningen and P. Rossi

Coupled cyclotron project radiation safety issues were presented and discussed in the document covering the project's scientific justification and technical specifications.[1] They were also presented to the NSF's technical review committee, for a site review of the project, in July, 1995. These issues include shielding design, remote handling, local and environmental monitoring, and personnel safety.

In the present annual report, we describe some very recent neutron measurements, which will supplement the earlier data [2], and a report on the status of our air monitoring system. We have previously reported on a neutron activation study of typical facility materials, such as copper, stainless steel, and brass [3]. Below, we describe several other measurements related to the radiation safety issues.

Late in 1994, the failure of a cyclotron deflector, while running an intense, high energy beam, gave us a chance to obtain data to project potential radiation exposures during coupled cyclotron operations. Deflector removal and its repair, are presently the sources of most of the measurable personnel exposure at the NSCL. Shortly after the failure, we measured dose rates of 6 rads per hour at 30 cm from the failed deflector. Beta radiation contributed 87% of the dose, and gamma radiation the remaining 13%. We note that the potential exposure from beta radiation can be significantly reduced by 2 cm of plastic. These data were then extrapolated using the coupled cyclotron design parameters: light ions having 200 MeV/u, 1 particle microampere currents, and 10% beam losses at the deflector. We project dose rates of 13 rad/hr to 32 rad/hr, at 30 cm, depending on how dose scales with beam energy. Our conclusions are that remote handling and radiation work permit policies will be necessary. However, these projections show that conditions for establishing a "Very High Radiation Area," that is, 500 rad or greater, in an hour, at 1 meter, should not exist during coupled cyclotron operations. Similar conclusions are reached for A1900 target handling.

To further address the personnel exposure issue, we have studied the "cool-down" times of beam-irradiated molybdenum and beryllium, materials that are used in the deflector septum, beam probes, and for targets in radioactive beam experiments. It can be shown that [4] the dose rates from cooling samples can be related to the incident beam flux density and the irradiation time by $\frac{dD}{dt} = B\phi \ln(\frac{t_i + t_c}{t_c})$. The constant B depends on the production cross section, beam energy, produced isotopes and their emissions, radiation attenuation factors, and geometry. Here, ϕ is the beam flux density; t_i is the irradiation time and t_c is the cooling time. A thick Mo target was bombarded by a beam of ^{18}O ions, and a thick Be target by ^{12}C ions. Exposure rates as a function of cooling time are shown in Fig. 1 and 2. The curves in these figures are the model predictions. Using cool-down curves, potential exposure rates can be estimated by scaling with beam current and energy.

We are doing measurements to assess the potential for neutron-induced soil activity to leach into the ground water as a result of coupled cyclotron operations. The Analysis Hall is the current site of the A1200 and the proposed future site of the A1900. It is within the NSCL building and is protected from rainwater. The ground water level is at least 25 feet below grade. Presently, during A1200 operations, and even more so during A1900 operations, copious amounts of neutrons are produced at the target chamber and in the A1200's first pair of dipole magnets, where the primary beam is dumped. The floor of the Analysis Hall consists of 20-inch-thick concrete. We have bored a test hole in the floor of the target area. The floor is 49 inches below the target. One cobalt activation foil was placed approximately one inch below floor level, and is covered by a 1.25-inch polyethylene plug. A concrete plug sits below

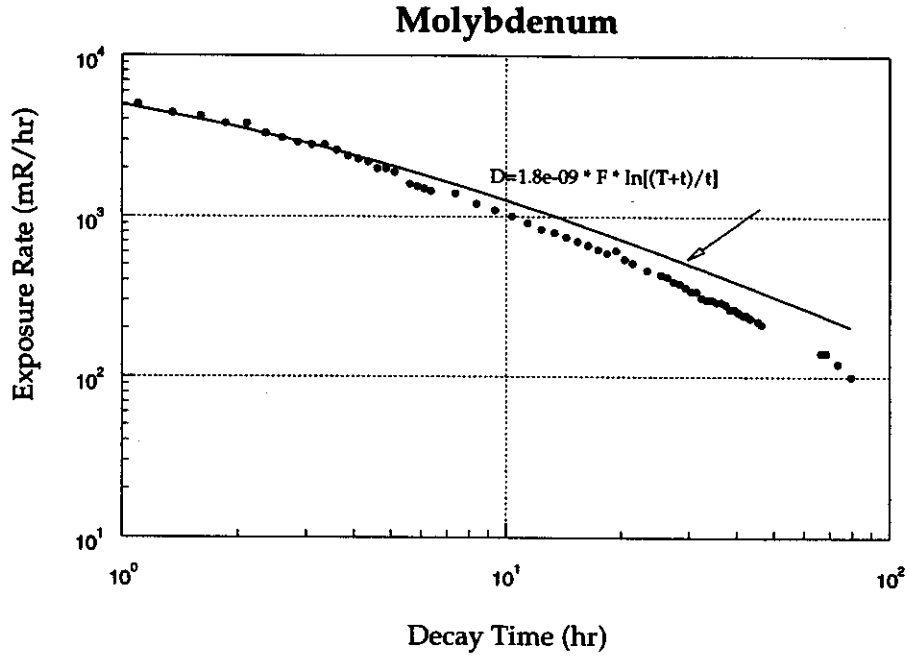

Figure 1: Measured decay of induced activity in a 0.0254 cm-thick molybdenum target irradiated by a ^{18}O beam having an energy of 100 MeV per nucleon. The beam current was about 6.25 particle-nanoamperes. The activity was measured by an ion chamber in near-contact with the target.

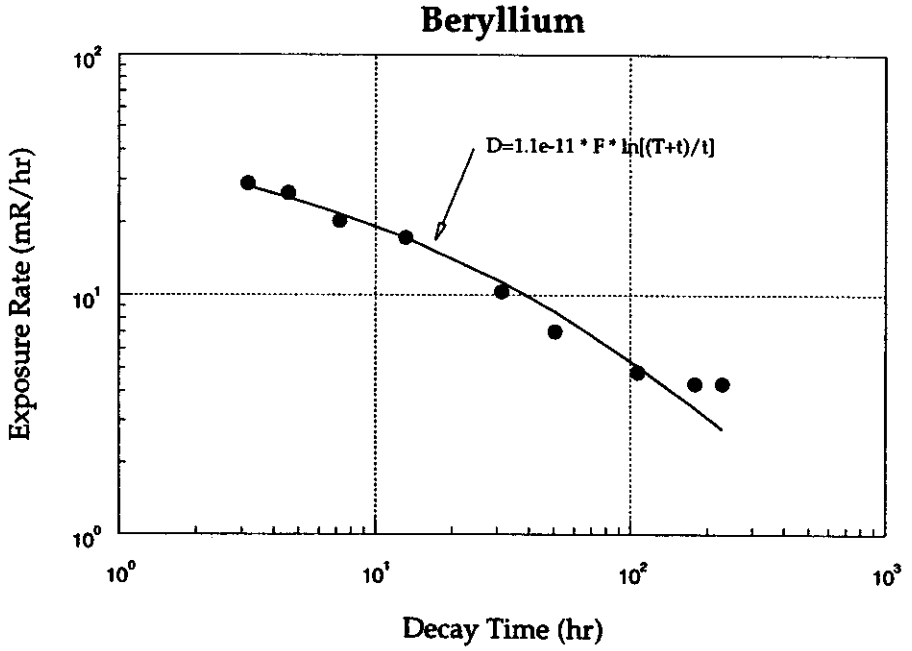

Figure 2: Measured decay of induced activity in a 0.254 cm-thick beryllium target irradiated by a ^{12}C beam having an energy of 60 MeV per nucleon. The beam current was about 50 particle-nanoamperes. The activity was measured by an ion chamber in near-contact with the target.

this foil, to approximate the floor's shielding effect. At the bottom of the plug a second cobalt foil was placed. The foils were purchased commercially, and each has a mass of approximately 35 grams. Figure 3 shows the buildup of activity (from the decay of neutron-induced ^{60}Co) in each foil. The foil at the bottom of the plug contains a smaller amount of activity because it is further away from the target, and because of shielding by the plug. These data will be analyzed to obtain the integrated neutron flux. Knowing flux, soil composition, and water table level should allow us to assess the potential for any soil activity to leach into the ground water.

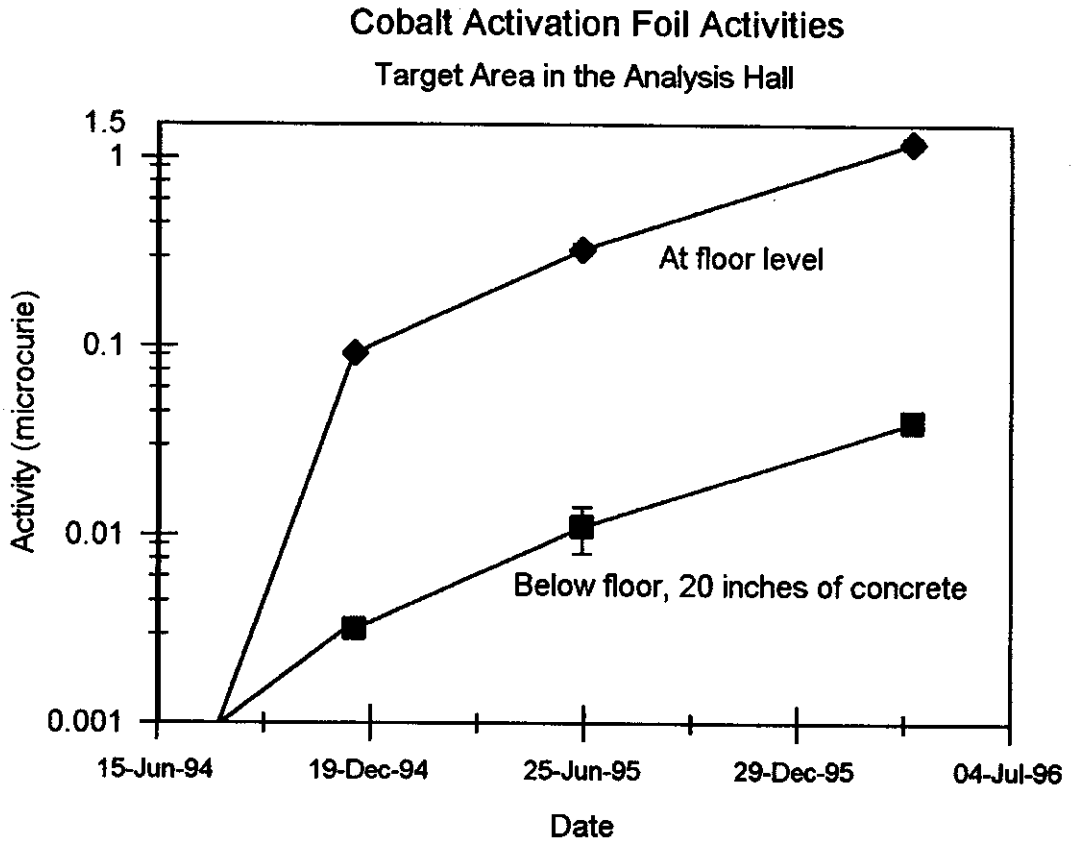

Figure 3: Measured ^{60}Co activities in cobalt activation foils, placed below the A1200 target chamber. One foil sits on the top of a 20-inch concrete plug, and is about 1.25 inches below the floor level. The floor is 49 inches below the target center. The second foil is mounted at the bottom of the concrete plug.

References

1. "The K500⊗K1200, A Coupled Cylotron Facility at the National Superconducting Cyclotron Laboratory, Michigan State University. Scientific Justification and Technical Specifications for a Cost-Effective Upgrade of the NSCL Facility," MSUCL-939, July, 1994.
2. NSCL Annual Report for 1993, page 252.
3. NSCL Annual Report for 1994, page 193.

AN ION CYCLOTRON RESONANCE ACCELERATOR

Chris Ramsell, Terry Grimm, and Richard York

This paper describes progress made in the computational study of a novel ion accelerator. The accelerator concept is based on the operating principles of cyclotrons and gyrotrons, and we use the name Ion Cyclotron Resonance Accelerator (ICRA). The ICRA promises to provide a compact, high efficiency accelerator capable of providing ion beam energies of tens of MeV and currents of hundreds of microamps. Ion energies and intensities in this regime have many applications including isotope production for radiopharmecuticals [1], production of neutron beams [2], and analysis and modification of materials [3]. Today ion beams below a few MeV are typically produced by electrostatic generators and above a few MeV by either linacs or cyclotrons. Due to the simplicity, compactness, and ease of beam extraction, the ICRA should provide a favorable and inexpensive alternative accelerator for these applications.

In a cyclotron, the accelerated particles are axially confined in a solenoidal magnetic field and accelerated azimuthally. The cyclotron and the cyclotron resonance accelerator differ primarily in the type of rf accelerating structure and the lack of axial focusing in the cyclotron resonance accelerator. In a cyclotron resonance accelerator, the beam simply drifts through the solenoid while being accelerated in the azimuthal direction.

Gyrotron oscillators are a source of coherent electromagnetic waves with frequencies ranging from one to several hundred GHz [4]. In a gyrotron, the energy of a dc electron beam is converted into microwaves in a resonant cavity within a solenoid magnet. The electrons spiral through the solenoid and are not axially confined as in a cyclotron. Even as the gyrotron was investigated as a source of microwaves, it was recognized that the inverse was equally feasible, i.e. it should be possible to accelerate electrons by driving a gyrotron structure with microwaves. Jory and Trivelpiece used cyclotron resonance acceleration in 1968 to produce a 10 mA, 460 kV electron beam [5]. This research will extend cyclotron resonance acceleration to ions by using a magnetron rf structure operating at a harmonic of the cyclotron frequency and a superconducting solenoid.

The essential components of an ICRA, shown schematically in Figure 1, include an ion source, superconducting solenoid magnet, resonant cavity, and an rf power source. The superconducting solenoid provides a high axial magnetic field which is nearly constant over the volume of the resonant cavity. In the fringe field of the solenoid, ions are extracted from the source by a dc bias voltage and spiral into the high field region such that most of their velocity is perpendicular to the magnetic field. While orbiting field lines at the cyclotron frequency (ω_c=qB/γm), the remaining small component of velocity parallel to the B-field causes an axial drift through the cavity. Thus the magnitude of this parallel velocity component determines the number of turns ions experience while traversing the cavity length. Within the cavity ions are accelerated in the azimuthal direction by electric fields that cross gaps in the cavity wall. Summing the energy gained at each gap over the total number of turns gives the final ion energy upon exit of the cavity. Since the resonant cavity is an open ended structure, ions exit the structure and spiral around magnetic field lines until impacting a target at some definite angle.

The accelerating rf electric field is provided by a resonant cavity known as a magnetron structure [6]. Electrically this cavity behaves like a resonant circuit made up of 2n coupled harmonic oscillators, each with inductance L and capacitance C that can be found from the cavity dimensions. Figure 2 shows the cross section of a magnetron structure with 4 oscillators. In the π mode of operation, the resonant frequency of the entire cavity is equal to the resonant frequency of a single oscillator ($\omega_o = 1/\sqrt{LC}$) and is independent of cavity length (into the page). An rf power source drives the cavity at its resonant frequency ($\omega_{rf}=\omega_o$) through a coupling antenna. The resonance condition required for acceleration

implies a harmonic relationship between the ion's cyclotron frequency and the rf frequency ($\omega_o=\omega_{rf}=n\omega_c$) where n=2 in this example. For the case shown here, it is the electric quadrupole field in the central region that provides the azimuthal acceleration across each gap. Since a multipole field goes to zero on axis (r = 0), an ion will gain maximum energy across a gap when orbiting closest to the wall. For this reason it is advantageous to taper the cavity such that the inner wall radius increases as the beam's orbit radius increases.

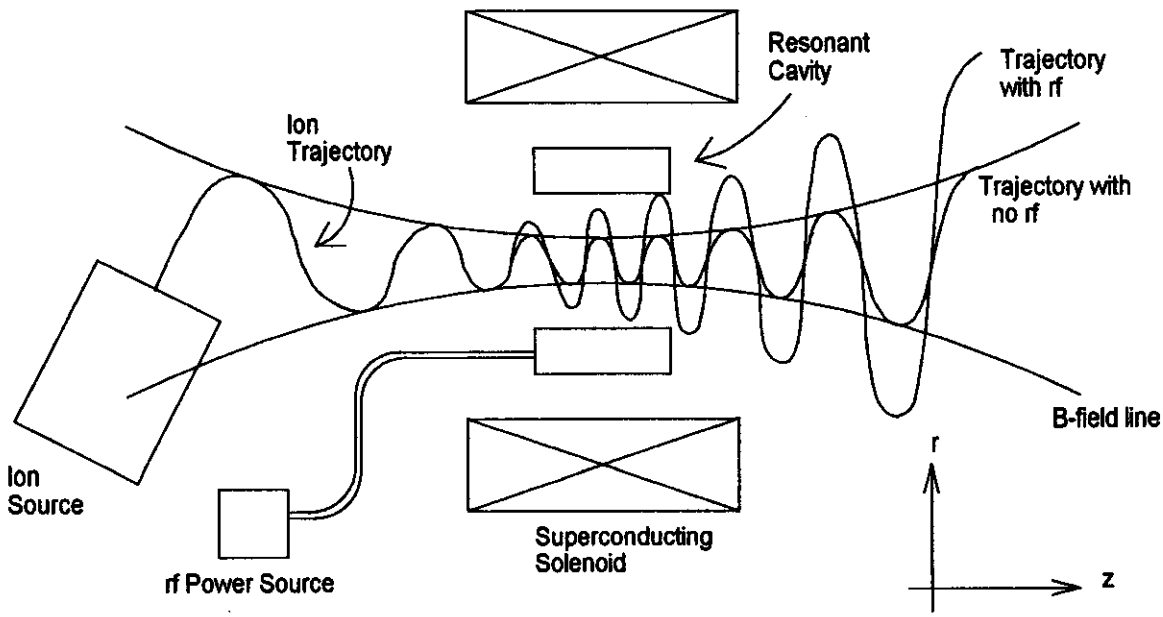

Figure 1: Components of an ion cyclotron resonance accelerator

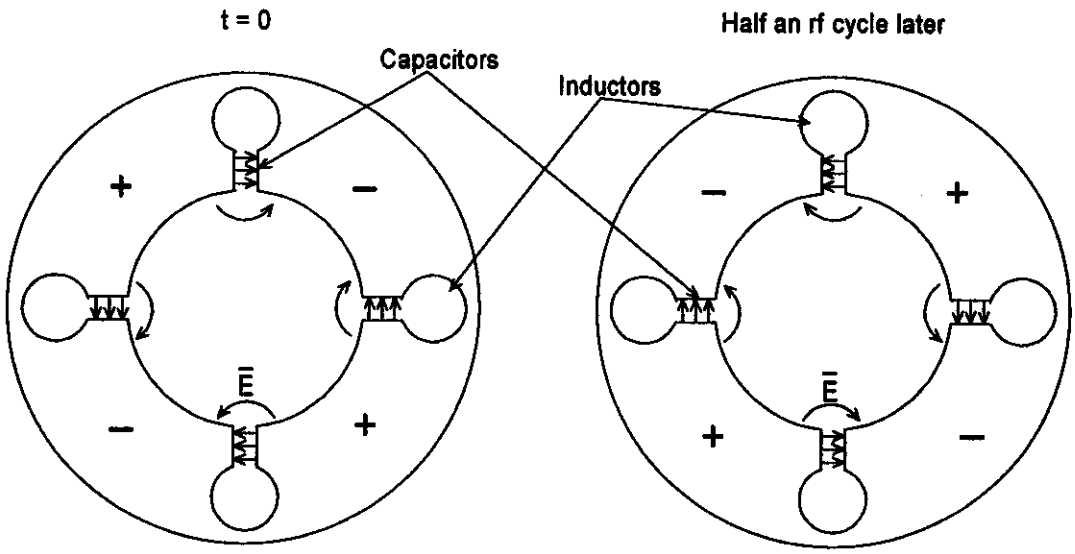

Figure 2: A cross section of a magnetron structure operating in the p mode is shown at two different rf phases. Z axis is into the page.

The specific case of an ICRA suitable for the production of 1 MeV protons is being evaluated since at this energy the hardware costs for experimental verification would be modest. Design parameters for this 1 MeV ICRA include an injected beam energy of 50 keV perpendicular and 1 keV parallel to the magnetic field. The resonant cavity is an 8 gap (4th harmonic) magnetron structure with a linear taper such that the inner cavity radius is R=0.55 cm at the entrance plane, and R=2.0 cm at the exit plane. The cavity length is 10 cm and the gap voltage is 5.6 kV. The magnetic field is 8 T over the acceleration region and the cavity will fit into a superconducting solenoid of 8" warm bore. The cyclotron frequency for a proton in this field is 122 MHz, therefore the rf frequency for this cavity is 488 Mhz.

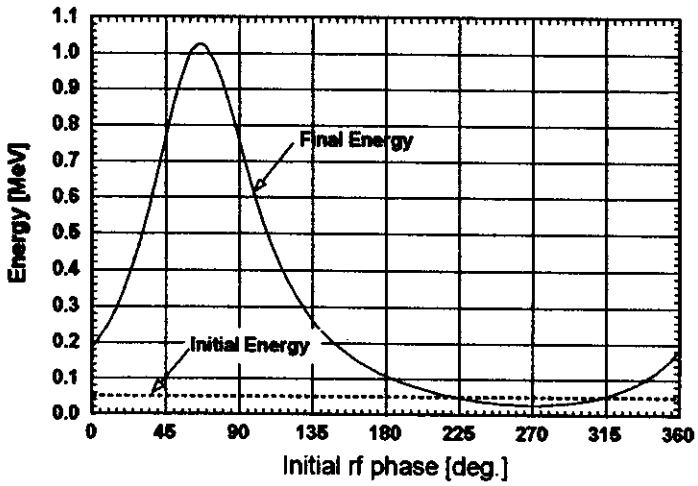

Figure 3: Final proton energy vs. initial rf phase for the 1 MeV design.

Computer codes RELAX3D, developed at TRIUMF, and a variation on Z3CYCLONE, developed here at the NSCL, have been used to solve for the voltages in the magnetron structure and then to track particle trajectories through the acceleration region. Figure 3 shows the final energy of protons that start at different initial phases relative to the rf. Since the rf here is a sine wave, one would expect the maximum energy gain if the proton started at 90°. However since the cavity is tapered, a small component of the electric field parallel to the z axis leads to a phase dependant change in the z momentum. This shifts the optimum initial rf phase to 65°. From this graph we can estimate that roughly 30° out of 360°, or about 8% of an unbunched dc beam will be accelerated to a final energy in the range of 0.90 to 1.03 MeV. However this is true only for an ideal trajectory. To simulate a beam of finite emittance, seperable coordinates were assumed and Z3CYCLONE was used to scan the injected beam phase space at the entrance plane. Based on this analysis it was found that for a dc beam of emittance 3p mm-mrad, 5% of the beam will be accelerated to the desired energy range. To avoid thermal issues and space charge effects, an output beam current of 1 mA has been chosen as a design goal.

A more complete computer model is being developed for the purpose of tracking particle trajectories through the injection, acceleration, and extraction regions. This code will be used to study the detailed beam dynamics of the 1 MeV proton ICRA. A future study will evaluate the design of a 6 MeV proton machine suitable for use as a neutron source or for the production of radioisotopes.

References

1. H.G. Jacobson (Editor), Council on Scientific Affairs, Cyclotrons and Radiopharmaceuticals in Positron Emission Tomography, JAMA, **254,** 12 (March 25, 1988) p.1854 - 1860
2. G.C. McClellan, Neutron Radiography Techniques and Applications, Nondestructive Testing and Evaluation for Manufacturing and Construction, H.L.M. dos Reis (Editor) (1990) p.319 - 328
3. K. Ziegler, Materials Research with Beams at Cyclotron Energies, Proc. of the 13th Intl. Conference on Cyclotrons and their Applications, (1992) p.149 - 157
4. Varian Microwave Power Tubes (catalog of products), Varian, Palo Alto, CA, (Sept.1989)
5. H.R. Jory and A.W. Trivelpiece, Charged Particle Motion in Large-Amplitude Electromagnetic Fields, J. of Applied Physics, **39,** 7 (June 1968) p.3053-3060
6. R.S.H. Boulding, The Resonant Cavity Magnetron, D. Van Nostrand Co. Inc., (1952)

STUDY OF 1000 MeV, 10 MILLIAMP, SUPERCONDUCTING CYCLOTRON TO PROVIDE SUPPLEMENTAL NEUTRONS FOR THORIUM CYCLE POWER REACTORS

H. Blosser and D. Johnson

I. Introduction

Recently, considerable interest has focused on using accelerators to provide supplemental neutrons for thorium fueled nuclear power reactors. Attractive features of such a system have been reviewed by Bowman[1] and include:

1) thorium is quite abundant (adequate to meet world electrical needs for several thousand years).
2) production of ^{239}Pu is largely eliminated so that risk of diversion of power reactor by-products into weapons is minimal.
3) with a moderate additional burden on the overall neutron economy, long-lived radioactive by-products can be internally consumed in the reactor.
4) the accelerator produced neutrons can be turned off very quickly (milliseconds) compared to movement of conventional control rods thus enhancing overall power plant safety and allowing consideration of fast neutron based reactor designs[2].

An extensive review of the details of this type of power system has been prepared by Bowman, et al[3]; Rubbia et al[4] have proposed a specific system based on an upgraded version of the meson factory cyclotron at the Paul Scherrer Institute (PSI)[5].

The upgraded PSI cyclotron suggested by the Rubbia group involves a three stage accelerator dominated by a stringent design assumption regarding extraction efficiency, namely that successive orbits be totally separated in the two cyclotrons so that extraction losses will be less than 0.01%. For the final stage cyclotron, this requirement implies an acceleration system with an energy gain of 8 MeV/turn, which becomes the dominant cost factor in the overall accelerator system. The PSI based accelerator concept also involves intricate space charge issues at the stage-to-stage transitions, and a massive magnet for the third stage cyclotron (final beam radius - 5.7 meters, overall diameter - 16 meters, weight - about 4000 tons).

An alternate design concept for such a 'reactor driver' cyclotron (RDC) is to use a single stage compact cyclotron operating at considerably higher magnetic field (a final beam radius of 2 meters has been selected for the preliminary study described here) and allowing beam losses of a few per cent at extraction so that energy gain can be reduced to about 0.4 MeV/turn with a resulting very large reduction in rf power. With these assumptions, which are basically those of the first PSI injector (the 'Phillips' injector), a broad interval of rf phase can be accepted from a conventional internal ion source and, assuming the beam can be carefully centered across the full phase interval, a rather complete partial separation of turns can be achieved at the edge of the cyclotron (as shown in a later section) based on the conventional isochronous cyclotron approach of using a small field bump at the $\nu_r=1$ resonance to induce a coherent radial precessional oscillation in the beam. In this fashion the Phillips injector achieved extraction efficiencies of 93%[6]; in a larger cyclotron such as considered here, and with a thinner septum, this efficiency can apparently be raised to the 98% range (as also discussed in a later section).

With losses of 2%, the total power in the non-extracted beam is still quite formidable, namely 200 kw (assuming the usual nominal specifications of 10 milliamps at 1000 MeV for the RDC primary beam). The compelling feasibility issue to address first in considering such a cyclotron design is developing an extraction system that will survive in the presence of such an intense beam. The work

which we report here is a first step toward this goal, and gives a preliminary indication of general feasibility of achieving a system with adequate power handling capability.

Assuming the preliminary indication of power-handling feasibility (i.e., that a workable multi-turn extraction system can be achieved including features appropriate for handling the power dissipation of the non-extracted beam) is confirmed by more detailed studies, the next phase of this design study will assess a further formidable problem, namely to develop an initial conceptual design of the remote handling devices needed to allow the cyclotron to be adequately maintained in the face of the high levels of radioactivity which will be induced in the cyclotron structure by the lost beam. The level of induced radioactivity from lost beam at the 2% level is clearly very high compared to that experienced in presently operating cyclotrons where losses are held to levels compatible with 'hands-on-maintenance' -- on the other hand the radioactivity is relatively minor compared to that of reactor components themselves or even to that experienced in primary production targets at accelerators (such as the 1000 kw beam power in the primary production target at PSI or at LAMPF). The design challange is then to design an accelerator structure compatible with the handling techniques developed for reactor components and accelerator production targets so that required maintenance can be performed without exposing personnel to unacceptable radiation levels. This next phase will include further development of the features of the main accelerator itself since this is needed in order to identify the location of beam loss points in a detailed way which is a prerequisite to development of devices for remote handling of the radioactive components.

Section 2 of this report describes the conceptual design of the accelerator as it exists at this time; Section 3 describes the orbit tracking studies which are the basis of the preliminary indication of feasible solutions to the power dissipation aspect of the multi-turn beam extraction concept.

II. Cyclotron Structure

Noting that the rigidity of protons at 1000 MeV is 5.6 Tesla-meters and selecting 2 meters as a first choice for the extraction radius means that the azimuthal average of the magnetic field at this radius must be 2.8 Tesla and that the field in the magnet hills will therefore need to be about 3.5 Tesla. Fields of this strength are most economically achieved using superconducting coils as in the present generation of compact superconducting cyclotrons. These cyclotrons are characterized by a circular main superconducting coil in a separate cryostat with a surrounding 'pill-box' iron yoke; access to the main acceleration chamber is obtained by raising/lowering the top/bottom of the yoke using a built in jacking system; accelerating electrodes, vacuum pumps, etc. are mounted from the respective yoke slabs. A cyclotron to produce 1000 MeV protons would involve a basic structure very similar to that developed by the EULIMA group for a proposed heavy ion therapy facility. Figure 1 is a cut away view of such a cyclotron from one of the EULIMA papers[7].

To study orbit characteristics in such a cyclotron, we need to first develop a reasonably realistic description of the magnetic field; given the ease of 2-D magnet calculations relative to 3-D we proceed in the now traditional way of using 2-D calculations of an azimuthally averaged steel array and thereafter replace the steel in the pole tip region by a detailed azimuthally varying computation based on the fully saturated approximation which can be quickly computed.

Proceeding in this way, we first lay out a profile of the azimuthally averaged magnet steel distribution, Figure 2, to be used for the 2-D relaxation calculation of the average magnetic field. As seen in the Figure, the assumed distribution includes the feature of reducing the thickness of the yoke steel near the cyclotron axis to assist in developing the required sharp radial increase in the average field in order to match the 110% radial increase of the isochronous magnetic field. (The relaxation studies show that an even greater thinning of the yoke than that shown in the Figure will be needed in a fully optimized design, but the structure shown is adequate for the present purpose.)

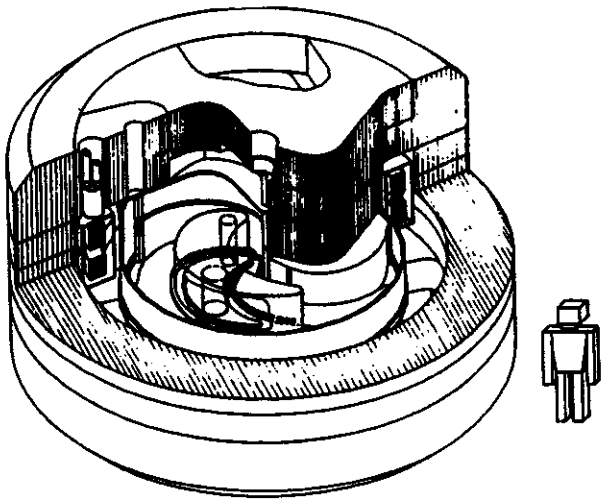

Fig. 1 : Cut away view of the superconducting cyclotron proposed by the EULIMA group [7] for heavy ion therapy. The superconducting cyclotron described in this paper is conceptually similar.

Figure 3 is a plan view of the pole tip structure used for the saturation calculations of the azimuthally varying field components and shows the unusal feature of six sectors at the outside combining in pairs into three near the center. (The six sector configuration at large radius is the minimum required to shift the N/2 stop-band out of the operating range of the cyclotron and three sectors near the center provide a good configuration for achieving well-centered orbits and also add to the axial focussing as needed to provide an axial space charge limit in the vicinity of 50 milliamps.)

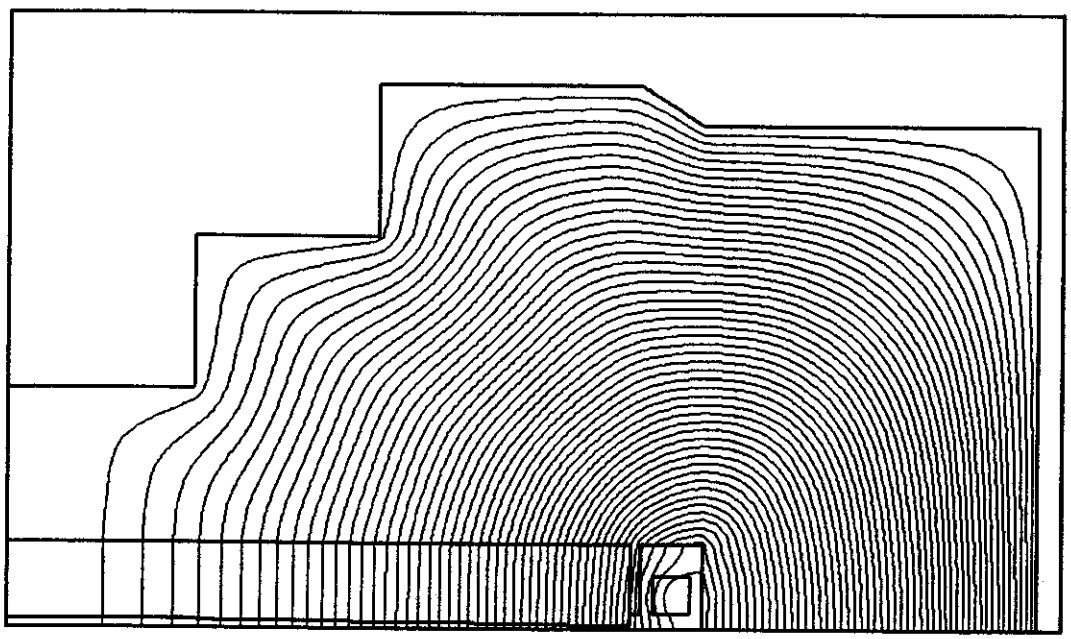

Fig. 2: R-Z drawing of the iron configuration used in the initial relaxation calculations. The outer edge of the yoke is at a radius of 332 centimeters, and the yoke height at this radius is ±161 centimeters. The iron fraction in the pole tip area is .4, the pole tip outer radius is at 201 centimeters, the minimum hill gap is ±1.25 centimeters, and the valley gap is ±27 centimeters. Steel far away from the medium plane near r=0 has been removed in coarse steps, and additional steel will be removed in smooth steps to achieve a well optimized design, but this is reserved for future studies. The total weight of steel for the geometry shown here is 457 tons. Coils are 12cm × 12cm excited at 2,800 amps/cm^2.

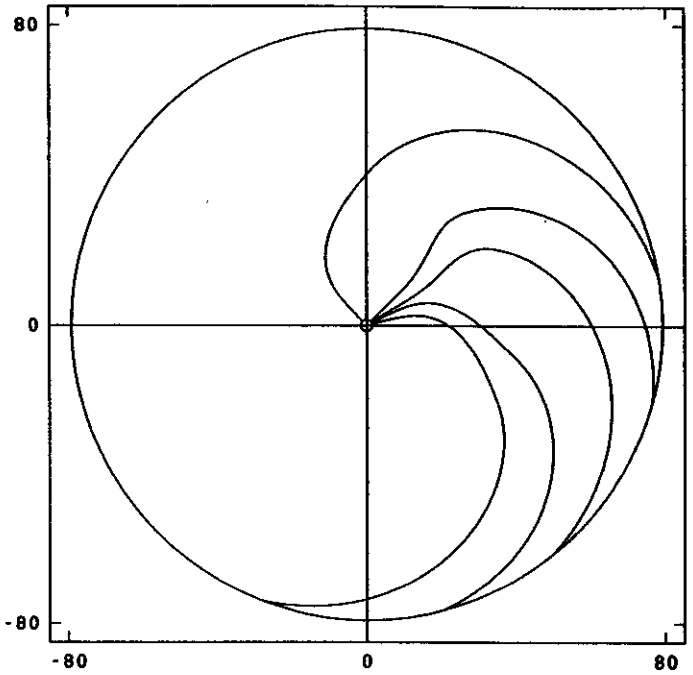

Fig. 3: Geometry of the pole tip for 120 degree sector showing the 6-sector structure at outer radius merging to a 3-sector structure in the center. Scales are in inches.

Figure 4 shows the computed flutter field in the form of Fourier amplitudes vs. radius for the pole tip structure given in Figure 2. Figure 5 is an isogauss contour map of the resulting total magnetic field. (In the internal beam region, an isochronizing correction has for the present been arbitrarily added to the B-average from the relaxation calculation.)

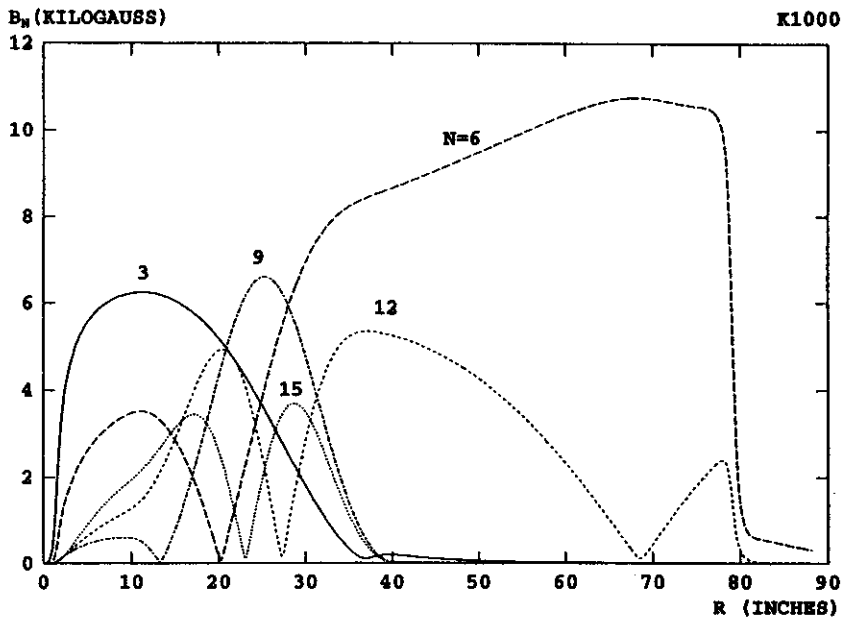

Fig. 4: Amplitudes of various magnetic field harmonics for the pole tip structure shown in Fig. 3; fields are computed using the saturated iron approximation. Zero crossings of particular harmonics, ie. 6 at r=20.5, 15 at r=23, etc. are due to the symmetry structure of the hills and valleys.

III. Extraction Studies

Assuming an axial beam height of 3mm, a useful phase width of 20 rf degrees, and an energy gain of 1.67 MeV/turn, the magnet structure from the previous section has a minimum ν_z of 0.4, and thus gives an axial space charge limit of 53 milliamps. (The longitudinal space charge effect which traditionally limits accelerated current in cyclotrons assumes single-turn extraction and so is not relevant in the multi-turn extraction regime.) If we use this magnet to accelerate a 10 milliamp beam and anticipate 98% as a likely limit on extraction efficiency in the multi-turn regime, the presumed extraction loss is at the 200 kw level, i.e. higher by a factor of 500 than the 400 watt loss anticipated in the upgraded K1200 cyclotron at NSCL[8], and this figure represents the frontier of present extraction system performance in compact, high field cyclotrons. (The upgraded K1200 is not yet in operation but a number of experimental tests of actual septums indicate a high probability of achieving reliable operation at design values, the extreme design case being a beam of 6×10^{12} ^{40}Ar ions at 180 MeV/A.)

The critical, power-limiting component of the extraction system is the deflector septum. Immediately at the septum entrance, the power density in the septum structure is given by the stopping power of the primary beam times the incident flux. Comparing the proposed RDC vs. the upgraded K1200: if turn geometry was the same in the two cyclotrons, the flux would be proportional to the particles/sec, i.e. higher by a factor of 10^4 for the RDC, but the stopping power for protons of 1 GeV is lower by a factor of 700 relative to that of 180 MeV/A ^{40}Ar, so for comparable geometry, the increase in power density at the septum entry would be $\times$ 15. In this computation we assume identical turn geometry -- the 2 meter radius of the RDC vs the 1 meter radius of the K1200, reduces the 15 to 7.5 -- a further reduction factor comes from the number of turns (900 in the K1200 upgrade vs 600 presently assumed here, and a more aggressive assumption is clearly feasible) which is reduced by 2/3, leaving a factor of 5. For the present we assume that this remaining factor will be handled in one of two ways, namely:

1. By taking advantage of the ability to accurately match the septum to the real trajectories as a consequence of the single beam, fixed energy feature of the RDC vs variable energy and particle in the K1200. (Septum tests for the K1200 upgrade assume extraction losses of 10%; if these can be reduced to 2%, as following sections imply, septum power density becomes equivalent in the two structures.)
2. As a final backup, by building 5 driver cyclotrons of 2 milliamps each (which would apparently still leave a substantial cost advantage relative to the PSI based plan and would have the further advantage that a redundant 6th cyclotron could be added at a relatively minor added cost).

Away from the immediate septum entrance the greatly extended range of the 1000 MeV proton beam (700 times that of 180 MeV/A ^{40}Ar) rapidly reduces the power density in the proton situation due to particles scattering out of the septum -- more detailed calculations will be required to quantitatively evaluate the power dissipation problem in this region, but the septum entry seems clearly the most difficult point.

The extraction technique which we are initially exploring is similar to that traditionally used in compact cyclotrons, namely to introduce an imperfection field component to develop a carefully controlled radial oscillation amplitude at the $\nu_r = 1$ or the $\nu_r = 2$ resonance. Illustrating the essential behaviour of such an extraction system, Figure 5 shows the coherent oscillation developed when a 20 gauss first harmonic field component acts on an initially centered central ray shown by the open circles (centered at 585 MeV) and tracked with a surrounding eigen-ellipse to the outer edge of the cyclotron. The orbits in Figure 5 start from a single phase and therefore show the behavior which would result for a low current, narrow phase beam.

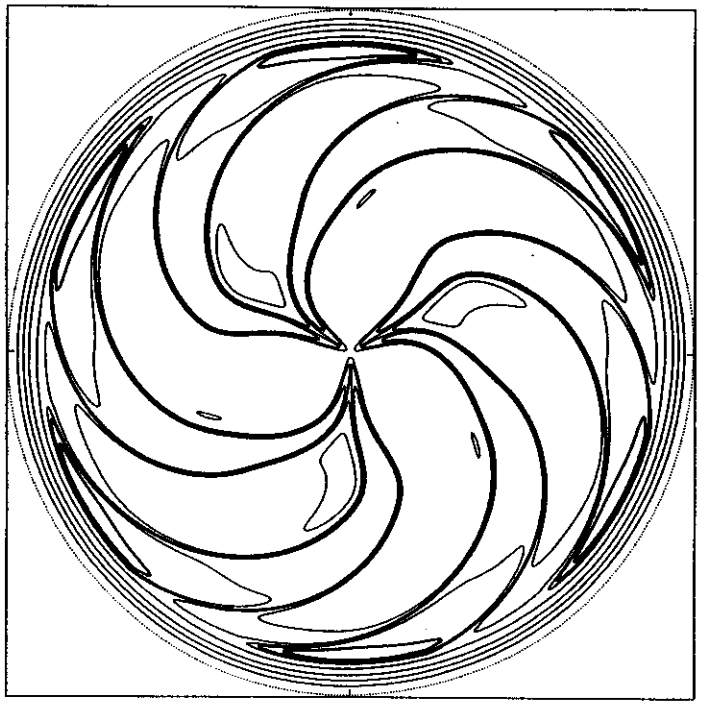

Fig. 5: Contour map of resulting isochronized magnetic field. The maximum contour is 3.5 tesla (denoted by the heavy solid line at the outer edges of the 6 hills). The minimum contour is 0 denoted by the dotted line surrounding the magnet. Other contours are at steps of .5 tesla.

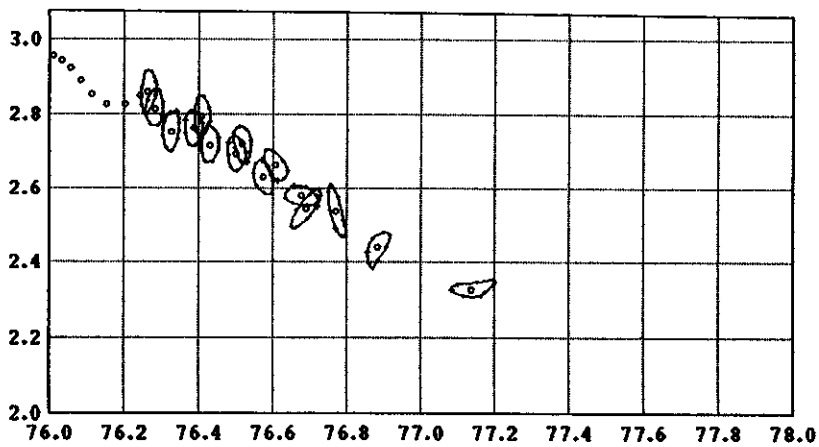

Fig. 6: Phase space plot of final turns of an initial, well-centered, eigen-ellipse (area corresponding to a circle of 0.88 mm radius) accelerated from 580 MeV with an energy gain of 1.67 MeV/turn. A 20 gauss first harmonic field bump is located at an azimuth of 90 degrees, and trajectories are plotted at the hill center azimuth. Horizontal axis is radius in inches, vertical axis is radial momentum $p_r/(m_0\omega_0)$ in inches.

The effect of the field bump and resonance on a broad phase beam is shown in Figure 6, which is a histogram showing number of particles per 0.0035 inch radius interval for a broad phase beam in which 12 additional initial phases have been added spaced at 2.5 degree steps from -15 to +15 relative to the group shown in the previous figure. Also, at every phase an additional 8 point eigenellipse has been added of half amplitude relative to the ellipse shown in Figure 5, so that the broad phase beam is in total represented by a family of 221 rays. At each phase the r,p_r coordinates of the central ray for that phase were adjusted so that the center point of the ellipse for every phase is just on center. All 221 particles

were then accelerated from 585 MeV to 'extraction' the latter being defined as having an r value at the azimuth of the plot exceeding 76.437 inches (marked by the vertical line in the figure). When this test is satisfied by a particular ray, the ray is considered extracted, plotted in one of the bins to the right of the marker line, and thereafter not tracked. (The results reported here are for median plane motion; future work will include axial displacements and other phase-dependent centering errors, the effects of which are expected to be small.)

Viewing Figure 6 we see a strong peak structure in the vicinity of 76.4 inches which would then be the optimum location for an extraction septum. Radial bins in the figure are .0035 inch, which corresponds approximately to a thinnest possible septum. If such a septum was perfectly aligned with one of the lowest bins (or if the septum was 1/2 bin in thickness, which is marginally conceivable, with the remaining 1/2 bin representing small misalignments), and if the phase space selected for the study precisely corresponded to the real beam, a septum entry efficiency of 97.7% results, i.e. about the same as the 98% assumed in the earlier discussion. The effect of the precessional oscillation is to reduce septum losses by a factor of approximately 7 relative to that which would result from a beam with no precessional oscillation, a very important contribution.

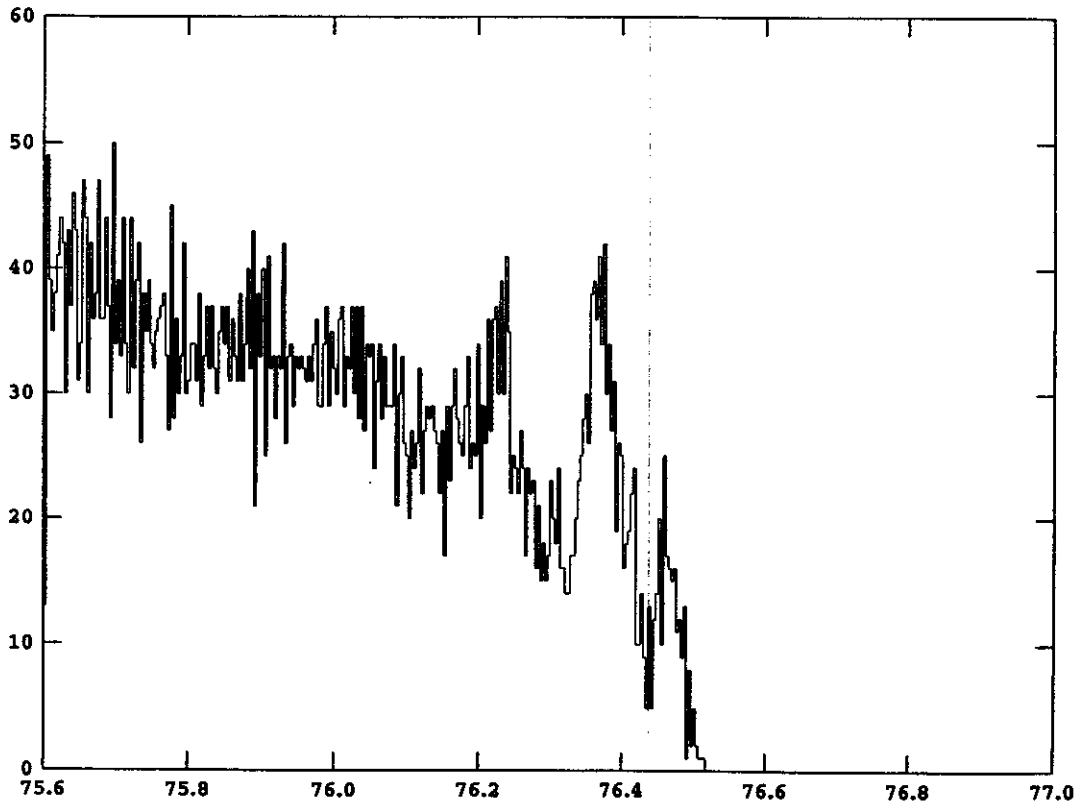

Fig. 7: Histogram of composite beam consisting of ellipses with +/- 2.5, +/- 5, +/- 7.5, +/- 10, +/- 12.5 and +/- 15 degrees relative to the group in Figure 6 and with a half amplitude ellipse included in each group to represent the effect of the better centered rays at each phase. Radial bins are .0035 inches. The histogram structure shows the effect of a first harmonic component in extracting a well centered broad phase beam. Each tracked ray is plotted and terminated on the turn where its radius first exceeds 76.437 inches (marked by the vertical line in the figure).

IV. Conclusions

The initial explorations described here show that a multi-turn, broad phase beam can be accelerated to 1000 GeV in a magnet of modest size and that septum losses can be reduced by a factor of about 7 by use of precessional extraction. With the beam size assumed, a septum of 90 micron

thickness gives a power density at the entrance the same as that expected in the MSU K1200 upgrade. As noted in the Introduction, the challenging problem of design of remote handling systems to deal with radioactive components will be taken up in future work.

The authors are indebted to Dr. Felix Marti for many helpful comments..

References

1. C. D. Bowman, AIP Conference Proceedings **346**(1994)22.
2. C. Rubbia, AIP Conference Proceedings **346**(1994)44.
3. Bowman, et al., Nuclear Inst. & Meth., **A320**(1992)336.
4. Rubbia, Mandrillon and Fietier, Proceedings of the European Particle Accelerator Conference (1995) 270.
5. Stammbach, Adam, Fietz, Joho and Schryber, AIP Conference Proceedings **346**(1994)229.
6. Stammbach and Jaccard, Proceedings of the 10th International Conference on Cyclotrons and Their Applications (1984)689
7. Mandrillon, et al., Proceedings of the 13th International Conference on Cyclotrons and Their Applications (1992)248.
8. The K500⊗K1200 Coupled Cyclotron Facility at the National Superconducting Cyclotron Laboratory, July 1994, MSUCL-939.

CONCEPT FOR AN INTERNAL ^{14}C DETECTOR FOR AN AMS CYCLOTRON

Jeff Schubert

Introduction

In an attempt to simplify the task of building a cyclotron based AMS system we consider building an internal ^{14}C detector to eliminate the need for an extraction system. The detector must count very low currents (.01–1/sec) of ^{14}C ions with an energy of only 40–50 keV/ion, while filtering out a background of scattered ions with energies of a few keV and also photons (UV and soft x-rays produced in the cyclotron.)

Theory of Operation

The detector itself would be similar to the external detector designed by Friedman for the "cyclotrino" at Berkeley.[1] A schematic of the Berkeley detector is shown in figure 1. The 40-keV ions strike an Al_2O_3 conversion dynode and liberate a few tens of secondary electrons, which are accelerated through a drift-gap by an electric field and allowed to separate from one another until they each land on separate pores of a microchannel plate (MCP) which multiplies each secondary electron by about 10^7. The total charge is collected on an anode. The hight of the output pulse is proportional to the number of secondary electrons ejected from the dynode which is proportional to the energy of the incident ion. A 40-keV ^{14}C ion should eject 15–30 secondary electrons, resulting in a pulse which is the sum of the output for 15–30 MCP channels. Photons or stray low energy particles striking the dynode should result in a pulse small enough to be discriminated from the 40 keV pulse. A photon or stray particle striking the MCP directly should only fire one channel.

The MCP is operated in saturation mode so that each channel produces the same output. Each secondary electron should land in a different channel in order to be counted. Because a typical stack has three plates, oriented randomly, a single channel in the first plate will trigger three channels in the second plate which will trigger a cluster of roughly seven channels in the final plate. Therefore, for proportional counting, the secondary electrons should land at least three channels away from one another on the first plate.

Putting the Detector Inside the Cyclotron

For the internal detector the dynode would intercept the beam at the median plane of the cyclotron, and the secondary electrons would then follow the B-field lines down to the MCP plate a few cm below the midplane. Looking into the cyclotron from the side the detector would look something like figure 2.

The magnetic flux density falls as the electrons move away from the midplane so the ratio of the dynode size to the MCP size would be the ratio of the flux density at the MCP to the flux density at the midplane. The change in B-field will spread the beam in the azimuthal direction more than in the radial direction, so to use the circular MCP area effectively the dynode may need to have an elliptical shape. Rectangular microchannel plates are also available and might be considered.

The degree to which the electrons separate from one another would then be a function of their

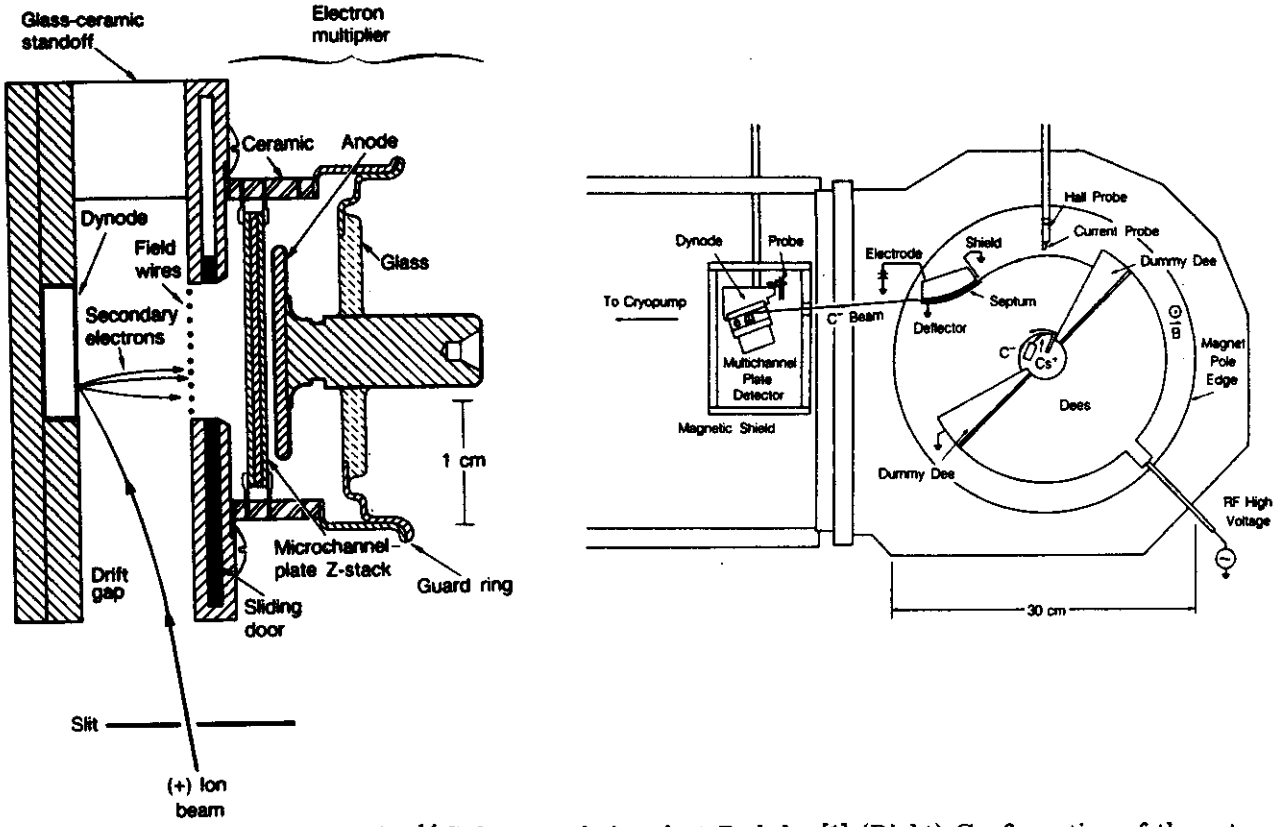

Figure 1: (Left) Schematic of the ^{14}C detector designed at Berkeley.[1] (Right) Configuration of the external detector with respect to the cyclotron.[2] The choice of flat poletips with a 3.2 cm gap and a 1.0 T magnetic field precluded any studies toward an internal detector.

Larmor radius, so the average distance between electrons would be proportional to their initial momentum transverse to the B field, and to the magnitude of the B-field at the MCP detector.

The plane of the MCP would probably be perpendicular to the B-field, while the dynode would need to be tilted out of the median plane, resulting in some asymmetry in the electric field of the accelerating gap. We assume that this asymmetry would not be a problem since it is the number rather than the momentum of the secondary electrons that we are interested in.

Even without good turn separation, most of the beam would strike the dynode. The only losses would be from beam landing on the top or sides of the dynode or hitting the fixture that holds the dynode in place. Since the detector is insensitive to small changes in beam energy, it shouldn't matter if the last two or three turns are measured simultaneously.

Two issues that arise are 1) can we reduce the magnetic field at the MCP stack to a low enough value so that the secondary electrons spread out enough so that each lands in a different channel, and 2) will the electric field used to accelerate the secondary electrons interfere with the last few turns of the beam before it hits the dynode?

Minimizing the Magnetic Field at the MCP Stack

The poletips of the available magnet have a 35 cm radius with a maximum hill field of 1.3 Tesla. To run 40 keV $^{14}C^-$ ions at a 30 cm radius we could turn the average field down to 3.4 kG, so the hill field would be 4.8 kG and the valley field would be 1.5 kG at the midplane.

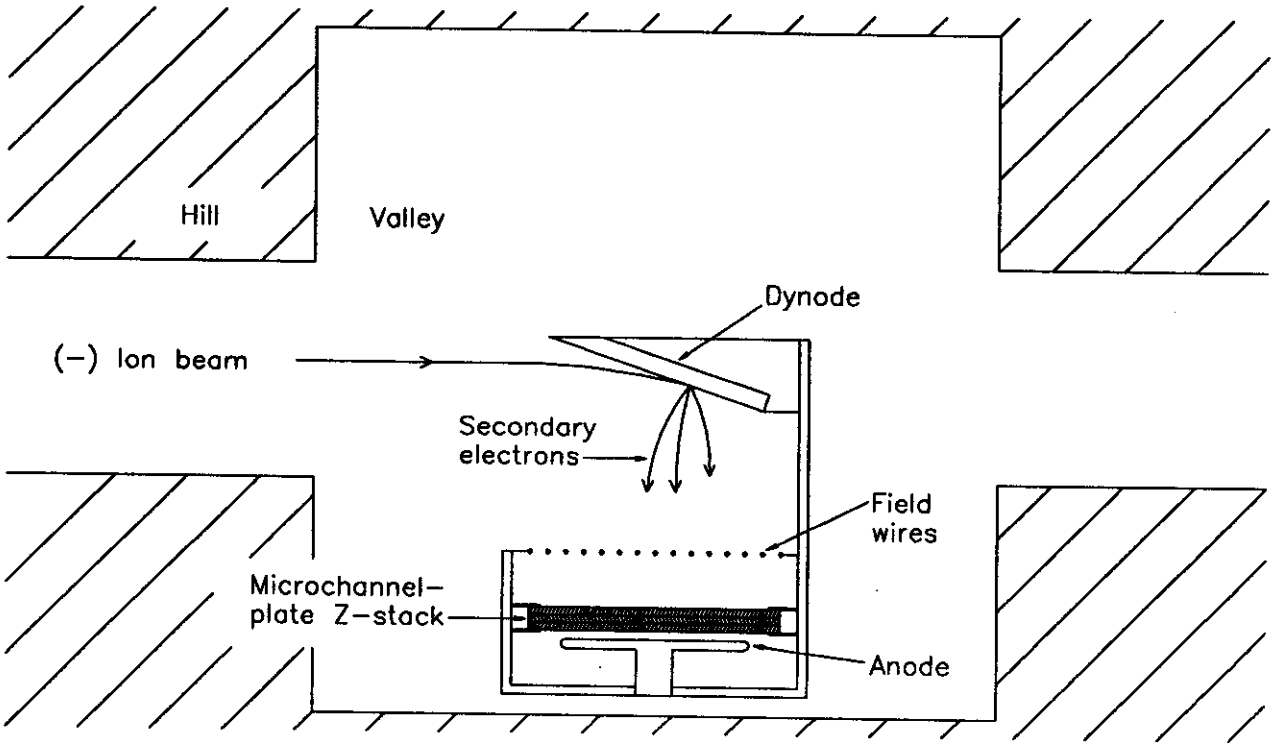

Figure 2: The internal ^{14}C detector. The view is looking into the cyclotron from the side.

To calculate the spacing between secondary electrons, we start by assuming $N = 30$ electrons (as in reference 1) with an initial energy of 10 eV which is mostly due to electrostatic repulsion from one another. We assume that all of the 10 eV is associated with momentum away from the rest of the electrons. The Larmor radius, r_L, of 10 eV electrons in a 1.5 kG field is 53 μm. The electrons will be confined to a circular area with a radius $R = 2r_L$. If we assume an even distribution of electrons over the allowed area, then we calculate the average distance $d = 2(R^2/N)^{.5} = 39\,\mu m$. This is equivalent to 2.6 pore spacings with pores 15 μm apart, which is roughly the theoretical limit of electron density before some electrons fail to be multiplied proportionally. (The distribution of electrons actually has a peak at the center of the allowed area and a minimum at an intermediate radius, but the area of high density is a small fraction of the total area, so only a few of the 30 electrons might be lost due to this effect.)

The field in the valleys could be reduced by milling the valleys deeper than in the present configuration, or the field near the MCP could be lowered by drilling a hole in the valley floor and locating the MCP inside this "sub-valley" where the lines of flux would diverge toward the walls of the hole. The B-field due to the magnet coils alone is approximately 300 gauss, which would allow an average separation of 20 pore spaces between secondary electrons, the same as in Friedman's calculation. With the unavoidable fringe field from the hills, the minimum possible valley field should be somewhere between 300 G and 1.5 kG.

We could also use a non-uniform electric field in the drift gap to assist with the spreading of the secondary electrons.[3] If we imagine a cylindrical coordinate system with the z-axis centered on the MCP, then we want the radial gradient of the radial component of the electric field $\frac{\partial E_r}{\partial r}$ to be positive at all r. The desired field shape will be accomplished automatically by making the dynode smaller than the area of

the field wires. If we wish to enhance $\frac{\partial E_r}{\partial r}$ we might use more than one set of field wires to control the field shape in some region. It doesn't matter at what z coordinate the separation takes place. The electrons might drift as a compact bunch from the dynode to the first set of field wires, and then the bunch could be separated between the first and second set of field wires, prior to landing on the MCP.

Minimizing the Fringe Electric Field

The last few turns of the ion beam will sample the fringe field from the drift gap, which will result in a force in the -z direction. If we assume a 2 cm diameter dynode, 30 cm from the center of the cyclotron, then the orbiting particles will spend roughly 1/100 of their orbit in the undesired electric field. The cyclotrino's detector used a 1 kV/cm field in the drift gap. If a $^{14}C^-$ ion experienced the entire magnitude of the electric field it would receive a change in momentum of 5×10^{-22} kg·m/s ($P_z/qB = .84$ cm $= .33$ inch), which corresponds to an axial velocity of 5 cm/orbit. This is probably far to much for a weak focusing cyclotron, however, few particles should experience the full intensity of the electric field if they are not on a collision path with the dynode.

There are also several options to reduce the fringe field. First, the field wires should be placed as close as possible to the dynode. The field strength of 1 kV/cm was chosen by LBL only to insure enough electron spreading for the zero-B-field environment. Since our inter-electron distance is dominated by the B-field, the only determining factor for the E-field is that the electrons must strike the MCP with enough energy to fire a pore and be multiplied. The MCP used by LBL claimed a collection efficiency (fraction of incident electrons which fire pores) of between 60% and 100% for electrons with greater than 200 eV. MCPs are available with collection efficiencies of 90% for electron energies as low as 100 eV, so a 1cm drift gap with an E field as low as 100–200 V/cm should be permissible.

To deal with the remaining effects of the fringe field we could place a "dummy detector" after the real detector which would have the same geometry but opposite voltages, so after the particles received a downward (and radially inward) kick they would receive an equal and opposite kick.

Conclusion

The internal ^{14}C detector appears to be a reasonable design option for an AMS cyclotron. Both of the issues discussed above lend themselves to computer modeling, and the effect of the detector's electric field could probably be incorporated into the orbit program CYCLONE. Detailed calculations would follow the design of the cyclotron poletips, which would tell us how much space is available for the detector and and how low the field can be in the valleys.

References

1. P.G.Friedman *et. al.*, Low background-rate detector for 40-keV ions using a conversion dynode and a microchannel-plate electron multiplier to reject low-energy ions, electrons and photons. RSI 59,98(1988).
2. J.J. Welch *et. al.*, A low energy cyclotron for radiocarbon dating, NIM B18,202(1987).
3. J.Yurkon, private communication, 1995

FEASIBILITY OF A MINI-CYCLOTRON FOR ACCELERATOR MASS SPECTROMETRY AT THE NSCL

Jeff Schubert

Introduction

Accelerator Mass Spectrometry (AMS), used as a method of determining the abundance of radioisotopes, is 1000 times more sensitive than traditional decay counting.[1] Since the discovery of AMS in 1977 many accelerators have been converted into ^{14}C dating devices for archeology. With AMS accurate dates may be obtained with as little as a milligram of carbon. The reduced sample size is of great value to archaeologists as well as art historians who must destroy part of an artefact in order to extract enough carbon to date it. More recently AMS has been investigated as a tool for detecting radioisotopes that are used as tracers in biomedical experiments. As in archeology, the 1000 fold increase in sensitivity has driven rapid development of this new industry. The Center for Accelerator Mass Spectrometry (CAMS) at Lawrence Livermore runs over 10,000 samples a year using 8 different isotopes. 80% of the AMS work at LLNL involves measuring ^{14}C at abundances of 10^{-12}–10^{-15} relative to ^{12}C.[2]

CAMS and most other commercial AMS laboratories use electrostatic tandem accelerators with energies of at least 1 MeV. The large size and cost of tandem accelerator systems has motivated a few groups to study the possibility of a cyclotron-based AMS system. Because the cyclotron automatically selects one charge to mass ratio (Q/A) to accelerate, the acceleration and mass-separation are performed in one step. Cyclotrons are also capable of isolating ^{14}C in beams with energies as low as 25–50 keV/ion.

Principle of Operation

The resonance condition for an isochronous cyclotron tells us that for a given magnetic field, B, and particle frequency, $f_p = \frac{1}{2\pi}\frac{qB}{m_o}$, only ions of one charge to mass ratio, q/m_o, may accelerate with out changing in phase, ϕ. Non-resonant background particles (e.g. species with the same charge but a different mass, m) will experience phase-slip proportional to their mass difference, $\Delta m \equiv m_o - m$. Once a particle slips more than 90° out of phase it is decelerated back toward the center of the machine. The AMS cyclotron, then, relies on a large number of turns to allow the phase-slip of background particles to accumulate and/or a high harmonic ($h = \frac{f_{RF}}{f_p}$, where f_{RF} is the RF frequency) to maximize the phase-slip/turn.

The resolution of the cyclotron mass spectrometer is defined as the inverse of the mass difference required to shift a background particle from $\sin\phi = 1$ to $\sin\phi = -1$, which would insure that background particles of any possible starting phase will cease to accelerate. An approximate expression for the resolution is derived in reference 3.

$$R \equiv m/\Delta m = \pi h N_o$$

where h is the harmonic number, and N_o is the number of turns an in-phase particle would experience.

To separate $^{14}C^-$ from the nearest molecular isobar, $^{12}CH_2^-$, a resolution of 1800 is required. (Negative ions are used because ^{14}N does not form a negative stable ion.) A cyclotron operating in 3rd harmonic mode would require approximately 200 turns. Conversely, a smaller 50 turn cyclotron could achieve the same resolution if it could be operated at 12th harmonic. The final energy of the beam is only relevant to the problem of detection, and a large energy gain per turn, ΔE_t is only desirable to facilitate

injection and extraction of the beam. Otherwise a low value of ΔE_t, and hence, a low dee voltage would be desired in order to maximize the turn number.

Existing AMS Cyclotrons

Three cyclotrons have been built solely for the purpose of mass spectrometry. During the 1980s Lawrence Berkeley Laboratory (LBL) built the "cyclotrino" with 10 cm radius flat poletips that relied on the fringe electric field in the dee gaps to provide vertical focusing. The cyclotrino detected ^{14}C at natural levels but was plagued by a very small phase acceptance. A successor to the cyclotrino with an improved injection system is nearly completed and awaits testing at LBL. At the Shanghai Institute of Nuclear Research, Chen et al. have extracted ^{14}C from 48 cm radius sector focused compact cyclotron. A schematic of the Shanghai mini-cyclotron for AMS (SMCAMS) is shown in figure 1. The SMCAMS uses an unconventional dee structure to provide greater energy gain on the first and last turns (to minimize injection and extraction losses) and a lesser energy gain in between to allow a large number of turns.

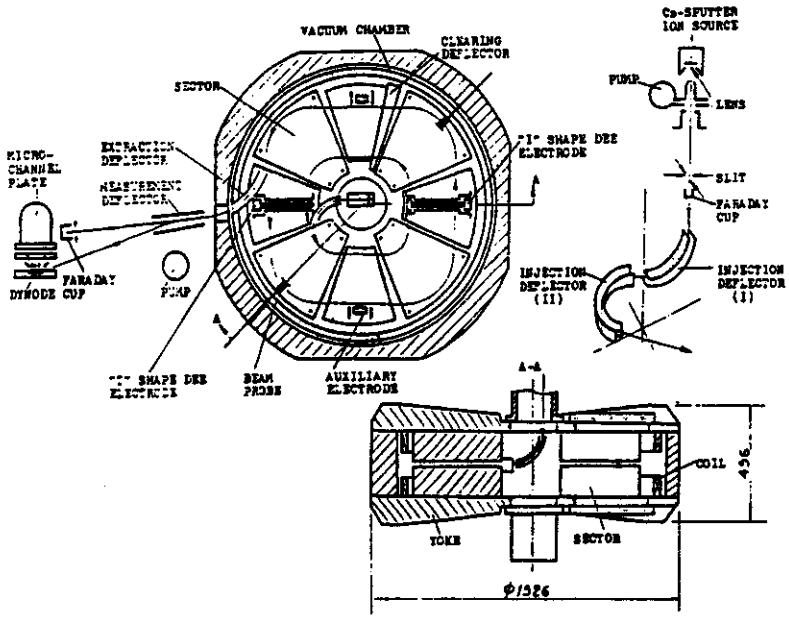

Figure 1: The Shanghai Mini Cyclotron for AMS.[4] Dimensions on the yoke are in mm. The injection and extraction radii are 20 cm and 48 cm respectively. The ^{14}C detector is shown on the far left. ^{12}C current is measured in the faraday cup next to the ^{14}C detector in order to normalize the count rate.

All of these cyclotrons accelerate ^{14}C to a final energy of 50 keV/ion with dee voltages ranging from 300 to 500 V. Individual ^{14}C ions are counted using a detector developed for cyclotron AMS at Berkeley. [5] The low operating voltage raises the possibility of using non-sinusoidal RF waves, such as a flat-topped sine or even a square wave, to increase the phase acceptance of the cyclotron. Chen *et al.* claim to have increased their total particle acceptance by a factor of 30 by using a novel triangular waveform with off-peak acceleration.[6] The SMCAMS has achieved a resolution of 3000 with an extracted ^{12}C beam of 500 nA, which corresponds to 5 cps of ^{14}C in a sample of modern carbon.

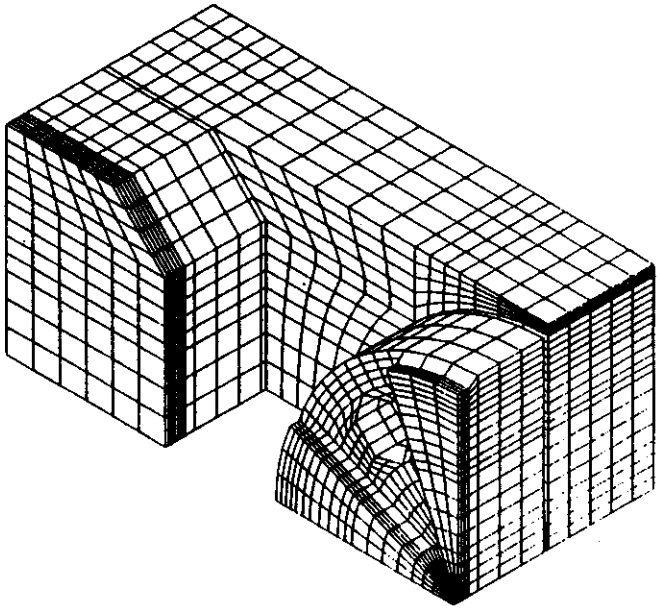

Figure 2: Mesh used for the calculation of midplane magnetic field of the airport cyclotron.[7] One eighth of the magnet is represented, with the machine's central axis at the lower right.

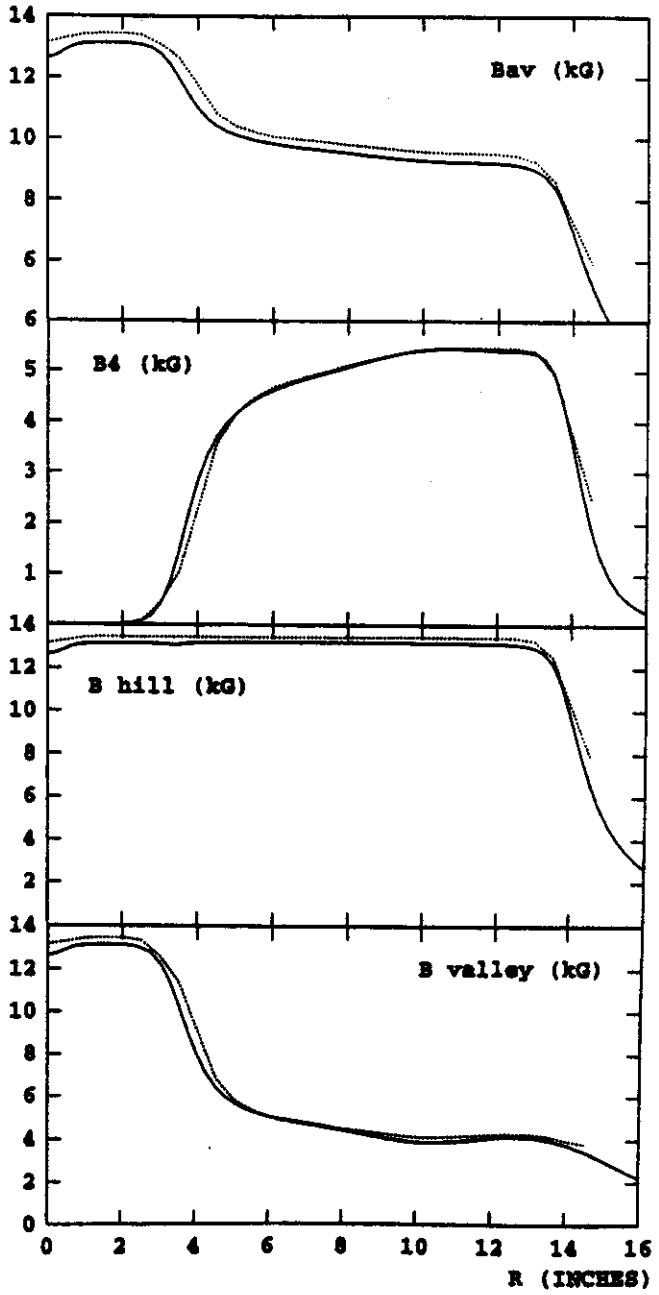

Figure 3: Main field parameters in the median plane of the airport cyclotron magnet for both the calculation (dashed line) and measurements(solid line). [7] Since the magnet iron is unsaturated, the field shape should be preserved when the overall field level reduced to match the requirements of the AMS cyclotron.

Scaling a Proven Design to Work in the Available Magnet

Studies for a possible cyclotron AMS system at the NSCL began with the mothballed steering dipole, M3, which currently resides on the roof of the experimental vaults. In the early nineties a development program sought to convert M3 into a four sector cyclotron for contraband detection (the "airport cyclotron.") Poletips were procured and the midplane field was modeled and mapped.[7] An eighth section of the yoke and poletip is shown in figure 2. Several properties of the midplane field are plotted in figure 3.

M3 offers a maximum extraction radius at 12.6 in, which is 2/3 as great as the SMCAMS's extraction radius. The average field available in M3, however, is over four times greater than that of SMCAMS. We could scale Chen's design into our magnet by holding the rigidity, $B\rho$ constant. An average field of 3.53 kG would be required, which is only 40% of that available in M3. (This quick calculation

does not account for the differences in scalloping between our magnet and Shanghai's, however it does demonstrate that a similar cyclotron could be designed to use the available magnet with the existing poletips.)

The Cs-sputter ion sources used for tandem and cyclotron AMS provide a 20 keV beam of $^{14}C^-$. At this energy the beam could be injected at a radius of roughly 5 in. We can see from figure 3 that by this radius the flutter field has turned on and there is no need for the magnetic focusing cone, or a complex central region for electric focusing. The center plug could then be removed to make room for a bulky injection channel which would also center the beam. Vertical focusing would be a simple function the flutter field, B_4, which is plotted in figure 3. Using the analytical treatment of Livingood[8] we can approximate the axial betatron frequency, $\nu_z \approx 0.37$ for the entire acceleration region. If we chose to mill the valleys deep enough to achieve the same flutter as SMCAMS we could raise ν_z to roughly 0.51.

It would not be necessary at first to use the advanced dee structures under development in China. An experimental machine could work with two wedge-shaped dees in opposite valleys and traditional on-peak acceleration. A peak dee voltage of approximately 75 V would accelerate a 20 keV beam to 50 keV in roughly 100 turns. The separation between the first and second turns would then be on the order of 1–2 mm, which should be adequate for at least part of the beam to clear an electrostatic injection channel. At this low voltage it might be economically feasible to use nonresonant dees. If we assume that a solid-state broadband transmitter excites the dees in parallel with a 50 Ω impedance, the total RF power $P_{RF} = \frac{1}{2}\frac{V^2}{R}$ would be only 56 W.

Both SMCAMS and the Berkeley cyclotrons use a short electrostatic channel to extract the 50 keV beam. Since our extraction radius and local field will be in between those of the Shanghai and Berkeley cyclotrons, the design should be a trivial scaling exercise. One possible improvement on the existing designs would be to move the ^{14}C detector inside the cyclotron. This would eliminate the complexities and beam losses associated with an extraction channel. Details of an internal detector are discussed in another paper.[9]

Conclusion

The NSCL possesses the resources and experience needed to begin a development program for cyclotron based accelerator mass spectrometry, and a suitable magnet is available for the cyclotron. The first milestone of such a project would be the commissioning of a cyclotron capable of delivering a beam of pure ^{14}C from a source fed with natural carbon. A crude cost analysis has determined that such a cyclotron could be built at a cost of approximately $ 250 K, with roughly one third of the cost for procurement and the remainder for human effort. This project may be investigated further when the funding environment is more conducive to new projects.

References

1. A.E. Litherland, Ultrasensitive mass spectrometry with accelerators, Ann. Rev. Nucl. Part. Sci. 30, 437(1980).
2. J.C. Davis, AMS beyond 2000, NIM B92, 1(1994).
3. D.J. Clark, Cyclotrons as mass spectrometers, 10th Intl. Conf. on Cyclotrons and their Applications, 534, East Lansing (1984).
4. M.B. Chen *et al.*, The successful SINR mini cyclotron AMS for ^{14}C dating, NIM B92, 213(1994).
5. P.G. Friedman *et al.*, Low background-rate detector for 40-keV ions using a conversion dynode and a microchannel-plate electron multiplier to reject low-energy ions, electrons and photons. RSI 59,98(1988).

6. M.B. Chen *et al.*, Adopting a non-sinusoidal wave dee voltage in minicyclotrons as mass spectrometers for dating, NIM A278, 409(1989).
7. D. Johnson, T. Kuo and F. Marti, Calculation of 3D Magnetic Fields with ANSYS, a Finite Element Commercial Code, Proceedings of the European Particle Accelerator Conference, Berlin 1992.
8. J.J. Livingood, Cyclic Particle Accelerators, Princeton: Van Nostrand. 1961.
9. J. Schubert, Concept for an internal ^{14}C detector for an AMS cyclotron, this Annual Report.

REMAINDER DIFFERENTIAL ALGEBRAS FOR THE STUDY OF LONG TERM STABILITY

Kyoko Fuchi and Martin Berz

The long-term stability of weakly nonlinear systems is an important problem that originated with the detailed study of the solar system, that has triggered the development of sophisticated perturbative methods for repetitive motion, and is now experiencing a new application in the field of particle accelerators.

In this case, the motion of particles can be described very well by high order Taylor transfer maps of the action on phase space. High order automatic differentiation and differential algebraic techniques [1,2,4,7] have offered a very elegant and accurate way to obtain such transfer maps. Since typically derivatives of up to order ten in six variables are needed, other methods are far from providing such a robust way to study the weakly nonlinear behavior of beams; hence the differential algebraic technique has evolved into one of the essential tools in beam physics.

However, the question of long-term stability remains as one of most difficult yet important problems. Recent ideas of Nekhoroshev and others triggered an analysis of stability in particle accelerator in normal form space, and the problem can be re-cast into a highly complicated optimization problem [10,9]. Along this scenario, the Taylor maps can be used to obtain families of six dimensional approximate invariants of motion, and the quality of them directly relate to the time for particles to be lost.

Because of the irregularity of the deviations from invariance, a conventional optimization of the six dimensional deviation function is very troublesome and never completely accurate. On the other hand, interval methods allow an exact estimate, but for complicated functions they suffer from a severe blow-up problem, the control of which is the key issue in getting a practical and very tight estimate. We have worked on the problem using various interval optimization methods, however all methods available to us failed to give satisfactory answers.

A new technique, the method of Remainder Differential Algebras, [11] employs high-order computational differentiation [3] to express the model function by a Taylor polynomial, and interval computation to evaluate the Taylor remainder error bound. In normal form theory, it is known that if the transfer map has a converging Taylor series in normal form coordinates, the system is stable. So the sharpness of the remainder term of deviation function is the key to the problem. The method is straightforward and can yield tighter bounds than the mere interval bounding of the Taylor remainder's $(n+1)$st order derivative obtained via forward differentiation. The method may shed light on the stability problem and many other questions requiring verified computations of complicated problems [9].

A short review of the theory is as follows. With the help of Taylor's theorem, any $(n+1)$ times partially differentiable function $f : [\vec{a}, \vec{b}] \subset R^v \rightarrow R$ can be expressed by the Taylor polynomial $P_{n,f}$ of nth order and a remainder $\varepsilon_{n,f}$, namely $f(\vec{x}) = P_{n,f}(\vec{x} - \vec{x}_0) + \varepsilon_{n,f}(\vec{x} - \vec{x}_0)$. Let the interval $I_{n,f}$ be such that for any $\vec{x} \in [\vec{a}, \vec{b}]$, $\varepsilon_{n,f}(\vec{x} - \vec{x}_0) \in I_{n,f}$. Then

$$\forall \vec{x} \in [\vec{a}, \vec{b}], \quad f(\vec{x}) \in P_{n,f}(\vec{x} - \vec{x}_0) + I_{n,f}. \tag{1}$$

Because of the special form of the Taylor remainder term $\varepsilon_{n,f}$, in practice usually the remainder decreases as $|\vec{x} - \vec{x}_0|^{n+1}$. Hence, if $|\vec{x} - \vec{x}_0|$ is chosen to be small, the interval remainder bound $I_{n,f}$ can become very small. We say a pair $(P_{n,f}, I_{n,f})$ is a Taylor model of f if and only if (1) is satisfied, and we denote it by

$$T_{n,f} = (P_{n,f}, I_{n,f}).$$

The question now is how to efficiently determine Taylor models for any arbitrary functional dependency that can be expressed on a computer. The key is to begin with the Taylor model for the identity function, which is trivial, and then successively build up Taylor models for the total function from its pieces. This requires methods to determine Taylor models for sums and products from those of the summands or factors, as well as from intrinsics applied to functions with known Taylor model.

Addition and multiplication of Taylor models are computed as follows [11]. Let the functions $f, g : [\vec{a}, \vec{b}] \subset R^v \to R$ have Taylor models $T_{n,f} = (P_{n,f}, I_{n,f})$ and $T_{n,g} = (P_{n,g}, I_{n,g})$. Then Taylor models for $f + g$ and for $f \cdot g$ are obtained as

$$T_{n,f+g} = (P_{n,f} + P_{n,g}, I_{n,f} + I_{n,g})$$

$$T_{n,f\cdot g} = (P_{n,f\cdot g}, B(P_{n,f} \cdot P_{n,g} - P_{n,f\cdot g}) + B(P_{n,f}) \cdot I_{n,g} + B(P_{n,g}) \cdot I_{n,f} + I_{n,f} \cdot I_{n,g}),$$

where $B(P)$ denotes a bound of the polynomial P. The key idea of computing Taylor models for intrinsic functions is to employ Taylor's theorem of the function under consideration. However, in order to keep a small remainder interval and not to contribute anything to the Taylor polynomial, some additional manipulations are necessary [11]. Altogether, it is possible to calculate Taylor models for all functions representable on a computer. For many practical problems, in particular the efficient solution of differential equations, it is actually important to complement the set of currently available operations by a derivation ∂ that allows the computation of a Taylor model of the derivative of a function from that of the original function. It completes the algebra of Taylor models into a Remainder Differential Algebra.

Table 1: The width of the bound interval of $f(x) = 1/x + x$ by various methods; $x_0 = 2$, $[a, b] = [1.9, 2.1]$

Method		Width of Bound Interval
Intervals	$n_d = 1$	0.25012531
	$n_d = 10^4$	0.14988476
	$n_d = 10^8$	0.14987468
Taylor models	3rd order	0.14987903
	6th order	0.14987468
Exact		0.14987468

Table 1 shows the widths of the bound interval for a simple example function $f(x) = 1/x + x$ in the domain $[1.9, 2.1]$ around the reference point $x_0 = 2$, for the exact value, the method of Taylor models and the divided interval method, where n_d indicates the number of division of the domain interval. In the case of simple interval method, to achieve the sharpness of the third-order Taylor model, the domain has to be split into about $24,000$ subintervals. More important in practice is the case of several variables, where the situation becomes more dramatic. Table 2 illustrates the computational effort by estimating the required number of floating-point operations, for a simple example function of six variables like $f(\vec{x}) = \sum_j (1/x_j + x_j)$.

Implementation in the program COSY INFINITY [5,6,8,9] has begun, and we have been working on the problem to estimate the long-term stability of weakly nonlinear systems in connection with the design of storage rings [10,14]. The problem involves rather complicated functions of about 10^5 floating-point operations, which are polynomials with six variables and up to roughly 500th order; many large terms cancel each other, and very small fluctuations have to be estimated. While the sharpness of the bounds in question is important in order to guarantee a large number of stable turns, in reality these functions

Table 2: The total number of FP operations required to rigorously bound a simple function like $f(\vec{x}) = \sum_j (1/x_j + x_j)$

	One Dimensional	Six Dimensional
Interval	~ 10	~ 10
10^4 divided intervals	$\sim 10^5$	$\sim 10^{25}$
3rd order Taylor model	~ 10	$\sim 10^4$

have a very large number of local maxima; hence, an exact estimate of their bounds requires careful treatment. We have tried the method of conventional interval optimization [12,13,15,16] and optimization based on Remainder Differential Algebras, and the results were compared with the approximations by a tight rastering in real arithmetic, which merely gives optimistic, nonguaranteed estimates. The method of Remainder Differential Algebras gives a satisfactory result and is far superior to interval bounding [10,11,14], and thus seems to offer the key to solving the long-term stability problem rigorously for the first time.

References

1. M. Berz. Differential algebraic description of beam dynamics to very high orders. *Particle Accelerators*, 24:109, 1989.
2. M. Berz. Arbitrary order description of arbitrary particle optical systems. *Nuclear Instruments and Methods*, A298:426, 1990.
3. M. Berz. Forward algorithms for high orders and many variables with application to beam physics. In A. Griewank and G. F. Corliss, editors, *Automatic Differentiation of Algorithms: Theory, Implementation, and Application*, pages 147–156. SIAM, Philadelphia, Penn., 1991.
4. M. Berz. *High-Order Computation and Normal Form Analysis of Repetitive Systems, in: M. Month (Ed), Physics of Particle Accelerators*, volume AIP 249, page 456. American Institute of Physics, 1991.
5. M. Berz. COSY INFINITY Version 6. In *M. Berz, S. Martin and K. Ziegler (Eds.), Proc. Nonlinear Effects in Accelerators*, page 125. IOP Publishing, 1992.
6. M. Berz. New features in COSY INFINITY. In Robert Ryne, editor, *AIP Conference Proceedings 297, Computational Accelerator Physics*, pages 267–278, New York, 1993. American Institute of PHysics.
7. M. Berz. Modern map methods for charged particle optics. *Nuclear Instruments and Methods*, 352, 1994.
8. M. Berz. COSY INFINITY Version 7 reference manual. Technical Report MSUCL-977, National Superconducting Cyclotron Laboratory, Michigan State University, East Lansing, MI 48824, 1995.
9. M. Berz, K. Fuchi, K. Shamseddine, G. H. Hoffstätter, and W. Wan. COSY INFINITY and its applications to nonlinear dynamics. In M. Berz, C. Bischof, G. Corliss, and A. Griewank, editors, *Computational Differentiation: Techniques, Applications, and Tools*. SIAM, Philadelphia, Penn., 1996.
10. M. Berz and G. Hoffstätter. Exact estimates of the long term stability of weakly nonlinear systems applied to the design of large storage rings. *Interval Computations*, 2:68–89, 1994.
11. K. Fuchi and M. Berz. Remainder differential algebras and their applications. In M. Berz, C. Bischof, G. Corliss, and A. Griewank, editors, *Computational Differentiation: Techniques, Applications, and Tools*. SIAM, Philadelphia, Penn., 1996.
12. E. R. Hansen. Global optimization using interval analysis – the one–dimensional case. *J. Optim. Theor. and Appl.*, 29:331–334, 1979.
13. E. R. Hansen. An overview of global optimization using interval analysis. In Ramon E. Moore, editor, *Reliability in Computing*, pages 289–307. Academic Press, New York, 1988.
14. G. H. Hoffstätter. *Rigorous bounds on survival times in circular accelerators and efficient computation of fringe–field transfer maps*. PhD thesis, Michigan State University, East Lansing, Michigan, USA, 1994. also DESY 94-242.
15. K. Ichida and Y. Fujii. An interval arithmetic method for global optimization. *Computing*, 23:85–97, 1979.
16. C. Jansson. A global optimization method using interval arithmetic. *IMACS Annals of Computing and Applied Mathematics*, 1992.

COMPUTATION OF DERIVATIVES WHEN ALL OTHER METHODS FAIL

Khodr Shamseddine and Martin Berz

1. Introduction

The general question of efficient differentiation is at the core of a significant part of the work on aberrations and perturbation theories relevant in Beam Physics. In this case, derivatives of highly complicated functions have to be computed to high orders. However, even when the derivative of the function is known to exist at the given point, numerical methods fail to give an accurate value of the derivative; the error increases with the order, and for orders greater than three, the error usually becomes too large for the results to be practically useful. On the other hand, while formula manipulators like Mathematica are successful in finding low-order derivatives of simple functions, they fail for high-order derivatives of very complicated functions. Consider, for example, the function

$$g(x) = \frac{\sin\left(x^3+2x+1\right) + \frac{3+\cos(\sin(\ln|1+x|))}{\exp\left(\tanh\left(\sinh\left(\cosh\left(\frac{\sin(\cos(\tan(\exp(x))))}{\cos(\sin(\exp(\tan(x+2))))}\right)\right)\right)\right)}}{2+\sin\left(\sinh\left(\cos\left(\tan^{-1}\left(\ln\left(\exp(x)+x^2+3\right)\right)\right)\right)\right)}. \tag{1}$$

Using Differential Algebras [1] implemented in COSY INFINITY [4,6], we find $g^{(n)}(0)$ for $0 \leq n \leq 19$. These numbers are listed in table (1); we note that for, $0 \leq n \leq 19$, we list the CPU time needed to

Order n	$g^{(n)}(0)$	CPU Time
0	1.004845319007115	1.820 msec
1	0.4601438089634254	2.070 msec
2	−5.266097568233224	3.180 msec
3	−52.82163351991485	4.830 msec
4	−108.4682847837855	7.700 msec
5	16451.44286410806	11.640 msec
6	541334.9970224757	18.050 msec
7	7948641.189364974	26.590 msec
8	−144969388.2104904	37.860 msec
9	−15395959663.01733	52.470 msec
10	−618406836695.3634	72.330 msec
11	−11790314615610.74	97.610 msec
12	403355397865406.1	128.760 msec
13	$0.5510652659782951 \times 10^{17}$	168.140 msec
14	$0.3272787402678642 \times 10^{19}$	217.510 msec
15	$0.1142716430145745 \times 10^{21}$	273.930 msec
16	$-0.6443788542310285 \times 10^{21}$	344.880 msec
17	$-0.5044562355111304 \times 10^{24}$	423.400 msec
18	$-0.5025105824599693 \times 10^{26}$	520.390 msec
19	$-0.3158910204361999 \times 10^{28}$	621.160 msec

Table 1: $g^{(n)}(0), 0 \leq n \leq 19$, computed with DA

obtain all derivatives of g at 0 up to order n and not just $g^{(n)}(0)$. For comparison purposes, we give in table (2) the function value and the first six derivatives computed with Mathematica. Note that the respective values listed in tables (1) and (2) agree. However, Mathematica used a much longer CPU time to compute the first six derivatives, and it failed to find the seventh derivative as it ran out of memory. We also list in table (3) the first ten derivatives of g at 0 computed numerically using the numerical differentiation formulas

$$g^{(n)}(0) = (\Delta x)^{-n} \left(\sum_{j=0}^{n} (-1)^{n-j} \begin{pmatrix} n \\ j \end{pmatrix} g(j\Delta x) \right), \quad \Delta x = 10^{-16/(n+1)}, \tag{2}$$

for $1 \leq n \leq 10$, together with the corresponding relative errors obtained by comparing the numerical values with the respective ones computed with DA or Mathematica.

Order n	$g^{(n)}(0)$	CPU Time
0	1.004845319007116	0.11 sec
1	0.4601438089634254	0.17 sec
2	−5.266097568233221	0.47 sec
3	−52.82163351991483	2.57 sec
4	−108.4682847837854	14.74 sec
5	16451.44286410805	77.50 sec
6	541334.9970224752	693.65 sec

Table 2: $g^{(n)}(0), 0 \leq n \leq 6$, computed with Mathematica

Order n	Δx	$g^{(n)}(0)$	Relative Error
1	1×10^{-8}	0.4601437841866840	54×10^{-9}
2	464×10^{-8}	−5.266346392944456	47×10^{-6}
3	1×10^{-4}	−52.83767867680922	30×10^{-5}
4	63×10^{-5}	−87.27214664649106	0.20
5	215×10^{-5}	19478.29555909866	0.18
6	518×10^{-5}	633008.9156614641	0.17
7	0.01	−12378052.73279768	2.6
8	167×10^{-4}	−1282816703.632099	7.8
9	251×10^{-4}	83617811421.48561	6.4
10	351×10^{-4}	91619495958355.24	149

Table 3: $g^{(n)}(0), 1 \leq n \leq 10$, computed numerically

Even the Differential Algebraic methods known for the fast and accurate computation of derivatives of complicated functions in a computer environment fail to find the derivatives of certain functions at given points even though the functions are differentiable at the respective points. This is mostly connected to the fact that Differential Algebras do not admit multiplicative inverses for every nonzero number, nor do they admit roots for every positive number. For example, the functions

$$g_1(x) = x^2\sqrt{|x|} \cdot \frac{\sin\left(x^3+2x+1\right) + \frac{3+\cos(\sin(\ln|1+x|))}{\exp\left(\tanh\left(\sinh\left(\cosh\left(\frac{\sin(\cos(\tan(\exp(x))))}{\cos(\sin(\exp(\tan(x+2))))}\right)\right)\right)\right)}}{2+\sin\left(\sinh\left(\cos\left(\tan^{-1}\left(\ln\left(\exp(x)+x^2+3\right)\right)\right)\right)\right)} \text{ and} \tag{3}$$

$$g_2(x) = \begin{cases} \frac{1-\exp(-x^2)}{x} \cdot \frac{\sin(x^3+2x+1)+\frac{3+\cos(\sin(\ln|1+x|))}{\exp\left(\tanh\left(\sinh\left(\cosh\left(\frac{\sin(\cos(\tan(\exp(x))))}{\cos(\sin(\exp(\tan(x+2))))}\right)\right)\right)\right)}}{2+\sin(\sinh(\cos(\tan^{-1}(\ln(\exp(x)+x^2+3)))))} & \text{if } x \neq 0 \\ 0 & \text{if } x = 0 \end{cases} \tag{4}$$

are both differentiable at 0; but the attempt to compute their derivatives using Differential Algebraic methods or formula manipulators fails. This is not specific to g_1 and g_2, and is generally connected to the occurrence of nondifferentiable parts that do not affect the differentiability of the end result, of which case g_1 is an example, as well as the occurrence of branch points in coding as in IF-ELSE structures, of which case g_2 is an example.

A part of our research on the nonarchimedean field $\mathcal{R}$ [2,3,5], a field extension of R that contains ${}_nD_1$ for each positive integer n, studies many of the general problems connected to computational differentiation in a broader sense than what is necessary for conventional Beam Physics [5,7]. Using the calculus on $\mathcal{R}$, we formulate a necessary and sufficient condition for the derivatives of functions from R into R representable on a computer to exist, and show how to find these derivatives whenever they exist.

2. Computer Environment Functions

In this section we define a large class of functions, the class of computer functions, and state a few results about their smoothness properties, whose proofs can be found in [7]. A function $f : R \to R$ will be called a computer function if it can be obtained from intrinsic functions and the Heaviside function through a finite number of arithmetic operations $(+, \cdot)$ and compositions. For the sake of convenience, the intrinsic functions are assumed to include the reciprocal function.

Since we will be studying only computer functions, it will be useful to define the domain D_c of computer numbers; that is, the domain of the real numbers representable on a computer: If l and L denote, respectively, the lower and upper bounds of the positive real numbers representable on the computer, then $D_c = [-L, -l] \cup [l, L] \cup \{0\}$.

If f is a computer function, then its domain D of definition (continuity) in D_c is a finite union of intervals; furthermore, the system $\{f(x) \in I;\ x \in D_c\}$, where $I \subset D_c$ is an interval, has as a solution a finite union of intervals in D_c. Since the family of computer functions is closed under differentiation to any order n, the statement holds as well for derivatives of computer functions.

In the following, we give a standard representation of any computer function f around any fixed point x_0 of its domain of definition, which will be of crucial importance in studying the differentiability of f at x_0: Given a real computer function f, there exist mutually disjoint intervals $I_1, \ldots, I_M$ in D, the domain of definition of f in $D_c = [-L, -l] \cup [l, L] \cup \{0\}$, such that $\bigcup_{k=1}^{M} I_k = D$, and if x_0 is an interior point of I_k then there exists a positive real number σ such that, for $0 < x < \sigma$,

$$f(x_0 \pm x) = A_0^{\pm}(x) + \sum_{i=1}^{i_k^{\pm}} x^{q_i^{\pm}} A_i^{\pm}(x), \tag{5}$$

where $A_i^{\pm}(x), 0 \leq i \leq i_k^{\pm}$, is a power series in x with a positive radius of convergence, $A_i^{\pm}(0) \neq 0$ for $i = 1, \ldots, i_k^{\pm}$, and the $q_i^{\pm}$'s are nonzero rational numbers that are not positive integers. Since the family of computer functions is closed under differentiation to any order n, the statement holds for derivatives of computer functions as well.

To be able to use the calculus on $\mathcal{R}$ to compute derivatives of real computer functions, we first need to extend this class of functions into the new field $\mathcal{R}$: If f is a real computer function, then f is given around any given real point of its domain of definition in D_c by a finite combination of roots and power series. Since roots and power series have already been extended to $\mathcal{R}$ [2,3,5], f is extended to $\mathcal{R}$ in a natural way similar to that of the extension of power series from R to C.

3. Computation of Derivatives

Using the results of the previous section, we now have criteria to check the order of differentiability of a real computer function f at a given point x_0 of its domain of definition and to accurately compute all existing derivatives. We state the following results whose proofs are given in [7].

Let f be a computer function. Then f is defined at x_0 if and only if $f(x_0)$ can be computed on a computer.

If x_0 is such that $f(x_0-d)$, $f(x_0)$, and $f(x_0+d)$ are all defined, where d is the positive infinitely small number introduced in [2,3,5], then f is continuous at x_0 if and only if $f(x_0-d) =_0 f(x_0) =_0 f(x_0+d)$. If $f(x_0)$ and $f(x_0+d)$ are defined, but $f(x_0-d)$ is not, then f is continuous at x_0 if and only if $f(x_0+d) =_0 f(x_0)$. Finally, if $f(x_0)$ and $f(x_0-d)$ are defined, but $f(x_0+d)$ is not, then f is continuous at x_0 if and only if $f(x_0-d) =_0 f(x_0)$.

Now, let f be continuous at x_0, and let $f(x_0-d)$ and $f(x_0+d)$ be both defined. Then f is differentiable at x_0 if and only if $\{f(x_0+d)-f(x_0)\}/d$ and $\{f(x_0)-f(x_0-d)\}/d$ are both at most finite in absolute value and their real parts agree. In this case,

$$\frac{f(x_0+d)-f(x_0)}{d} =_0 f'(x_0) =_0 \frac{f(x_0)-f(x_0-d)}{d}. \tag{6}$$

In general, if f is $(n-1)$ times differentiable at x_0, $n \geq 2$, then f is n times differentiable at x_0 if and only if

$d^{-n}\left(\sum_{j=0}^{n}(-1)^{n-j}\binom{n}{j} f(x_0+jd)\right)$ and $d^{-n}\left(\sum_{j=0}^{n}(-1)^{j}\binom{n}{j} f(x_0-jd)\right)$ are both at most finite in

absolute value and their real parts agree. In this case

$$d^{-n}\left(\sum_{j=0}^{n}(-1)^{n-j}\binom{n}{j} f(x_0+jd)\right) =_0 f^{(n)}(x_0) =_0 d^{-n}\left(\sum_{j=0}^{n}(-1)^{j}\binom{n}{j} f(x_0-jd)\right). \tag{7}$$

The last result in this section follows from the fact that knowledge of $f(x_0-d)$ and $f(x_0+d)$ gives us all the information about a computer function f in a real positive radius σ around x_0; it states that, from the mere knowledge of $f(x_0-d)$ and $f(x_0+d)$, we can find at once the order of differentiability of f at x_0 and the accurate values of all existing derivatives: If f is a computer function that is continuous at x_0, then f is n times differentiable at x_0 if and only if $f(x_0-d)$ and $f(x_0+d)$ are both defined and can be written as

$$f(x_0-d) =_n f(x_0)+\sum_{j=1}^{n}(-1)^j a_j d^j \text{ and } f(x_0+d) =_n f(x_0)+\sum_{j=1}^{n} a_j d^j, \tag{8}$$

where the a_j's are real numbers. Moreover, in this case $f^{(j)}(x_0) = j!\, a_j$ for $1 \le j \le n$.

The methods discussed above for computing derivatives of real computer functions can be of practical use only if we can implement the $\mathcal{R}$ numbers on a computer. We do have a first version of the implementation using COSY INFINITY [4,6], a brief outline of which is shown in [7].

4. Examples

In the following, we apply the results of the previous section to find the order of differentiability and all existing derivatives at 0 of the two functions already mentioned in the introduction, Eqs. (3) and (4), which are clearly computer functions. Consider first the function $g_1(x)$. If we input the values $x = -3d, -2d, -d, 0, d, 2d, 3d$, we obtain the following output up to depth 3

$$g_1(\pm 3d) =_3 15.66398831641272 d^{5/2} \tag{9}$$

$$g_1(\pm 2d) =_3 5.684263512907927 d^{5/2} \tag{10}$$

$$g_1(\pm d) =_3 1.004845319007115 d^{5/2} \tag{11}$$

$$g_1(0) = 0. \tag{12}$$

Since $g_1(-d) =_0 g_1(0) =_0 g_1(d)$, g_1 is continuous at 0. A simple computation shows that $\{g_1(d) - g_1(0)\}/d =_0 0 =_0 \{g_1(0) - g_1(-d)\}/d$, from which we infer that g_1 is differentiable at 0, with $g_1'(0) = 0$. Also $\{g_1(2d) - 2g_1(d) + g_1(0)\}/d^2 =_0 0 =_0 \{g_1(0) - 2g_1(-d) + g_1(-2d)\}/d^2$, from which we conclude that g_1 is twice differentiable at 0, with $g_1^{(2)}(0) = 0$. On the other hand, $\{g_1(3d) - 3g_1(2d) + 3g_1(d) - g_1(0)\}/d^3 \sim d^{-1/2}$, which entails that $|(g_1(3d) - 3g_1(2d) + 3g_1(d) - g_1(0))/d^3|$ is infinitely large. Hence g_1 is not three times differentiable at 0.

By evaluating $g_2(-d)$ and $g_2(d)$ up to any fixed depth and applying the last result of the previous

Order n	$g_2^{(n)}(0)$	CPU Time
0	0.	3.400 msec
1	1.004845319007115	4.030 msec
2	0.9202876179268508	5.710 msec
3	−18.81282866172102	8.240 msec
4	−216.8082597872205	12.010 msec
5	−364.2615904917884	17.570 msec
6	101933.1724529188	25.150 msec
7	3798311.370563978	35.700 msec
8	60765353.84260825	49.790 msec
9	−1441371402.871872	67.210 msec
10	−156736847166.3961	89.840 msec
11	−6725706835826.155	118.950 msec
12	−131199307184575.8	154.530 msec
13	5770286440090848.	200.660 msec
14	$0.7837443136320079 \times 10^{18}$	256.460 msec
15	$0.4850429351252696 \times 10^{20}$	321.630 msec
16	$0.1734774579876559 \times 10^{22}$	400.140 msec
17	$-0.1757849296527536 \times 10^{23}$	478.940 msec
18	$-0.9350429649226352 \times 10^{25}$	582.150 msec
19	$-0.9521402181303937 \times 10^{27}$	702.390 msec

Table 4: $g_2^{(n)}(0), 0 \le n \le 19$, computed with $\mathcal{R}$ calculus

section, we obtain that g_2 is differentiable at 0 up to arbitrarily high orders. In table (4), we list only the function value and the first nineteen derivatives of g_2 at 0, together with the CPU time needed to compute all derivatives up to the respective order. The numbers in table (4) were obtained using the implementation of $\mathcal{R}$ in COSY INFINITY [4,6].

References

1. M. Berz. Differential algebraic description of beam dynamics to very high orders. *Particle Accelerators*, 24:109, 1989.
2. M. Berz. Automatic differentiation as nonarchimedean analysis. In *Computer Arithmetic and Enclosure Methods*, Amsterdam, 1992. Elsevier Science Publishers.
3. M. Berz. Analysis on a nonarchimedean extension of the real numbers. Lecture Notes, Studienstiftung Summer School, September 1992 MSUCL-933, National Superconducting Cyclotron Laboratory, Michigan State University, East Lansing, MI 48824, 1994.
4. M. Berz. COSY INFINITY Version 7 reference manual. Technical Report MSUCL-977, National Superconducting Cyclotron Laboratory, Michigan State University, East Lansing, MI 48824, 1995.
5. M. Berz. Calculus and numerics on Levi-Civita fields. *Computational Differentiation: Techniques, Applications, and Tools*, Martin Berz, Christian Bischof, George Corliss, and Andreas Griewank, eds., SIAM, 1996.
6. M. Berz, G. Hoffstätter, W. Wan, K. Shamseddine, and K. Fuchi. COSY INFINITY and its applications to nonlinear dynamics. *Computational Differentiation: Techniques, Applications, and Tools*, Martin Berz, Christian Bischof, George Corliss, and Andreas Griewank, eds., SIAM, 1996.
7. K. Shamseddine and M. Berz. Exception handling in derivative computation with nonarchimedean calculus. *Computational Differentiation: Techniques, Applications, and Tools*, Martin Berz, Christian Bischof, George Corliss, and Andreas Griewank, eds., SIAM, 1996.

USE OF A HELMHOLTZ RESONATOR TO VERIFY AND DAMP THERMAL ACOUSTIC OSCILLATIONS IN THE 50 LITER LIQUID HELIUM CRYOVESSEL

Jeff Schubert

Thermal acoustic oscillations (TAOs) are a well known nuisance in the construction of dewars and cryostats. The low frequency (on the order of 10–60 Hz) oscillations which occur in pipes that connect warm and cold sections of a cryostat have been blamed for transferring energy to the cold end of the pipes and for rendering precise pressure measurements impossible.[1,2]

Although most of the literature only discusses the existence of TAOs in static columns of gas, we believe that we have observed the same phenomenon in pipes with over 2 L/min of gas flow. At first the pressure of the gas exiting from the radiation shields of the cryovessel oscillated with a frequency between 6 and 7 Hz, depending on the temperature of the shields. Although the oscillation did not noticeably effect the boiloff rate, it did interfere with both pressure and flow measurements. The floating ball in the rotometer flowmeter oscillated with an amplitude that varied from 5% of the reading to greater than the full scale of the flowmeter. Similar oscillations in static columns have been known to increase the heatload on a cryostat by three orders of magnitude. [2]

We set out to damp the oscillations by installing a Helmholtz resonator as a side branch to the pipe that carries the helium away from the cryovessel. The Helmholtz resonator is simply a surge tank connected by a capillary to the side of the pipe that carries the TAO. This device destroys the resonant quality of the pipe so that acoustic standing waves in a given frequency range will be minimized. Since the resonator can work at the warm end of the vent pipe, it may be located outside the cryovessel, wherever space is available.

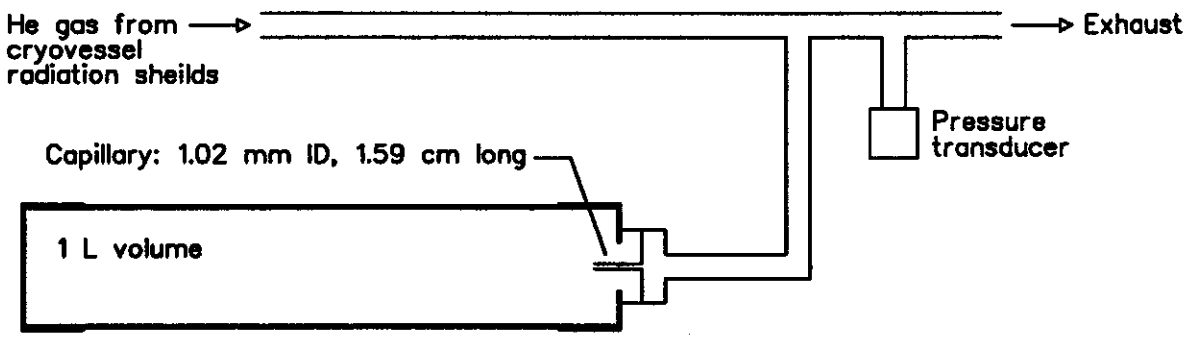

Figure 1: Schematic of the Helmholtz resonator for damping thermoacoustic oscillations.

A schematic of the resonator is shown in figure 1. The volume of the surge tank and the dimensions of the capillary are based on the recipe reported by Tward and Mason,[1] with the exception of the radius of the capillary. Because there is a unit error in the equation reported in Tward and Mason's paper, we used the relationship $a^2 < \mu/\rho\omega$ where a is the radius of the capillary, μ and ρ are the viscosity and density of helium at the resonator, and $2\pi\omega$ is the frequency of the TAO.

As soon as the Helmholtz resonator was installed the TAO disappeared. In order to study the effect of the damper, we installed a valve between it and the rest of the system. Figure 2 is a strip-chart recording

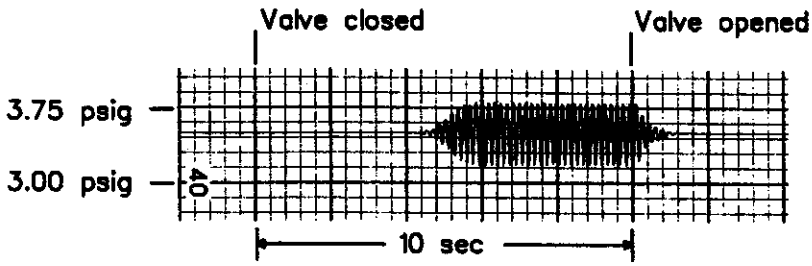

Figure 2: The pressure of the exhaust helium gas, measured outside the vessel, as the valve to the Helmholtz resonator is closed and then opened. The frequency of the oscillation is 6.25 Hz.

of the signal from a pressure transducer located near the Helmholtz resonator. When the radiation shields reached equilibrium the valve was closed, removing the damper from the system. After a period of time that ranged from less than one second to seven or more seconds, the oscillations reappeared. When the valve was opened, the oscillations began to decay immediately and were undetectable after one second.

With the resonator in operation pressure and flow measurements of the exiting gas became routine and the TAO phenomenon was ruled out as a significant source of heatload to the cryovessel. The same method detailed here should be capable eliminating oscillations that transfer heat to the inside of a cryostat.

References

1. E. Tward and P.V. Mason, Damping of thermoacoustic oscillations, *Adv. Cryo. Eng.* 27:807 (1982).
2. D.A. Ditmars and G.T. Furukawa, Detection and damping of thermal-acoustic oscillations in low-temperature measurements, *Jour. Res. NBS-C* 69C:35 (1964).

CALCULATIONS AND MEASUREMENTS IN THE K500 CENTRAL REGION

S.L. Snyder and F. Marti

An axial injection and central region system have been designed and constructed that meet the operating requirements for the K500⊗K1200 coupling project. The spiral inflector has been redesigned to account for the new scaling law, and a second harmonic central region has been devised. Computer calculations of the vertical focusing and radial centering properties of this central region have been performed, the results of which show good performance in both respects.

Calculations of the overall behavior of the axial injection and central region system show the production of a well-behaved beam. The centering error for the simulated beam is minimal as full energy is reached without the phase space distortions which accompany a miss-centered beam. In the simulations, the phase width has been reduced to 3° FWHM, and with the use of both the first and second harmonic bunchers, 6% of the input DC beam reaches full energy. The second harmonic buncher should give a factor of 2 increase in the transmitted beams and should certainly be used in the final system. The extraction bump, in conjunction with the final phase-reduced beam, produced good turn separation at extraction and a 2.2π mm-mrad emittance.

The above mentioned designs have been built and installed in the K500 cyclotron. During initial operations with the new inflector and central region, beam has been successfully accelerated up to full energy and extracted. The beam has been successfully centered through the use of the first harmonic bump coils. Comparisons of the calculated turn positions versus the observed values (using the main probe) show good agreement when a full range of starting times is used. The operating and calculated dee voltages needed to get such agreement differ and at this point it is not clear whether this is due to an uncertainty in the voltage calibration of the K500 monitoring system, a variation between the actual and assumed starting conditions, or motion of the dee tips. Certainly, the dee tip motion will present a problem and as such should be addressed during the K500 upgrades.

The first turn slit has been placed according to computer simulations, and the phase-reduced beam produced has been accelerated to extraction. Observations of the enhancement of the turn separation caused by the slit have been made as were internal timing measurements of the beam. The introduction of the phase pins allowed a further reduction in the phase spread of the beam thereby producing separated turns throughout the machine. In this way, the measured phase spread of the beam has been reduced to 2.5° FWHM. Transmission calculations on a 5° FWHM beam have shown that the first harmonic buncher increases the current by a factor of five and places nearly 8% of the input current into the reduced width. The instability of the RF system and the lack of a working second harmonic buncher limited the testing of the design.

Improvements to the RF supplies and mechanical systems need to be made to increase the stability of the machine and to limit the motion of the dee tips.

K1200 VACUUM STUDIES

P. Miller, D. Lawton, A. McCartney, F. Marti and D. Poe

Beam Loss from Charge Changing Collisions

The present upgrade plan of the NSCL requires the coupling of the K500 and K1200 superconducting cyclotrons, with the K500 beam injected by stripping inside a dee of the K1200. The installation of the stripper mechanism inside the dee prevents the operation of a possible third cryopanel inside that same dee. The loss of transmitted beam intensity in a cyclotron due to charge changing collisions with the residual gas molecules involves the cross sections for the loss process over a wide range of energy per nucleon (E/A typically 0.015 Q/A at injection to 1000 $(Q/A)^2$ at extraction in the K1200). In the operating pressure range, the beam loss is non-linear with pressure for ions that have large cross sections, such as U^{35+}. We performed an experiment in which the beam intensity out of the cyclotron was measured with one cryopump bypassed and compared this to the normal configuration, with and without gas being added to the vacuum through an external valve and flow meter. We measured the pressure in the beam chamber with a nude ion gauge fitted to a beam probe with the magnet carefully degaussed. See Fig. 1. Additional experiments were performed with other ions to study the validity of empirical formulas for vacuum attenuation of the beam. A report on this project is being published. [1]

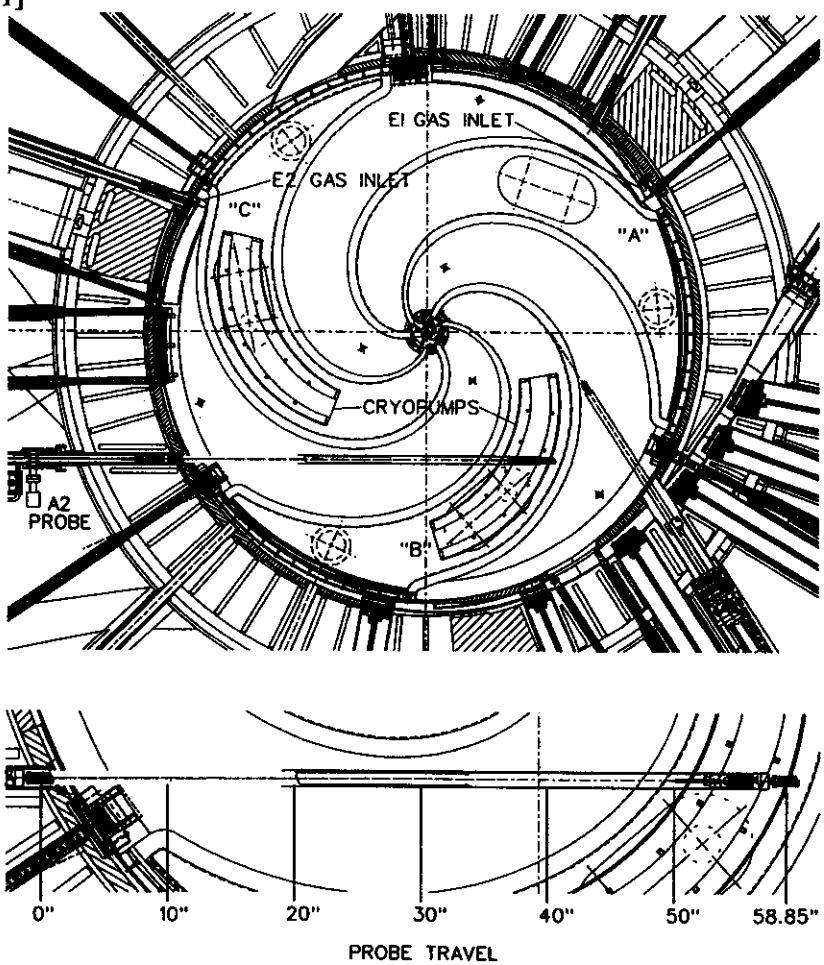

Fig. 1: Plan view of K1200 with detail of the path of the vacuum probe.

The pressure inside the cyclotron (measured by the nude ionization gauge mounted on a probe) is lower than the pressure read by the external ionization gauge by roughly a factor of 3. The pressure above the cryopump (inside the dee) is slightly lower than the pressure over the magnet pole. The empirical formulas for vacuum attenuation of the beam agree only roughly (within about a factor of 3 in pressure) with the measured beam attenuation. This accuracy is sufficient to estimate the pressure range needed for good performance. The present vacuum conditions in the K1200 cyclotron (10^{-6} torr) will be adequate for the future coupled cyclotron project. The K500 vacuum system will be upgraded to operate at 0.5 to 1 x 10^{-7} torr to reduce beam attenuation to less than 5% loss.

Pumping Modifications

The cryopumps in the K1200 are copper panels cooled to approximately 8K with liquid helium. They were not designed to pump hydrogen or helium; the turbomolecular pumps served that purpose. We found that high power operation of the rf system was causing the release of so much hydrogen into the vacuum chamber that it was causing problems for the rf. The residual gas analyzer gave a semi-quantitative measure of the partial pressures of the vacuum gas constituents.

We applied activated charcoal pellets to the cryopanels to provide sorption pumping for hydrogen. This was successful in holding the hydrogen partial pressure to about 1% of the pressure observed previously during high power rf. The problem was solved. We have indications that the endurance of the pumps is roughly 1 month (before they require a 2 hour warm-up cycle to regenerate them.)

The 500 l/s turbomolecular pumps on the cyclotron were replaced with new 140 l/s pumps. The old pumps were transferred to other systems which require the larger pumping speed. (On the K1200 the effective pumping speed for air was limited by the conductance of the connection through the magnet pole to 78 l/s.) The new pumps are also easier to maintain.

Additional Pumping for Liner Vacuum

The existence of a leak between the liner vacuum (around the trim coils) and the beam chamber vacuum was confirmed, but attempts to eliminate it have been unsuccessful. Several leaking indium seals under the heads of mounting screws that penetrate the liner on the magnet hills were fixed, but pressure measurements show that the two vacuum volumes are still coupled. The standard liner pump is an Edwards model E2M8, with a pumping speed of 11.5 m^3/hr. We connected a Welch model 1397, with pumping speed 29 m^3/hr, via a short tube to a tee on the liner manifold, and this lowered the pressure by a factor of 3. The liner's contribution to the pressure in the beam chamber is estimated by the liner pressure (600 millitorr) and the coupling coefficient (0.23 x 10-6) as 1.4 x 10^{-7} torr, or about 1/7 of the normal beam chamber pressure.

Reference

1. Beam Loss from Charge Changing Collisions in a Cyclotron, P. Miller, D. Lawton and F. Marti in *Cyclotrons '95*, Proc. of 14th International Conf. on Cyclotrons and Their Applications, Oct. 1995, Capetown (to be published by World Scientific Publishing Co.)

ELECTROSTATIC DEFLECTOR DEVELOPMENT

P. Miller, H. Blosser, T. Grimm, F. Marti, D. Poe and G. Stork

Deflector Modifications to Allow Higher Beam Intensity

The demand for higher intensity beams for radioactive secondary beam production has motivated us to step up R & D work on increasing the beam power that the first deflector E1 can transmit. On its last turn in the cyclotron the beam overlaps the previous turn, and the extraction efficiency is between 30% and 60%. Most of the power of the intercepted beam is dissipated in the septum, until recently a molybdenum sheet 0.010 inches thick. The short range of the particles (usually < 3 mm) implies that a small area of the septum is heated. Heat dissipation by conduction to the support structure is negligible compared to that due to radiation. The heat produced by beam loss is concentrated at the leading edge of the septum. This heat is radiated to the cathode and to other nearby parts. The cathode has no effective cooling path, while the deflector housing and the cyclotron liner are water cooled. A typical operating condition for producing radiaoctive beams is 0.4 electrical microampere of 100 MeV/u $^{18}O^{6+}$ (120 W). We have occasionally operated with output up to 200 W, but usually the deflector becomes unstable and loses efficiency above 120-150 W output.

The problems encountered are: (1) leakage current increases when beam is turned on (both prompt and delayed, i.e. thermal response observed), (2) the high voltage connection to the cathode gets hot enough to melt the polyethylene insulation of the cable to the power supply, (3) induced radioactivity produces a dose rate at the surface of the deflector of 50 rad/hr 1 day after shutdown. Runaway leakage current at high beam current (problem (1) above) usually determines the practical limit on beam intensity, since item (2) has been addressed by externally cooling the high voltage feed cable and item (3) is mitigated by use of remote handling tools to remove the deflector to a shielded storage area. The removable radioactive contamination that remains in the cyclotron is a potentially greater radiation exposure hazard for workers than the removal of the deflectors.

The cathode support insulators are being replaced with ones made of BeO to provide indirect cooling of the cathode. Four such insulators have been installed in the cyclotron. The previous insulators were made of Macor machinable glass ceramic, which has very good electrical properties but negligible heat conduction. A liquid cooled feedthrough was installed on E1; it is described in another paper in this annual report.

Making the septum thinner than 10 mils was predicted to reduce the amount of heat produced in the septum and thereby reduce its temperature. This was confirmed in a test where two sample strips of septum material were mounted in the beam line side by side and bombarded while they were observed on television. The 10 mil thick sample was heated to glowing, but the 5 mil sample did not get hot enough to glow under the same beam conditions. We have just installed a 5 mil septum on E1 and find similar extraction efficiency as before (possibly limited by mechanical errors in the deflector) and evidence of less power dissipation. A television was installed to view the septum through a glass view port on the opposite side of the cyclotron. The heating of the 10 mil thick septum by the beam gave a bright light at maximum usable beam intensity. The 5 mil septum did not emit a detectable glow even when the beam was twice as intense (300 W). The 5 mil septum will be tested with higher beam power in the future. Its beam power handling limit has not yet been observed. Further experience will provide a determination of the maximum power level and the relationship to cathode voltage.

Fig. 1 shows the melting of the 10 mil septum that occurred when it was tested to destruction. The deformed septum was placed between flat plates to measure the effective thickness of the warped

regions beginning 0.2" above and below the median plane. The result was 0.03" to 0.05". The metal "ball" that remained at the end of the slot was 0.06" thick.

Fig. 1: Photograph of leading edge of the septum (0.010 in. thick Mo) melted by a 100 MeV/u $^{20}Ne^{6+}$ pulsed beam. When melting started the duty factor was 40%, the internal beam current was 10 euA and the extracted beam current was 3.5 euA (1200 W x 40%= 480 W). The height of the septum was 64 mm.

We expected the beam losses to be sensitive to small changes in the septum shape, such as are caused by thermal expansion of the septum, and to small misalignments of the segments of the septum. We have modeled in 3D the deformation of the septum under the influence of the electric pressure for several different thicknesses and mechanical constraints at the edges. We plan to use the model to investigate the effect of thermal expansion. These results will be used to guide experiments testing alternative mechanical solutions for optimized system performance.

To visualize beam impact areas we exposed film to the beta- and gamma radiation from the radioactivity induced by the beam. We used Kodak type XRP-2 medical X-ray film (33 x 41 cm) when its high sensitivity is needed. It is packaged in a sealed paper envelope which allows handling in the light. An exposure of 10 mrad (estimated from the radiation intensity measured with an ion chamber near contact) was sufficient. Initially, the deflector was too radioactive, and the optimum exposure time was impractically short. In that situation we were able to use 35 mm photographic film (Tri-X), at an exposure of 1 rad. We transferred the film to an opaque envelope in total darkness and supported it in contact with the septum on a fixture that was inserted and removed using long handles to reduce personal exposure. Polaroid Type 57 film is also convenient to use to autoradiograph small areas, up to 10 cm across.

In the near future we plan to test a deflector section with several improvements. The cathode will be shortened so that an aluminum block can be placed upstream from the cathode to shield it from the thermal radiation from the hot edge of the septum. This block will also help support the septum above and below the median plane. A thinner septum (2 or 3 mil) will be tried with as much support as possible to keep it flat and resist the electric pressure. The electric field at the ends of the cathode will be reduced by increasing the gap there a few mm. The plates that support the septum and the cathode will be fitted with dowels for greater mechanical accuracy, and the heat conduction to the cooling water will be improved.

In summary, recent experience using a 5 mil thick septum suggests that the power in the external beam can be increased by a factor of two (to 300 W). Other improvements are being made which are expected to provide additional gains. An increase in the amount of neutron shielding will be needed in

some cases to utilize the higher intensity. (For some He beams we are already limited by neutron radiation.)

Series resistor for deflector power supplies

A resistor string with total resistance 50 megohms and rated for 100 kV was installed in series with each deflector power supply. Its purpose was to limit the current to the deflector during a spark discharge from the charge stored in the capacitance of the cable and power supply. It replaced a resistor that was fitted into the output connection of the power supply and had mechanical and electrical deficiencies. The standoff insulators supporting the resistors and spherical terminals were housed in a stainless steel pressure vessel mounted on the cyclotron yoke (see Fig. 2). Its pressure rating was 150 psi. We operated at 30 psi with air supplied from the compressed air system of the building via a filter and regulator. The compressed air was routed inside the cable to the end of the high voltage feed through. It flowed out through another tube after cooling the end of the cable. This prevented the cable from overheating due to contact with the deflector cathode. The air flow rate was 20 STP cu. ft. per hour. This flow may not be needed when cathode cooling is implemented. The resistor strings, cables and high voltage feed throughs have been tested to 100 kV, the power supply limit.

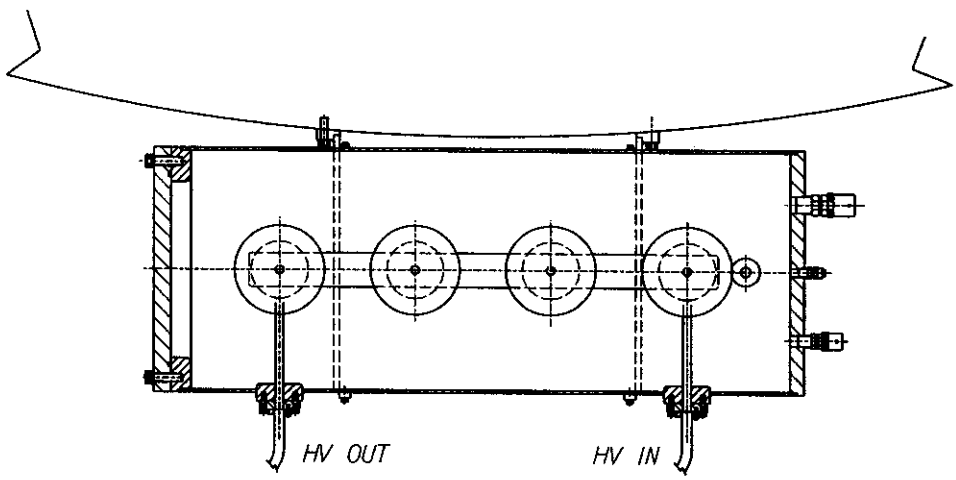

Fig. 2: Drawing of the air tank housing the resistor string (top view). The 3 resistors, not shown, are supported by 4 standoff insulators. The coaxial cables from the power supply and the deflector enter through O-ring sealed flanges on the side of the tank. The outside dimensions are 10.75" diameter and 28.5" long.

A LIQUID COOLED HIGH VOLTAGE FEEDTHROUGH FOR THE K1200 CYCLOTRON

D. J. Pudvay, T. L. Grimm, P. S. Miller, and D. R. Poe

Introduction

Superconducting cyclotrons offer a compact, high rigidity accelerating system with the concomitant difficulties of beam extraction. Extraction is achieved by the use of high field electrostatic deflectors with a thin septum. However, beam loss at the septum system, particularly for high power beams, produce thermal problems that necessitate cooling.

At present, the highest power beams extracted in the K1200 cyclotron at the National Superconducting Cyclotron Laboratory have been on the order of 400 watts with nearly as much power lost, presumably on the septum and deflector electrodes.[1] Further upgrades and the proposed coupled cyclotron project require beam power 10 times as great.[2] The increase in the energy and intensity of beams in the K1200 will require improved cooling and redesign of the entire electrostatic deflector assembly. This report presents the design and experimental results of a liquid cooled feedthrough assembly that will deliver the high voltage and cooling required to the deflector electrode.

Design

The feedthrough assembly is required to deliver 100 kV and the cooling fluid down a 5.1 cm inner diameter by 150 cm long vacuum tube to the high voltage electrode. Fig. 1 shows an overall schematic of the system. This system provides a "cold finger," that is the fluid is pumped to the back of the feedthrough and not into the electrode directly

Both the cooling fluid and the high voltage are passed to the electrode via the high voltage cable with the coolant return via a channel outside the cable and inside the ground tube. The high voltage cable consists of a center conductor wrapped by a semicon shielding encased in a polyethylene shielding. The semicon is a resistive conductor that acts to smooth any high field regions on the center conductor. The center conductor is removed and the semicon acts as the voltage carrier. This provides both a channel for the fluid and a series resistance to dissipate energy when the deflector arcs. The fluid voltage interface is achieved by a corona ball in the small fluid reservoir shown in Fig. 1. All edges inside the tank were rounded to reduce the field enhancements.

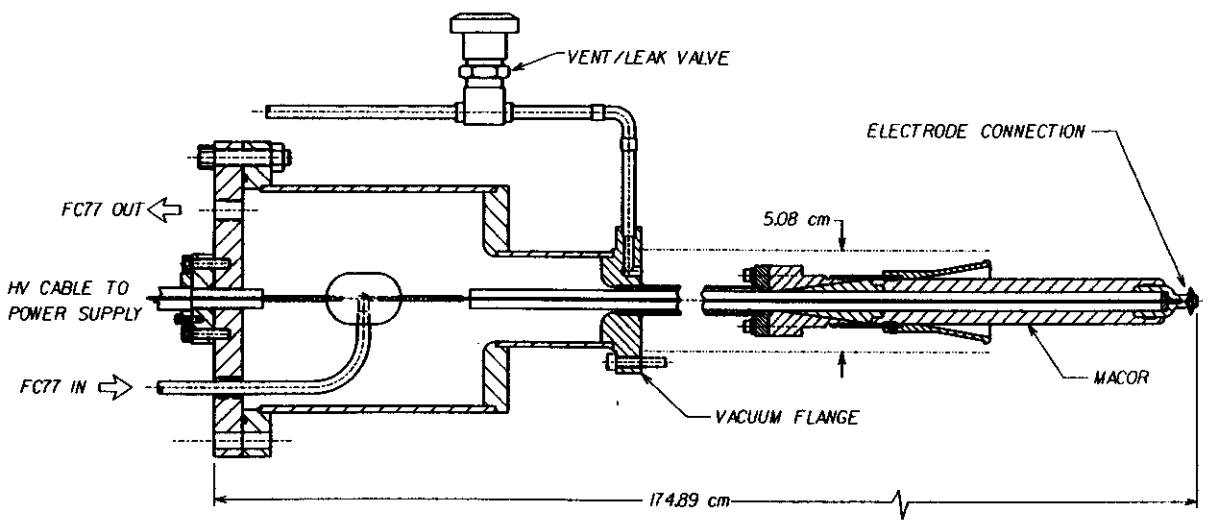

Fig. 1 Liquid Cooled Feedthrough Assembly

The cooling fluid requirements include high volume resistivity, high breakdown voltage, good thermal properties, and reasonably low viscosity. Three fluids were considered; low conductivity water, oil, and fluorinert FC-77, a fluorocarbon. Each had the necessary thermal and electrical properties as shown in Table 1.[3] Due to the difficulties in maintaining purity, the water was deemed not suitable and oil was rejected due to the difficulties in clean up if a vacuum breakage occurred. Therefore fluorinert was chosen.

	water	FC-77
density (g/ml)	1.00	1.78
viscosity (centistokes)	0.9	0.8
volume resistivity (ohm-cm)	NA	1.9×10^{15}
dielectric strength (kV/cm)	NA	160
specific heat (cal./g C)	1.00	0.25

Table 1. Comparison of the properties of water and flourinert

Experimental Results

The new feedthrough system was first tested for high voltage holding capabilities with a corona ball instead of the normal deflector electrodes. This was done because the electric field with the corona ball was lower than the deflectors thus requiring less high voltage conditioning time. In this first test it held 100 kV while drawing less than 10 mA current. The first test with the deflector electrode was successful in bringing the voltage up to 70 kV and drawing less than 10 mA current.

The highest power beam to date was an $^{18}O^{+6}$ beam at 80 MeV/A. The beam power extracted was 300 watts with an equal amount lost on the septum. A small submersible pump produces 5 ml/s flow to the electrode connection with about a 4 psi pressure drop. Most of the pressure drop occurs as the fluid flows inside the high voltage cable. At this flow rate the fluid can dissipate approximately 9 watts per °C rise in fluid temperature. The present electrode connection has a fairly high thermal resistance of about 15°C per watt due to the long narrow titanium cross section. Because the problems due to thermal expansion of the electrode limit the temperature rise in the electrode to about 150°C, the geometry of the electrode connection limits the cooling to about 10 watts.

The liquid cooled high voltage feedthrough is currently in use on the K1200 cyclotron. At present this should provide sufficient cooling but the increased beam power in the proposed coupled cyclotron project could require more. The cooling can be improved by redesigning the electrode connector or by circulating the liquid directly into the electrode. Changes to the connector include decreasing the temperature difference across the titanium and increasing the surface area for heat transfer from the electrode to the liquid.

References

1. P. Miller, T. Grimm, F. Marti, D. Poe, "Electrostatic Deflector Development", NSCL Annual Report (1995)
2. R.C. York, H. Blosser, T. Grimm, D. Lawton, F. Marti, J. Vincent, X. Wu, and A. Zeller, "Proposed Upgrade of the NSCL", Proc. of the 1995 Particle Accelerator Conference, (1995)
3. Fluorinert Properties Chart, 3M Industrial Products Division (1992)

K500 EXTRACTION SYSTEM STUDIES

David A. Johnson and Felix Marti

In the coupled cyclotron mode, the operating region of the K500 superconducting cyclotron is much reduced with respect to the K500 stand alone mode. Since the orbit shape in the extraction area varies significantly over the operating diagram, the extraction dynamics for the operating region necessary for the coupled mode was evaluated. The operating region for the coupled mode is characterized by central fields larger than 3.45 T and energies below 17 MeV/u.

Seven beams that enclose the new operating region were chosen to explore the beam dynamics issues. To make valid comparisons all magnetic fields were tailored in similar ways. The phase curve was selected to minimize the absolute value of the integral of $sin(\Phi)$ to reduce the energy spread. The extraction radius was selected to give a value of $\nu_r = 0.8$ for all beams. After the extraction bump (TC 13) was adjusted, an eigenellipse (with area of 0.004 in^2) was tracked from a point 80 turns before extraction and followed up to the entrance of the deflector. The starting times of the eight particles defining the ellipse boundary were adjusted so that they all had the same average phase to remove all deformations atributable to differences in energy gain. The internal beam prior to extraction showed no deleterious effects due to the crossing of the $\nu_r = 1$ and $\nu_r = 2\nu_z$ resonances.

A significant issue is the optimum shape of the electrostatic deflector. The present shape of the deflector was determined by matching the orbit of the 80 MeV/u Q/A=0.5 ion. The present deflector septum has a radius of curvature of 25.264 inches. As the proposed mode only needs to accelerate ions up to energies of approximately 17 MeV/u, the optimum septum shape was reevaluated. For the new reduced magnetic field range, the orbit curvatures can be more optimally shaped with a new septum that has a radius of 24.800 inches, giving better clearance than the old septum.

The extraction path includes two electrostatic deflectors and 9 passive focussing channels (M1 through M9) [1]. Of these, the M4 focusing bar was to be inserted for the high field magnetic beams, and removed from the orbit path in the low field cases. Operationally, the presence of M4 showed no significant difference in the beam quality, and as a consequence, M4 was not used at all. The M4 port has been dedicated to a new timing probe needed to tune the narrow beam phases. To improve the focusing in the extraction channel in the absence of M4 we increased the gradients of three bars (M3, M5 and M8) by minor design modifications. This new configuration provides better focussing properties.

References

1. Fabrici E., D. Johnson and F. G. Resmini, Nucl. Inst. and Methods 184, 301 (1981).

UPGRADE OF THE OPERATOR INTERFACE TO THE RADIATION SAFETY SYSTEM

R.M. Ronningen and P. Rossi

This past year we upgraded the system display computer and the operator interface (also known as a "man-machine interface," or MMI) to the radiation safety system. We previously used ScreenWare, by Computer Technology Corporation [1], for our MMI. We now use InTouch, by the WonderWare Corporation [2], to create and develop our new MMI. Also, the ladder logic program version was upgraded to SY/MATE Plus programming software, version 2.5, by GRAYSOFT, Inc. [3].

The upgrade was necessary because our version of ScreenWare could not be upgraded, its software required a monitor capable of displaying in an obsolete graphics format, the hardware was 10 years old, and the direction of the parent company's newer products diverged from our needs. Intouch's operating environment is Microsoft's Windows, and we are currently using version 3.11 running on a 486DX66 PC. Object-oriented graphics are used to create windows which contain objects that can be animated by logic conditions or by cursor selection. The windows interact with our Square D Company's SY/MAX Model 400 programmable logic controller[4], and other Windows applications, through a dynamic data exchange (DDE) server. The upgrade to Windows and DDE capability mirrors the cyclotron control system development direction.

We have to-date created several simple windows for monitoring the radiation safety system. Several simple "wizards" (pre-packaged programmable objects, such as buttons, lights, and meters) within InTouch were used, as well as several useful aftermarket ones from Reichard Controls [5], such as pop-up help dialog "balloons." We plan to create several complex windows using a wizard that can animate graphics in AutoCad's DXF format. This will reduce window development time by allowing us to use existing mechanical design drawings. A sound card was added to the PC, so that alarms can be announced by audio tones. We plan to add voice messages.

References

1. Computer Technology Corporation, 50 W. TechneCenter Drive, Milford, Ohio 45150; http://www.ctcusa.com/
2. Wonderware Corporation, 100 Technology Drive, Irvine, CA 92718; http://www.wonderware.com/
3. GRAYSOFT, Inc., 9275 North 49th Street, Brown Deer, WI 53223-1474
4. Square D Company, Executive Plaza, Palatine, IL 60067; http://www.modicon.com/directo.html
5. Reichard Controls, 1015 Valley Bluff Road, No. 3, Perrysburg, OH 43551; http://www.toledolink.com/reichard/

NON-INTERCEPTING CAPACITIVE BEAM DIAGNOSTIC

T.L. Grimm and P.S. Miller

The non-intercepting capacitive probe is a simple, robust beam diagnostic that measures the structure of the beam non-destructively. This makes it possible to monitor and feedback to the system while delivering the beam to an experiment. The basic operating principle of the capacitive probe is shown in Fig. 1. A metal cylinder is connected to ground by a coaxial cable terminated in 50 ohms. The charge induced on the cylinder produces a current in the cable that depends on the rate of change of the charge enclosed. The cylindrical capacitive probe can measure the beam intensity, phase relative to the rf, and bunch length.

The beam is emitted from the cyclotron in narrow pulses at the radio frequency. This beam can be represented by a Fourier series with components at harmonics of the rf frequency. The shorter the bunch, the higher the harmonics will be. To measure the bunch length efficiently, the probe cylinder must be shorter than the bunch. This will reduce the charge induced on the probe and thus decrease the available signal. If only the intensity and phase relative to the rf is needed, then the probe can be longer than the beam and pick up the entire charge of a bunch.

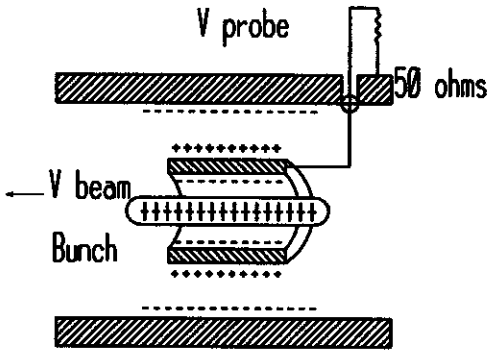

Fig. 1: Operating principle

The circuit used to monitor the beam is shown in Fig. 2. A matched coaxial line is used to maintain the intensity, phase and bunch length information. Because the beam currents are so small a high gain 60 dB broadband amplifier and spectrum analyzer are typically used. The capacitive probe and all cables are completely enclosed and well shielded. Even with the shielding, some radiated rf energy is detected, especially on the first harmonic. Fourier components of the beam can be measured on the second harmonic and above.

The bunch spacing and length of K500 and K1200 beams for coupled cyclotron operation are shown in Table 1. The 6° full width bunch length increases to as high as 35° for uncoupled operation.

	K500 2nd harmonic	K1200 1st harmonic
Bunch spacing (cm)	207	628
Bunch length for 6° rf (cm)	3.5	10.5
Bunch length for 35° rf (cm)	20.2	61.1

Table 1: Bunch spacing and length of extracted beams from the K500 and K1200 [1].

The K500 capacitive probe shown in Fig. 3 was installed in the Transfer Hall and was the first capacitive probe used at the NSCL. Its length allows bunch length measurements less than 6° as well as intensity and phase measurements. The isolated cylinder was made larger than the beam pipe to eliminate beam or secondary interception. Frequency domain analysis used a spectrum analyzer with a resolution bandwidth of 10 kHz. For a 10 nA beam the first 5 harmonics were above the noise floor with the strongest 5th harmonic signal of 60 μV being about 10 dB above the noise floor. At 100 nA the Fourier components were above the noise floor out to 550 MHz (37th harmonic).

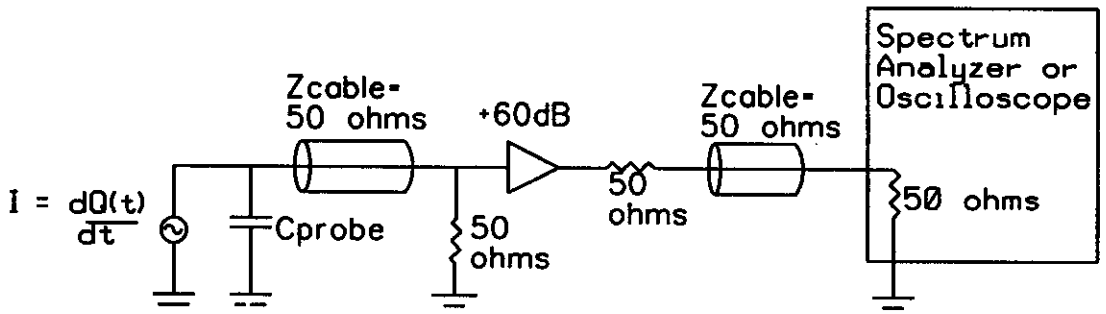

Fig. 2: Circuit schematic

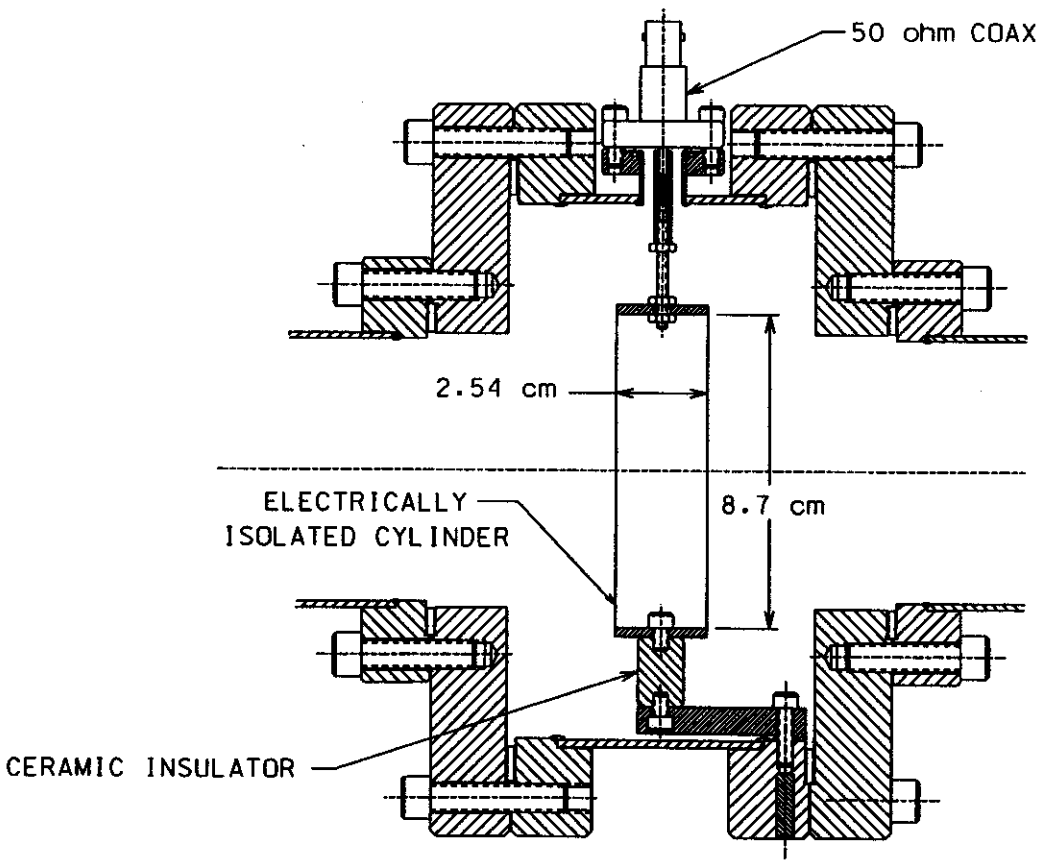

Fig. 3: Capacitive probe on K500 extraction line.

The K1200 capacitive probe shown in Fig. 4 was installed inside an existing beamline just before the first diagnostic chamber. It was built primarily as a non-intercepting intensity monitor, but could measure phase, and bunch length to the 8° level. With a large resolution bandwidth of 300 kHz and signal averaging a 100 nA beam had the first 5 harmonics above the noise floor with the strongest 2nd harmonic being about 10 dB above the noise floor. The capacitive probe has been used as an intensity monitor during operation by tracking the 3rd harmonic signal real time. The calibration obtained is 1.4 μV/nA, but it has varied by as much as a factor of two. A change in bunch length can explain this variation. The probe has shown the beam current oscillates, which is believed to be from the ECR ion source.

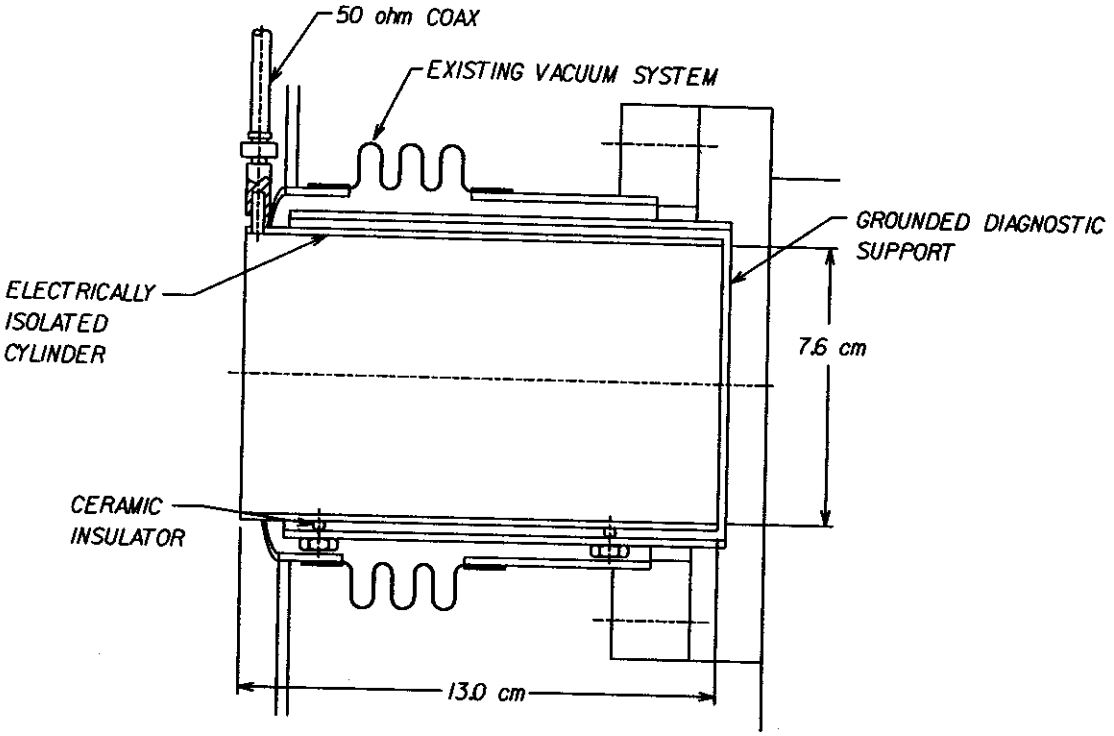

Fig. 4: Capacitive probe on K1200 extraction line.

The capacitive probe has been used to monitor the intensity of both cyclotron beams above the nA level. On the K1200 it has even become an operational tool. The measurement of the Fourier components on the spectrum analyzer for both probes shows the phase and bunch length information is available, but the required signal processing and data analysis to determine these parameters is the scope of future work. The M-channels could possibly be used as capacitive probes since they are already isolated to monitor current intercepted. Some of them are well shielded from rf and other pickup. By sectoring the capacitive probe the transverse beam parameters could be measured nondestructively.

References

1. R.C. York, H. Blosser, T. Grimm, D. Lawton, F. Marti, J. Vincent, X. Wu, and A. Zeller, "Proposed Upgrade of the NSCL", Proc. of the 1995 Particle Accelerator Conference, (1995)

BARNEY: NEW BEAMLINE CONTROL SOFTWARE FOR NUCLEAR EXPERIMENTS

M. Steiner, D.J. Morrissey

Experiments with the new S800 spectrograph will involve the control and monitoring of a large number of beamline devices, significantly increasing the overall complexity of nuclear–physics experiments. While the S800 hardware will be incorporated into the standard NSCL control system [1], a software user interface to the controls is needed that fulfills several requirements: The control system must provide the possibility to control and log the states of both FERMI and MODICON devices. Non-standard devices, such as magnet Hall and NMR probes, must also be supported. The software should allow the creation of simple interfaces for the less experienced experimenter as well as more sophisticated interfaces for the expert user.

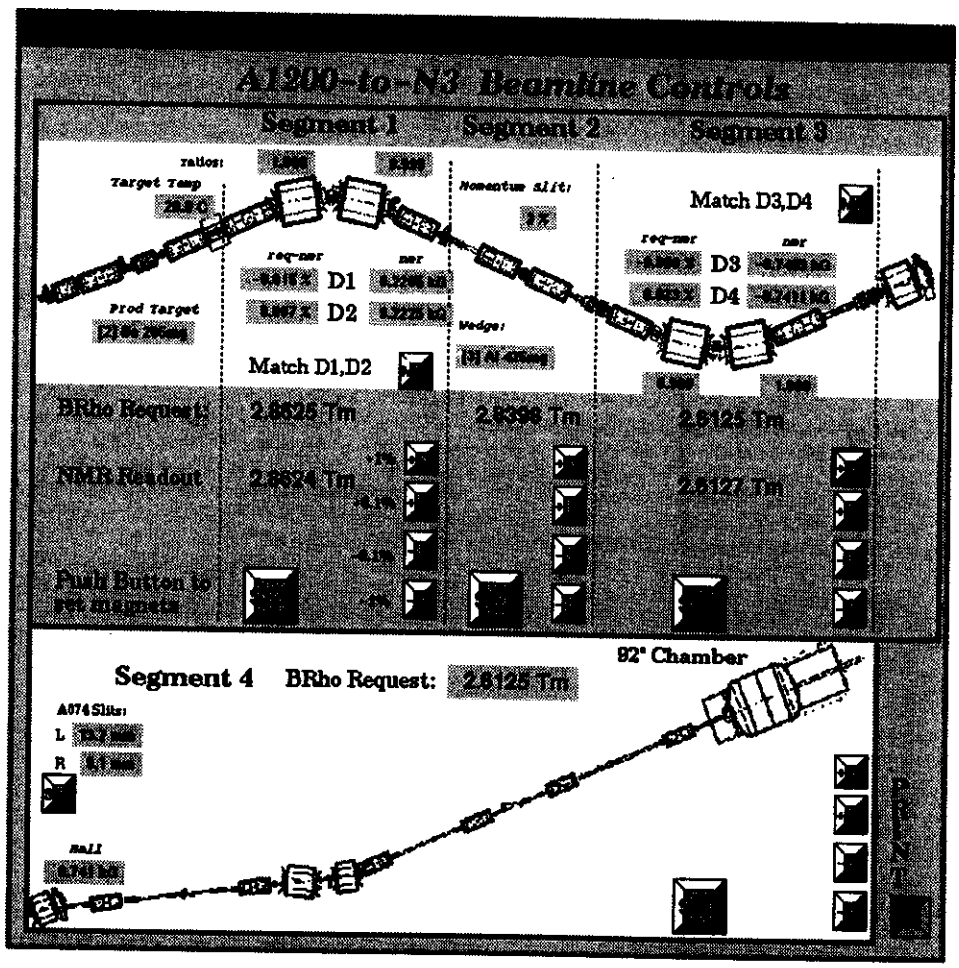

Figure 1: A sample "Barney" window for experiment control of the A1200 and N3 beamlines.

Completeness and reproducibility are also very important; it must be possible to save and reconstruct spectrograph settings in full — magnet settings, targets, slits, degraders, and all other devices.

In order to satisfy these requirements, the commercial VISTA control–system software package

was purchased and implemented at the NSCL under the work name of "Barney" [1].

While VISTA is capable of providing direct hardware control through VME, it has been implemented as an additional high–level layer in the NSCL control system rather than replacing existing structures.

Fig. 1 shows a relatively simple window created to control the beam lines for a nuclear–physics experiment in the 92–inch chamber. Input is limited to setting the magnetic rigidities of the four beamline segments and positioning the A1200 exit slits. Graphics are incorporated to help orient the user. Changes in magnet and slit settings are easily accomplished using push buttons, and the magnetic fields of the A1200 dipoles are monitored by NMR probes. Deviations from the desired values can be corrected through a push of the "match" button. Note that a number of MODICON devices, such as production target and momentum slits, are also monitored. Additional windows to control these devices can be "popped up" as needed.

Implementation of the new system started in November of 1995. It has been tested successfully in several nuclear–physics experiments and development continues. By the time the S800 spectrograph begins its commissioning phase, features such as automatic logging of settings and inclusion of parameters in the experiment data stream are expected to be in place.

References

1. J. Vincent, L. Foth, A. McGilvra, J. Priller, *The NSCL Control System*, Proceedings of the 1995 IEEE Conference on Real-Time Computer Applications in Nuclear Particle and Plasma Physics, East Lansing, Michigan, May 1995, pp. 297-302.

[1] in honor of Mr. Gumble, *not* a purple dinosaur

STATUS OF THE ANALYSIS HALL AIR-ACTIVATION MONITORING SYSTEM

N.E. Davis, P. Rossi, R.M. Ronningen, and D. Swan

The neutron flux generated by accelerator operations activates air [1,2], in addition to other materials. We are beginning tests of an air-activation monitoring system, recently installed in the NSCL Analysis Hall. The purpose of this system is to determine current levels of air activation (production of ^{11}C, ^{13}N, ^{15}O, which are positron emitters, and of ^{41}Ar) occurring within the Analysis Hall, to compare these levels with derived air concentrations, and to obtain data which will enable us to estimate levels during proposed coupled cyclotron operations.

Four lines to carry air were installed, running from the Analysis Hall to a roof area, where analysis was performed. Each air line was polyvinylchloride tubing, having an inside diameter of one inch. Paper element particle filters (nominally 10 μm particle size, 99% efficiency) from Solberg Manufacturing, part number 5Z665, were attached to the line ends in the Analysis Hall. The end of the first line is located near the A1200 target chamber shielding. The end of the second line is near the first dipole-pair area. The end of the third line is located near the second image point of the A1200, and the end of the fourth line is near the east end of the Analysis Hall.

A Thomas Industries pump, model number 727CM39, is used to pull air from the four lines through Dwyer standard window flow meters. The air is mixed in a manifold, and passes through an in-line particulate paper filter having a 2-inch-diameter, from HI-Q Environmental Products, model #ILHP-47. The air then flows through an Equimeter MR-75 temperature-compensated, diaphragm-type totalizing meter, to obtain the total volume of air. From the air-totalizing meter, the air passes through the sample chamber, a 1L Marinelli beaker identical to one used for the calibrations described below.

Using helium gas and a helium leak detector, the transport time of each air line was adjusted, using the flow valves, to be 20 seconds. The total volume of air flow was determined by the totalizing meter, and checked by timing measurements using the flow rate values. Two different mixtures of room air were studied. The first was an equal mixing of all four lines. The second isolated the target chamber line. For the equal mixing case, the air flow rate was determined to be 51.7 L/min. For the isolated target chamber case, the flow rate was determined to be 34.4 L/min.

High resolution gamma ray spectroscopy was used to identify radionuclides, using a high-purity germanium detector. The detector was calibrated using multi-nuclide-source material, in a simulated-gas-standard, from Isotope Product Laboratories, model number SGS-ML-1L. The gamma-rays used for energy calibration and efficiency calibration were 122.0 keV from ^{57}Co, 159.0 keV from ^{123m}Te, 320.0 keV from ^{51}Cr, 392.0 keV from ^{113}Sn, 662.0 keV from ^{137}Cs, 898.0 keV from ^{88}Y, 1173.0 keV from ^{60}Co, 1275.0 keV from ^{22}Na, and 1836.0 keV from ^{88}Y. The source material is in a dispersed foam matrix of 1L volume, contained in a model number 127G Marinelli beaker. All sample data were collected using an empty, but otherwise identical, Marinelli beaker in the same geometry. The Marinelli beaker was housed within a 2" lead brick shield, and was positioned in direct contact with the end of the germanium detector. This was because the cryostat of the germanium detector was too large to fit inside the re-entrant port of the beaker. When operational for routine monitoring, we plan to use a NaI detector which will fit in the port.

Two types of air sample analysis were attempted. The first was a continuous sample, with air being pumped from the Analysis Hall through the sample chamber at a continuous rate. The second was a grab sample, where data collection was initiated when the flow valves to the sample chamber were closed. Our first measurements were done during continuous operations with a beam of 155 MeV/n $^{4}He^{2+}$. The continuous sample data were not of high quality, but indicate that the concentrations of ^{11}C,

^{13}N, ^{15}O, and ^{41}Ar are below the as-low-as-reasonably-achievable values of 10% of their respective DACs. The observed activity in the grab samples was not high enough to identify the relative percentage of these nuclei by half lives. Improvements in the system are being made. Further measurements will take place in the spring of 1996.

References

1. Rindi, A. & Charalambus, S., Airborne Radioactivity Produced at High-Energy Accelerators, Nuclear Instruments and Methods, 47, (1967), 227-232.
2. Butala, S.W., Baker, S.I., Yurista, P.M. Measurement of Radioactive Gaseous Releases to Air from Target Halls at a High Energy Proton Accelerator. FERMILAB-Pub-88/189.
3. United States Nuclear Regulatory Commission, Rules and Regulations, Title 10, Chapter 1, Code of Federal Regulations-Energy. "Derived air concentration" (DAC) means the concentration of a given radionuclide in air, which, if breathed by the reference man for a working year of 2,000 hours under conditions of light work (inhalation ratio 1.2 cubic meters of air per hour), results in an intake of one ALI. These limits are 2.00E-04(μC_i)/(mL) for ^{11}C ($t_{1/2}$=20.38 min) compounds (the most restrictive value) and 3.00E-06(μC_i)/(mL) for ^{41}Ar ($t_{1/2}$=1.83 h). For ^{15}O and ^{13}N, the DAC is for an otherwise unspecified isotope with $t_{1/2} < 2$ hrs. For ^{15}O ($t_{1/2}$=2.04 min) and ^{13}N ($t_{1/2}$=9.97 min) the DAC is, 1.00E-07(μC_i)/(mL). "Annual Limit on Intake" (ALI) means the derived limit for the amount of radioactive material taken into the body of an adult worker by inhalation or ingestion in a year. ALI is the smaller value of intake of a given radionuclide in a year by the reference man that would result in a committed effective dose equivalent of 5 rems (0.05 Sv) or a committed dose equivalent of 50 rems (0.5 Sv) to any individual organ or tissue.

BONNER SPHERE MEASUREMENTS OF NEUTRONS FROM BEAMS OF ^{4}He, ^{12}C, AND ^{16}O AT 155 MEV/U STOPPED IN A HEVIMET TARGET

R.M. Ronningen, P. Rossi, L. Heilbronn[a], and G.I. Britvich[b]

The proposed coupling of the K500 and K1200 cyclotrons will provide beam intensities up to one particle microampere for lighter ions, with beam energies to 200 MeV per nucleon. Beams with these characteristics produce copious amounts of penetrating radiation, the most important being neutrons.

Few data are available for heavy ion beams, having this energy, irradiating thick targets. Thus, reliable neutron production source terms for these beams are not readily available for shielding calculations. Therefore, we measured neutrons produced from beams of ^{4}He, ^{12}C, and ^{16}O ions at 155 MeV/u stopping in a thick target.

Our thick-target experiment was set up in the N4 vault. The target was a solid cylinder of Hevimet [1], an alloy of tungsten, nickel, and copper. This material is used for many of the beam stops and Faraday cups at the NSCL. The target diameter was 5.08 cm and the length was 5.093 cm. For reference, the ranges of the He, C, and O ions in Hevimet are about 1.72 cm, 0.61 cm, and 0.46 cm, respectively. The target was pressed into a long copper pipe. Insulating rings were placed around this pipe, and the assembly was placed in the beam line, forming a Faraday cup for current integration.

The ^{4}He, ^{12}C, and ^{16}O ions were simultaneously produced in the NSCL's room temperature ECR ion source, from a mixture of He and CO_2 gases. The desired ion beam (the beams were charge-to-mass analogs) was selected by changing only the K1200 cyclotron frequency.

A Bonner-sphere spectrometer, having polyethylene spheres with diameters of 2, 3, 5, 8, 10, and 12 inches, was used for the neutron measurements. This spectrometer was purchased last year from Ludlum Measurement, Inc. [2]. The detector-photomultiplier housing was constructed of low-carbon steel, for additional magnetic shielding, and can house a 10 mm diameter detector. The spectrometer was placed one meter from the target. Measurements were made, using each ion beam, at angles of 0, 30, 60, 90, and 120 degrees with respect to the beam direction. In addition to using the moderating spheres, measurements were made with the "bare" detector, i.e., without using a sphere, and also with the bare detector covered with cadmium foil. The detector was a cylinder (4 mm diameter, 4 mm length) crystal of LiI(Eu), enriched in ^{6}Li, mounted to a photomultiplier tube. A plastic scintillator, placed at approximately 2 meters from the target, and about 20 degrees from the beam direction, was used to monitor the beam position on the target.

Several additional measurements were made to assess the target thickness effect on the neutron yields. With the spectrometer at 90 degrees, measurements using the beam were made first with the target alone, then with additional Hevimet. Measurements were also made using a PuBe source (about 4.5 MeV average neutron energy), first, with the target removed, and then with the source behind the target. Both sets of measurements, using the data for the three largest spheres, gave an estimation of the average interaction length of about 1.27 cm. This only gives a rough estimate of the interaction length, because the interaction length is neutron-energy-dependent, and each sphere has its own energy response.

Room scattering was also measured. Using the beam, we placed a "shadow bar," consisting of a solid cylinder of iron, having a diameter of 10.16 cm and a length of 30.48 cm, between the target and the spectrometer at 90 degrees. The shadow bar data contain contributions from room and target scattering scattering into the detector. We also did an additional measurement, but using the PuBe source to give us a known neutron energy spectrum, with the spectrometer at zero degrees. Here, measurements were done with and without the target, and with the target and a shadow bar. The shadow bar, in this case,

was an 27.94 cm-long, truncated cone of brass, tapered from 17.15 cm in diameter to 10.80 cm. The latter set of measurements will be compared with a measurement, using the PuBe source, made in a relatively open area of the NSCL, which simulated a scatter-free situation.

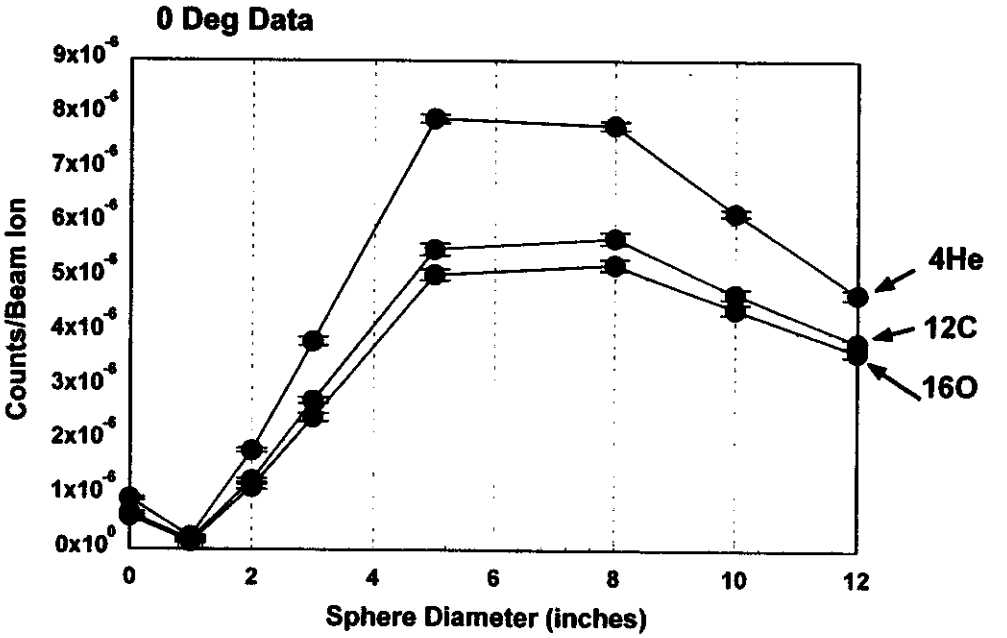

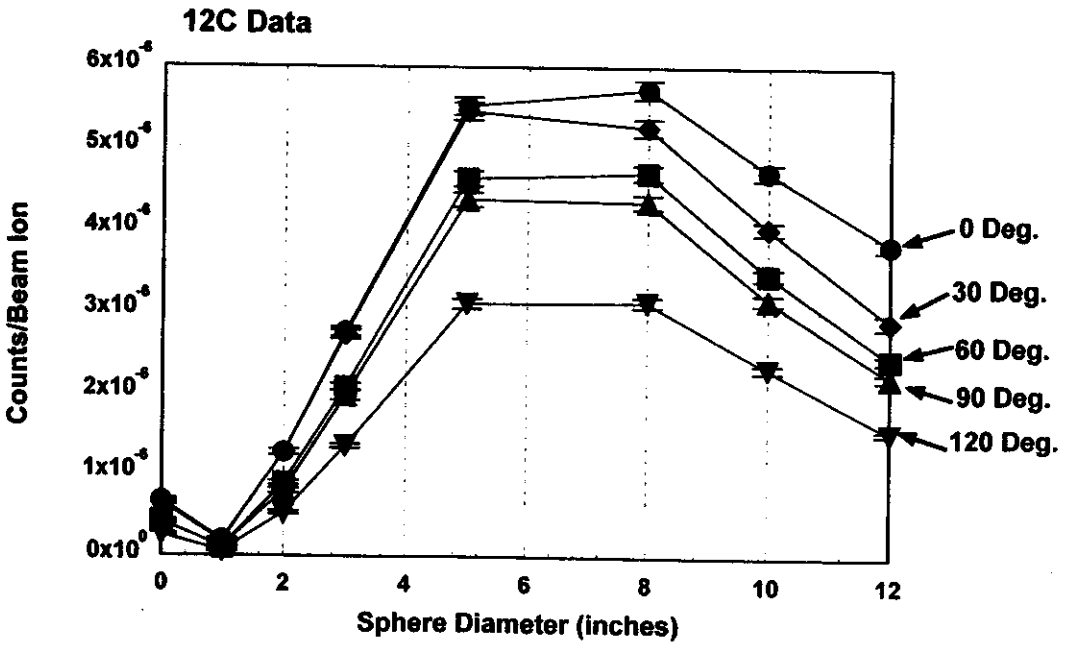

Figure 1 shows measured counts per beam ion for each sphere, when the spectrometer was at 0 degrees, for beams of ^{4}He, ^{12}C, and ^{16}O ions stopping in the target of Hevimet. Figure 2 shows the counts per beam ion as a function of angle for the ^{12}C ion beam. In each figure, the data for the "bare" detector are plotted at the abscissa value of 0-inch, and the data for the Cd-covered, bare detector are

plotted at the abscissa value of 1-inch. Qualitatively, there appears to be fewer neutrons per beam ion for heavier ions at a given energy per nucleon. This may be related to the ion range. And, as expected from many other studies, the number of neutrons per beam ion decreases for increasing detection angle. Quantitatively, these data are preliminary in that a more refined estimate of the target thickness contribution will be made, and the room scattering must be considered. The corrected data will then be analyzed using the unfolding codes BUNKIUT [3] and PREF [4], to obtain the neutron energy spectra and yields of neutrons per beam ion.

a. Lawrence Berkeley Laboratory, Berkeley, CA
b. Superconducting Supercollider Laboratory and IHEP, Protvino, Russia.

References

1. HD18, by Mi-Tech Metals, Inc., 1340 N. Senate Ave., Indianapolis, IN 46202; HD18 is 95% tungsten, 3.5% Ni, and 1.5% copper, and has a density of 18 g/cm^3.
2. Ludlum Measurement, Inc., P.O. Box 810, 501 Oak Street, Sweetwater, TX 79556.
3. K.A. Lowry and T.L. Johnson, Naval Research Laboratory (July, 1983); modified by S. Peterson, University of Texas, Austin (March, 1986).
4. E.A. Belogorlov and V.P. Zhigunov, Nucl. Instr. Meth. Phys. Res., **A235**, 146(1985).

S800 PROGRESS REPORT

A.Zeller, S.Alfredson, D.Bazin, S.Bricker, J.Caggiano, J.DeKamp, R.Fontus, D.Harris, H.Hilbert, P.Johnson, H.Laumer, L.Morris, D.Pendell, D.Sanderson, B.Sherrill, R.Swanson, J.Wagner, B.Zhang and R.Zink

Significant progress in the completion of the S800 has been accomplished in 1995. The most important of the milestones were the completion of D2 and its installation on the carriage, the initial mapping of D1, the testing of Q1 and Q2, and the completion of all the beamline quadrupole triplets.

During the leak checking of D2's bobbin a leak was discovered in one of the welds done by the vendor. This weld connects the coil volume with the vacuum space between the coils and thus a leak allows helium to diffuse into the insulation vacuum space. The leak was judged to be un-repairable without significant risk to the coil, so a solution of sealing up the space between the coils was made. Both inner and outer coil spacers were welded shut and a small line brought out of the cryostat and connected to a vacuum pump. We believe the helium leak in D1 is in the same location, but is, unfortunately, not repairable without complete disassembly of the magnet. Since the CTI-1400 can keep up with the load, on a limited basis, the leak will not be fixed. The addition of the new refrigerator system for the Coupled Cyclotrons upgrade will provide significantly more refrigeration capacity than is needed for the S800. Preliminary magnetic field maps were taken (See the separate report). Final maps have to done with D1/D2 in place and in operation.

The cryostat for D2 was completed and the magnet was assembled in place on the carriage. Attachment of the cryogenic connections started immediately afterwards. The cryogenic connections are very time consuming since every joint has to be leak checked, then covered with superinsulation and the outer cryostat closed. Connections have to be made between the cryo-distribution box above the CTI-1400 to the flexible lines which allow the carriage to rotate, then to D1, then D1 to D2, then to the box which will connect Q1/Q2. Additionally, another box was installed along the North wall for future applications, such as cryogenic targets or deflection magnets. The cryogenic connections will be completed early in 1996. Figure 1 shows both dipoles in place on the carriage, as well as some of the cryogenic connections.

The complete magnet assemblies for Q1 and Q2 were tested in the dunking dewar. Both magnets tested to their design currents. The magnets are being assembled into the cryostat. Upon completion they will be attached to the refrigerator and mapped before being put on the carriage. The sextupole which is in Q2 was not tested because it runs at such low field that testing was deemed not necessary.

The first beamline quadrupole triplet was installed and mapped(See the separate report). The first two dipoles and the second and third triplets were installed on the beamline. The last two triplets are complete, but can not be installed until the last two dipoles are in place. This will be done in early 1996.

The roof shielding has been ordered, but will not be delivered until the new shielding walls have been constructed. Work has started on the South wall. Installation of the utilities, ie., electricity, city water and low conductivity water has begun. Because everything on the carriage must rotate with the spectrometer, all utilities have to come through a flexible umbilical at the center of rotation. The spectrometer has been rotated to verify that it moves smoothly on the track without putting undue stress on the central pivot.

More details on most of the systems are given elsewhere in this Annual Report.

First beam down the beamline is scheduled for the Spring of 1996. Beam to the focal plane will happen shortly afterward. Several projects have been postponed in the interest of getting the S800 on line for doing experiments as soon as possible. Most notable of these is the large, general purpose

scattering chamber. This will not be available until 1997. The temporary chamber will, however, accomplish nearly everything the general purpose one will, only not as conveniently.

Figure 1: The S800, showing both dipoles in place on the carriage.

S800 BEAMLINE MAGNETS AND SPECTROGRAPH QUADS PROGRESS REPORT

J. Wagner, J. DeKamp, A. Zeller, S. Alfredson, R. Swanson, R. Zink, B. Zhang

In April, 1995 the first superconducting quadrupole [1,2] triplet for the beamline to the S800 spectrograph was completed and installed as shown in Figure 1. By May 1995 the triplet had been cooled-down, tested (all three magnets tested above operating current), and mapped. Construction of the second and third superconducting quadrupole triplets was finished in August 1995. These two triplets were installed and aligned in their 45 degree positions by September 1995. The fourth and fifth superconducting quadrupole triplets were completed in December 1995. Assembly of two S800 beamline dipoles were completed with the first dipole in the S800 beamline being successfully cooled-down, tested and mapped. Construction of the S800 spectrograph Q1/Q2 doublet is now 80% complete.

Figure 1: First completed S800 quadrupole triplet in position in the beamline.

S800 Beamline Quadrupoles

A LHe bucket was fabricated (Figure 2) for testing three quadrupole magnets at one time in the large dunking dewar. All three magnets in the second superconducting quadrupole triplet were successfully tested in the dewar. Because the end magnets operate at approximately half the current of the middle magnets only the middle magnets of the third, fourth and fifth quadrupole triplets were tested in the dunking dewar. A hinge stand (Figure 3) was fabricated during the assembly of the second quadrupole triplet making the procedure of rotating the magnet assembly from a horizontal to a vertical position safer and easier. Thicker G-10 support links were fabricated for the links that support the magnet weight to account for design changes of making them at a 30 degree angle (Figure 4) and results from strength testing of links already machined. The first triplet was cooled down and all three magnets were successfully operated. The magnets were also

aligned to the beam axis. The static boil off rate was 0.75 liters per hour of LHe at 1 atm which agrees with calculations when taking shield temperatures into account. The LN2 shield was warmer than anticipated. The ideal heat load assuming 80 kelvin shield temperature is 0.45 liters per hour at 1 atm.

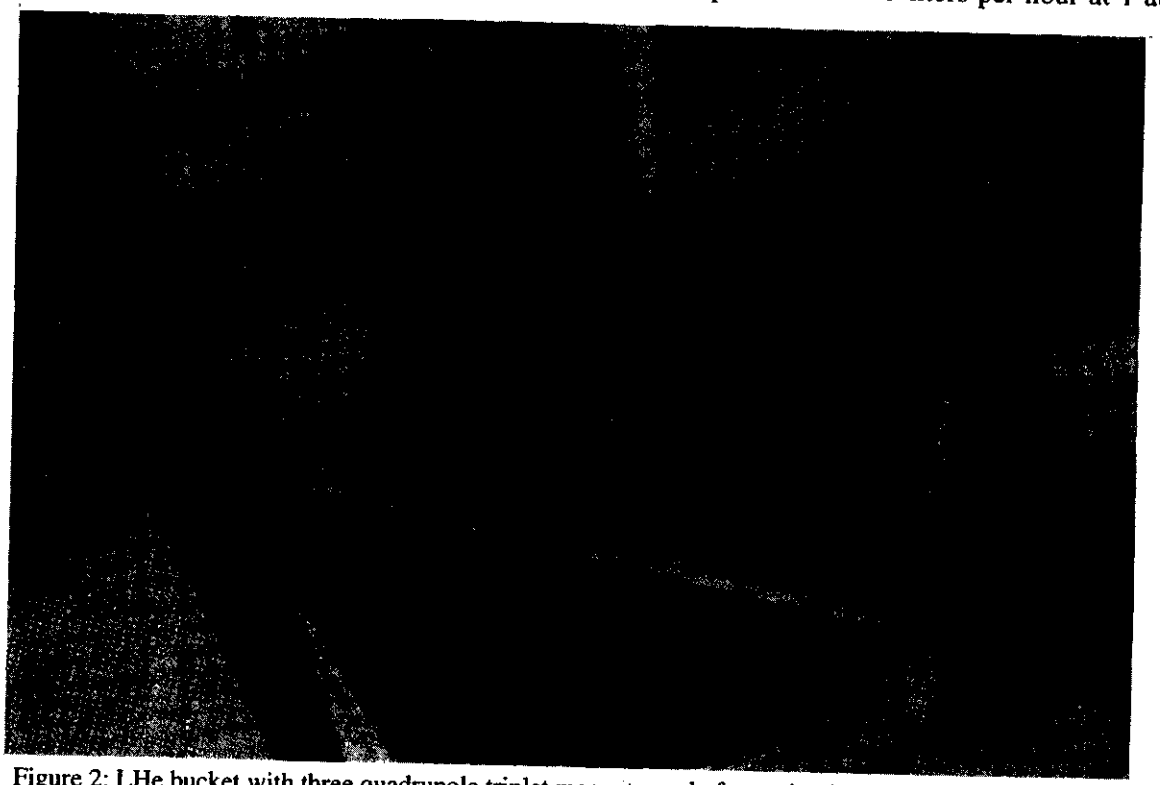

Figure 2: LHe bucket with three quadrupole triplet magnets ready for testing in the large dunking dewar.

Figure 3: Hinge stand attached to quad triplet with LHe vessel completed and LN2 shield partially assembled.

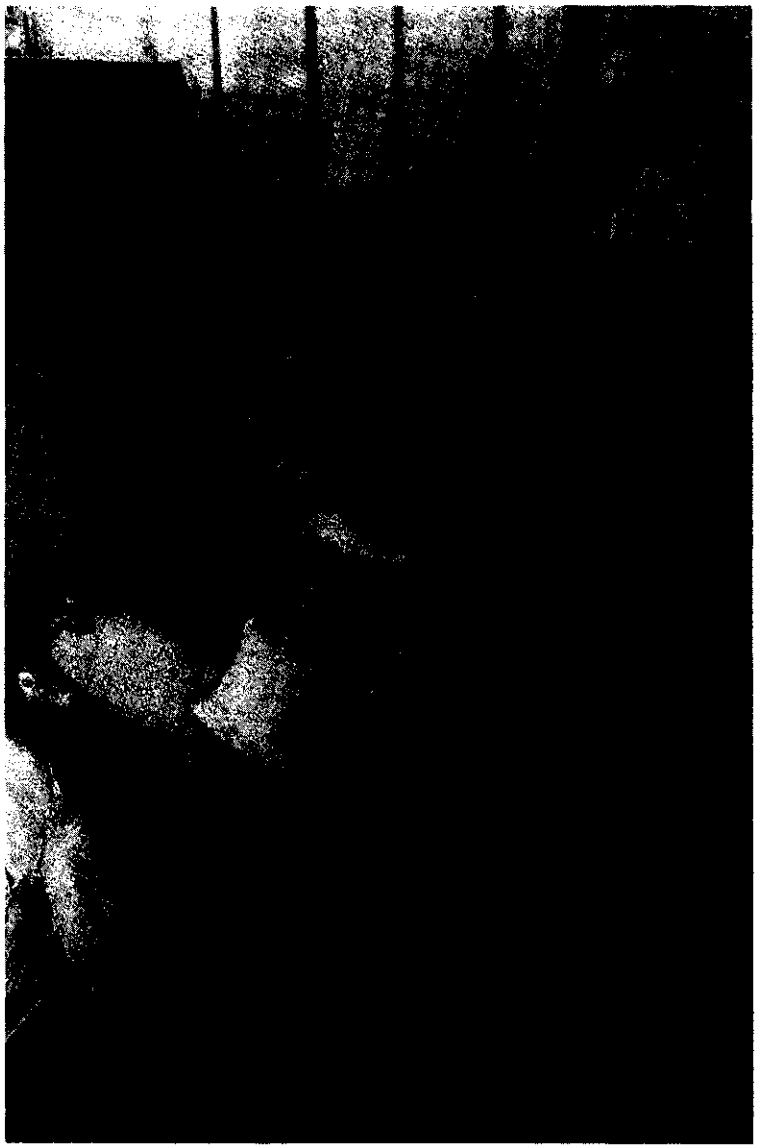

Figure 4: Rear vertical link assembly with the cryostat partially assembled.

The first superconducting quadrupole triplet was finished in April taking a total of eight months to complete (including delays due to late shipment of shield parts). The second triplet was completed in 3 months. To meet our goal of completing all five triplets by the end of 1995 a second assembly fixture was made to allow assembly on two triplets at a time. As soon as a magnet assembly was moved from the 4 ft. by 6 ft. surface plate [1] to the hinge stand for assembly of the LHe container the next magnet assembly could begin to be assembled on the surface plate. Once the LN2 shield had been assembled around the LHe container it was moved off the hinge stand for cryostat assembly and the next magnet assembly was moved to the hinge stand. This procedure saved two to three weeks per triplet in assembly time on the third, fourth and fifth triplets. Therefore, we were able to build the last three triplets in five months.

S800 Beamline Dipoles

The first two S800 beamline dipoles are ready for installation (Figure 5) and should be in place sometime in January 1996. The last two beamline dipoles are in various stages of construction. The third beamline dipole bobbin has been welded into its cryostat and is ready to be welded to its poletip assembly. The fourth beamline dipole bobbin has been superinsulated and is being assembled into its cryostat. Both beamline dipoles will be completed by February 1996.

S800 Spectrograph Q1/Q2 Quadrupole Doublet

Quadrupole and sextupole coils were wound and the quadrupole coils have been assembled into their steel assemblies. The two assemblies were then attached and aligned by a precision spacer ring as shown in Figure 6. The doublet was tested to full operating current in the large dunking dewar. The Q2 sextupole coils were assembled on the bore tube (Figure 7). Because part of the construction process was similar to that of the quadrupole triplets, a hinge stand comparable in design to the triplet hinge stand was fabricated to allow assembly and alignment of the bore tube (and sextupole) within the magnet assembly. The LHe vessel was assembled around the magnet assembly while still attached to the hinge stand. It was then removed from the hinge stand to assemble the LN2 shield. The shield has been

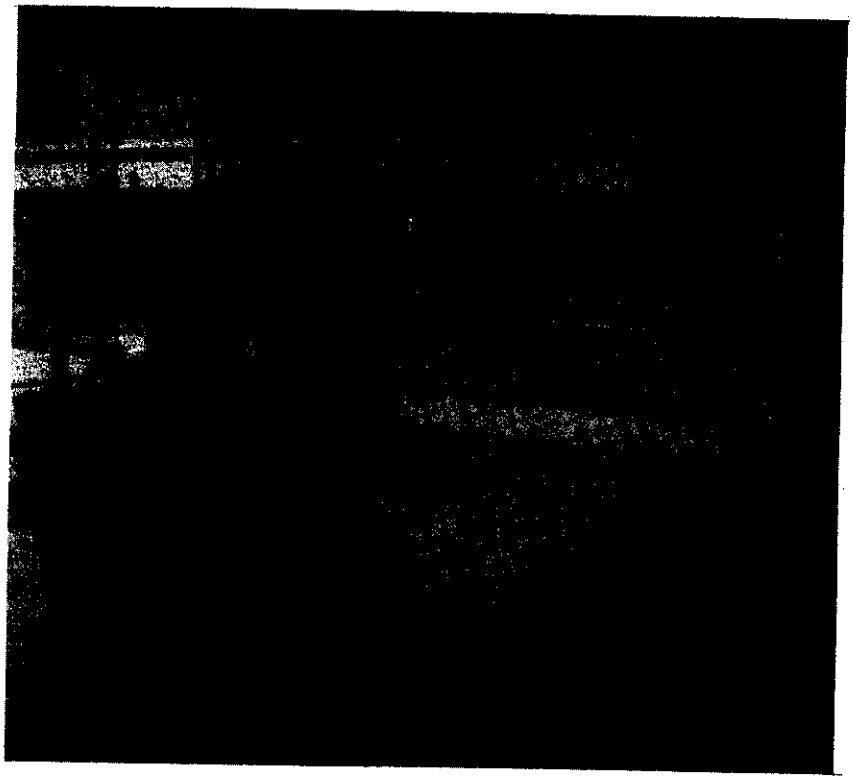

insulated and is ready for installation into its cryostat. All cryostat parts have been fabricated and are ready for final assembly. Construction and mapping should be completed by March 1996.

Figure 5: Completed S800 beamline dipole with lifting fixture attached to 40 ton crane.

References

1. J. DeKamp at al. "S800 Beamline Magnets and Spectrograph Quads Progress," NSCL Annual Report (1994), p. 163.
2. A. F. Zeller et al., "Superconducting Beamline Elements for the NSCL Spectrograph," IEEE Trans. on Applied Superconductivity, (in press).

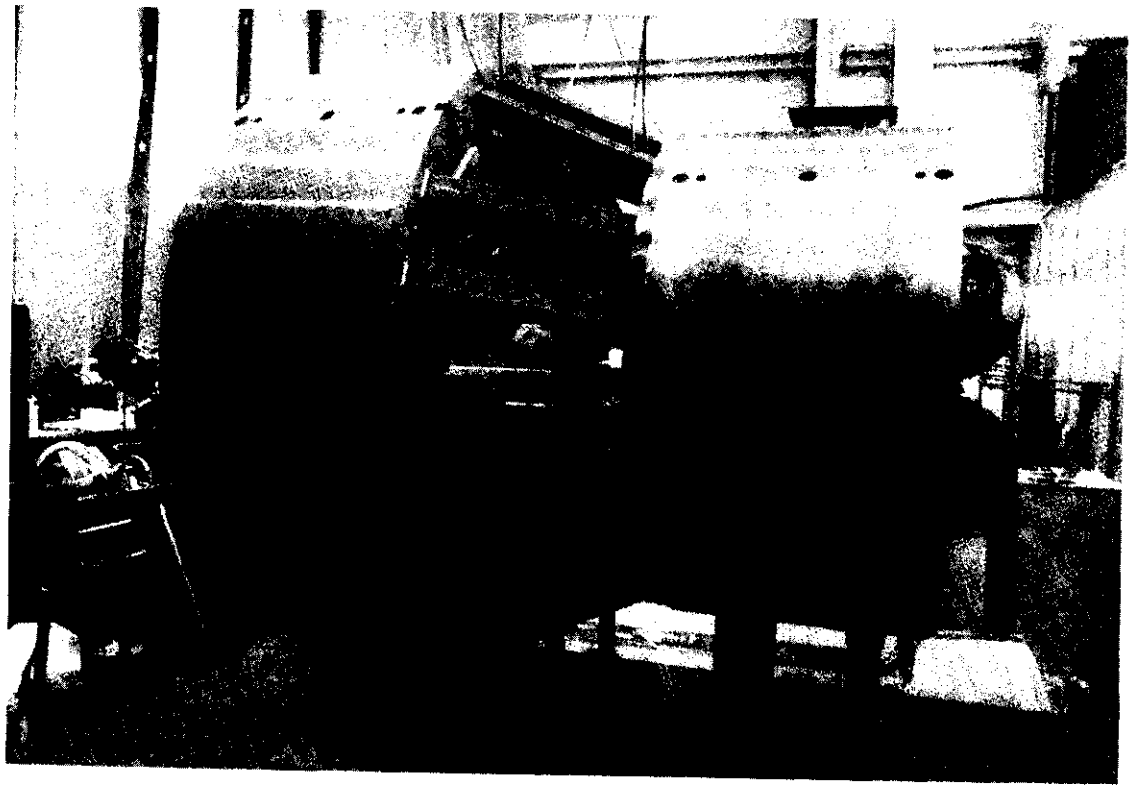

Figure 6: S800 Q1/Q2 quadrupole doublet magnet assembly with rotating fixture on surface plate.

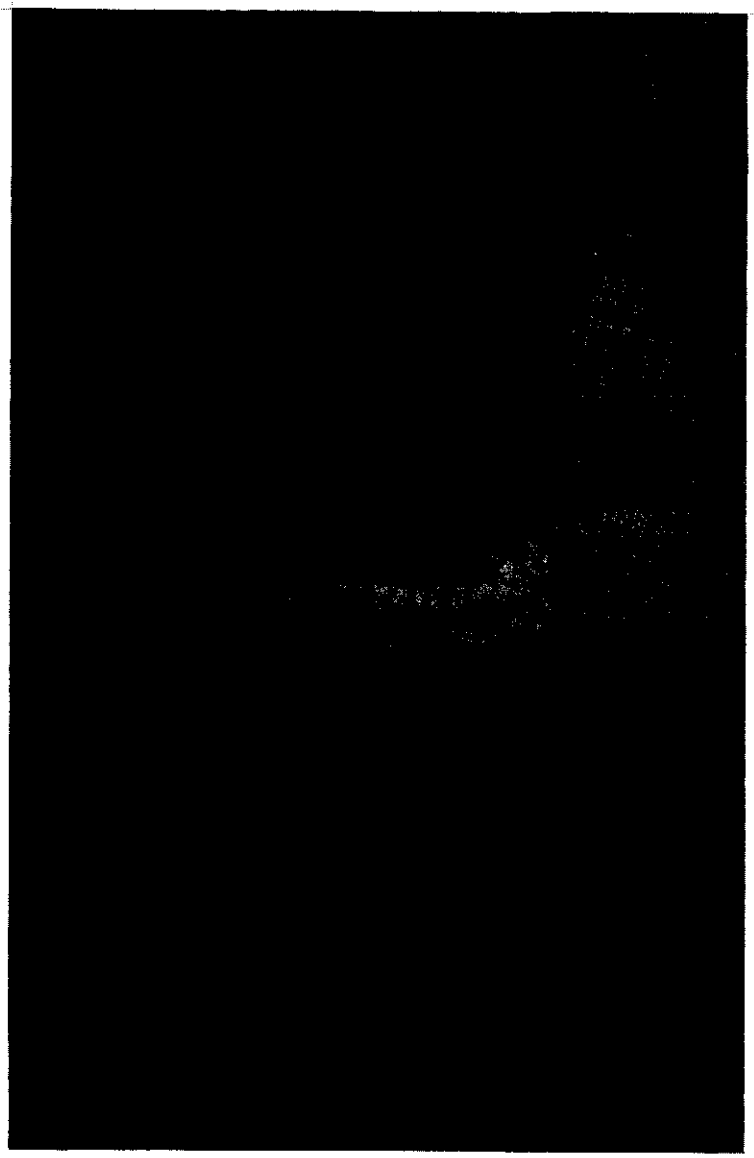

Figure 7: Q2 sextupole coils assembled on the bore tube.

S800 BEAMLINE QUADRUPOLE TRIPLET MAPPING

B. Zhang, P. Johnson, B. Sherrill, A. Zeller, R. Zink

An integral part of the S800 spectrometer is the analysis line which consists of fifteen superconducting quadrupoles and four superconducting dipoles. The beamline brings the beam from grade level into the spectrometer, which is situated in a ten meter deep pit. The quadrupoles are large version of the NSCL's standard beamline quadrupoles.[1] The standard quadrupoles have a 12.7 cm diameter inscribed circle and S800 beamline quadrupoles are 20.3 cm in diameter. The beamline quadrupoles are arranged into triplets with 3 magnets in a common cryostat. To achieve the required energy and angular resolution for nuclear physics experiments, the magnetic fields must be accurately known.

Quadrupole Mapper

The mapper used for magnetic field measurement is based on a 486 PC computer, with an Animatics 5000 Stepper Motor Controller and F.W. Bell 9903 series 3 axis gaussmeter. The control program was written using Borland Turbo Pascal compiler version 7.0.[2]

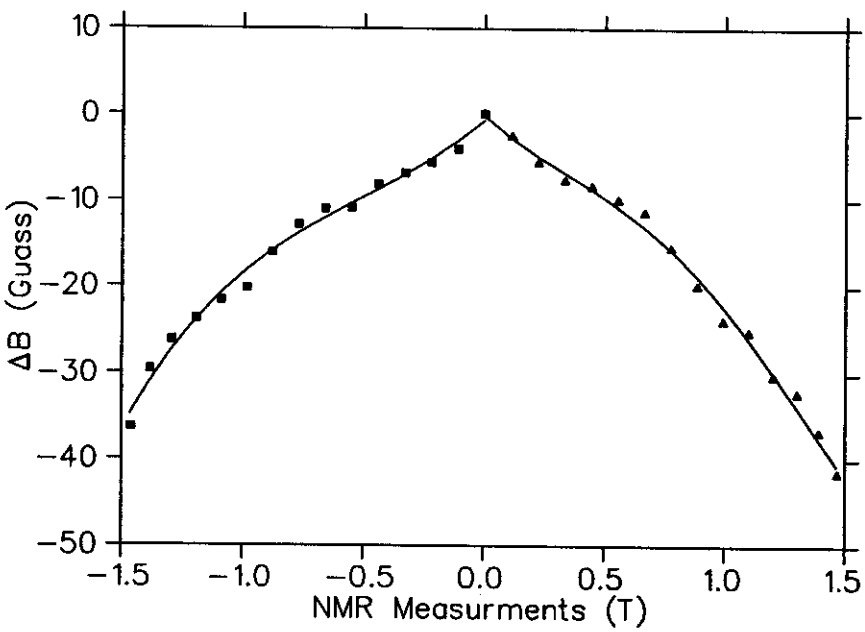

Figure 1: The magnetic field difference between the gaussmeter and NMR measurements for one channel. The solid lines through the data are fourth order polynomial fits.

Two different types of superconducting magnets were mapped with this apparatus: the S800 beamline quadrupole triplets and the S800 spectrometer doublet. A complete map requires motion in three dimensions. Azimuthal (Φ) movement of the probe is achieved through the use a NEMA 34 servo motor and encoder. The increments are applied through an 80 tooth gear and worm drive, with a resolution of 0.09 degrees. Along the beamline axis (Z), movement of probe is achieved through a non-magnetic

Thompson slide rail assembly equipped with a NEMA 23 servo motor and encoder. This allows for Z direction movement of the probe at programmable speeds up to 1 cm per second. The radial positioning of the probe is done with non-magnetic threaded rod inside the probe holder box. The center of rotation is captured and held in position by means of an aluminum machined frame which is flat to plus or minus 0.0127 cm over entire 76.2 cm length.

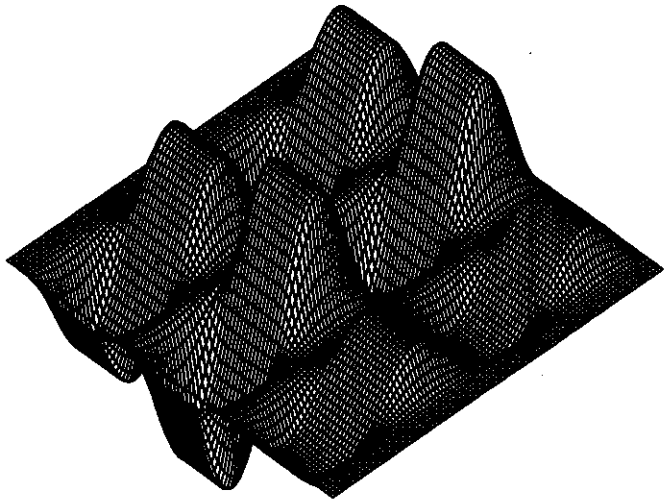

Figure 2: The radial component of the magnetic field for the triplet when the currents for the three quadrupoles are 5, 15 and 10 A respectively.

The gaussmeter utilizes the Hall effect to measure magnetic field. The maximum field produced by any of the magnets is 2 Tesla. The three axis Hall probe of the gaussmeter has been calibrated using an NMR system. Figure 1 shows the magnetic field difference between the gaussmeter and NMR measurements for one of the three channels. The lines through the data are the fourth order polynomial fits. Channel one of the probe measures the radial component of the magnetic field. Channel two measures Φ component, or tangential component. Channel three measures the Z component, which is component of the field along the beamline axis. The design of the gaussmeter makes it best suited for situations where the probe is in a fixed position during data acquisition. The feature conflicts with the desire to measure the field as quickly as possible. In order to synchronize the field data with respect to the position data are acquired for 200 ms. Processing and correcting for probe errors takes 2 seconds, before the data are transmitted data through the instrument's serial port.

S800 Beamline Quadrupole Triplet Mapping

Data are stored on the internal hard drive until they are loaded to another computer for processing. At one degree step size, each revolution takes 14.35 minutes and produce a 15 kB data file. A Z-axis step of 1 cm will require 210 revolutions in order to adequately measure the length for the triplet and fringe fields. The total data file for each of these maps is 3.15 MB. A one degree map takes 51 hours to complete, with the mapping process requiring minimal operator supervision. Table 1 listed mapping time and file size.

Maps for different sets of currents have been done. Figure 2 shows the radial component of the magnetic field for the triplet when the currents for the three quadrupoles are 5, 15 and 10 A respectively.

Table 1: Mapping Time and File Size for S800 Beamline Quadrupole Triplet

Parameter	1°Steps	2°Steps	3°Steps
Triplet Mapping Time	51 hours	34 hours	17 hours
Data File Size	3.15 MB	2.1 MB	1.05 MB

The optics for fragment separation mode have fifteen adjustable parameters so tuning the beam is only practical if the gradients are accurately known. On one pole tip of each quadrupole magnet a cryogenic Hall generator was mounted to provide for setting the magnetic field. The Hall generator was calibrated with the mapper gaussmeter at a known radius with a calibrated power supply. The measured gradients as a function of current for one quadrupole are shown in Figure 3. Each quadrupole will have its own calibration of gradient versus current (by reference to the cryogenic Hall generator).

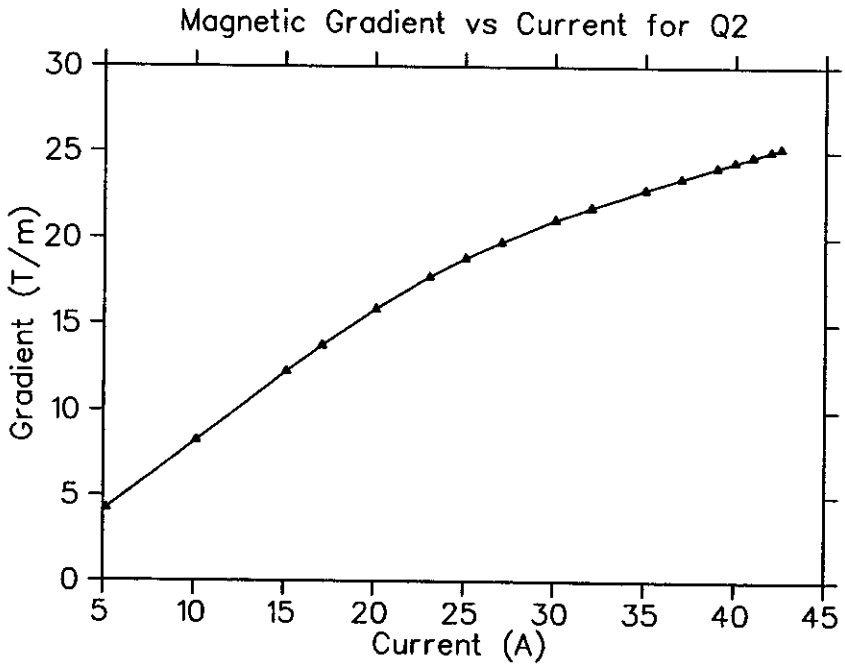

Figure 3: The gradient produced in a quadrupole as a function of current.

Magnetic Analysis of the S800 Beamline Quadrupoles

Since the S800 beamline magnets are a large version of the NSCL's standard beamline magnets which are cold iron, iron dominated superconducting magnets, they are differ from Panofsky[3] and Cos2θ in that the field shaping is done primarily by iron poles. Figure 4 shows the effective length of the S800 beamline quadrupoles as a function of current. The radial component of magnetic field at the center is shown in Figure 5. Figure 6 shows a map and the harmonic content at a radius of 7.43 cm. The sextupole error is about 3 parts in a thousand of the quadrupole field. Note that only the N=6 and 10 terms are theoretical allowed, and the rest of the terms must result from construction errors, or mapper errors.

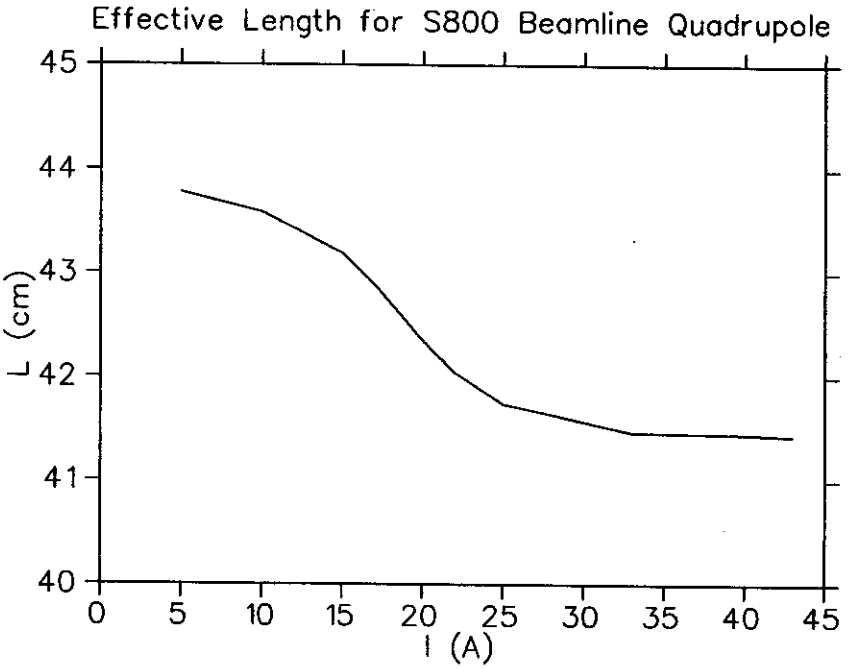

Figure 4: The effective length of the S800 beamline quadrupole as a function of current.

References

1. A. Zeller *et al.*, Superconducting beamline element for the NSCL spectrograph, *IEEE Trans. on Applied Superconductivity, Vol. 5, No. 2* 1032 (1995).
2. B. Zhang *et al.*, High gradient, large aperture quadrupoles for the NSCL superconducting spectrometer, *Adv. in Cryogenic Eng.* in press (1996).
3. L. Hand *et al.*, Magnetic quadrupole with rectangular aperture, *Rev. Sci. Insr. 39* 937 (1959).

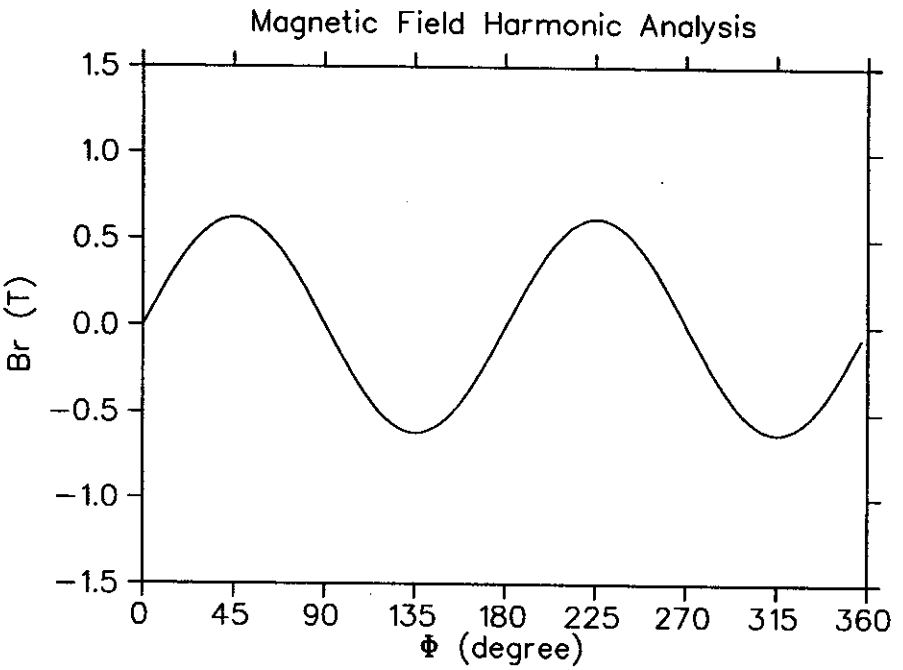

Figure 5: The radial component of magnetic field at the center at a radius of 7.43 cm.

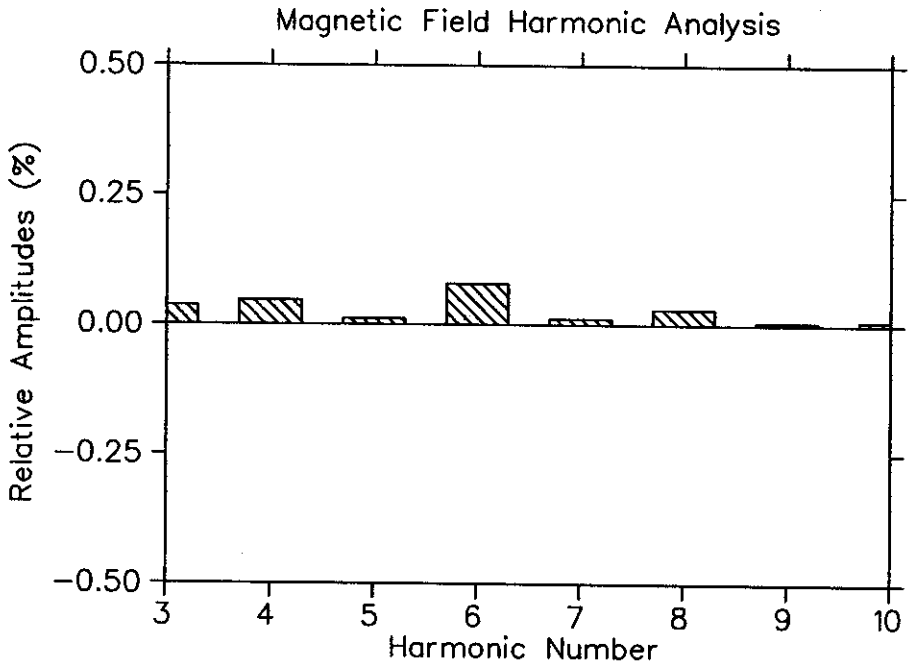

Figure 6: Fourier analysis of the radial component of the field in Fig.5.

ALIGNING THE S800 BEAMLINE

D. P. Sanderson

This report will describe how the magnetic and diagnostic elements were positioned along the beamline leading to the S800 magnetic spectrograph. In many ways the line is very similar to the A1200 mass analyzer immediately outside the K1200 cyclotron. They both have the same general shape with a radioactive beam production target at the beginning, a 45° bend, a device for viewing an intermediate image, another 45° bend, and a chamber at the focal plane of the analyzer. The main difficulty in the installation of the S800 beamline is the downward path that the beam takes into the spectrograph pit.

A layout of the S800 beamline can be seen in Fig. 1. The line begins at the switching magnet in the east end of the transfer hall. A scintillator is mounted on the exit box of the magnet. The beam passes through two room temperature steering magnets and a wall plug to enter the S3 vault, which houses the spectrograph. Immediately after the wall plug is a set of remotely controlled vertical and horizontal slits. A superconducting quadrupole doublet focuses the beam into the production target box. The box houses the target ladder for producing radioactive beams and several diagnostic devices. A superconducting quadrupole triplet follows the box to focus the beam through two 22.5° superconducting dipoles. They bend the beam down towards the bottom of the pit. A pair of quad triplets on the diagonal portion of the beamline have the intermediate image box sandwiched between them. Position sensitive detectors in this box aid in the focusing of radioactive beams through the analyzer. The pair of dipoles at the bottom of the steps bend the beam's path back to horizontal approximately 155 cm. above the floor. A small room temperature correction dipole is placed between these magnets. Two more quad triplets are positioned between the dipoles and the main scattering chamber of the spectrograph.

To provide second order corrections, four room temperature sextupole magnets are located along the beam's path. They are placed to simply fit around the beamtube at each location.

Initial Benchmarking

The path taken by the beam was constrained by the devices at each end. The path begins at the center of the switching magnet midway between the poletips. The angle out of the magnet is set by the center of the pivot bearing in the spectrograph support carriage. A level path uniquely sets the beam axis to the first bend. At the spectrograph end, the line connecting the switching magnet to the pivot defines 0° for the rotation of the spectrograph carriage. The position of the first dipole of the spectrograph on the carriage sets the beam height. At this point, two horizontal lines, parallel but displaced vertically exist. The two bend angles of 45° were chosen to provide mirror symmetry. Using a jig transit, a series of adhesive targets was laid out on the floor and steps along this path. To complete the definition of the beam axis, the distance from the switching magnet to the center of the first bend was arbitrarily chosen to provide sufficient space for the magnets. The beam characteristics are insensitive to the distance from the switching magnet to the quad doublet immediately ahead of the production target box. A target was placed on the floor directly below this first corner. To ensure equal 45° angles, a commercial digital theodolite was rented and used to shoot the path downward along the steps. A target was placed on the lower floor where this line intersected. This target would allow the jig transit to reproduce the path.

In order to be able to mount the transit at the lower level, a target was needed directly under the lower corner. One transit was mounted at the upper corner viewing the downward beam axis. Another

transit was mounted at the pivot of the spectrograph carriage viewing the horizontal portion of the beam axis upstream. A plastic target mounted in a sphere was adjusted until both transits viewed its center. At this point, the sphere was replaced by a plumb bob and mount which set the position of the adhesive target on the floor.

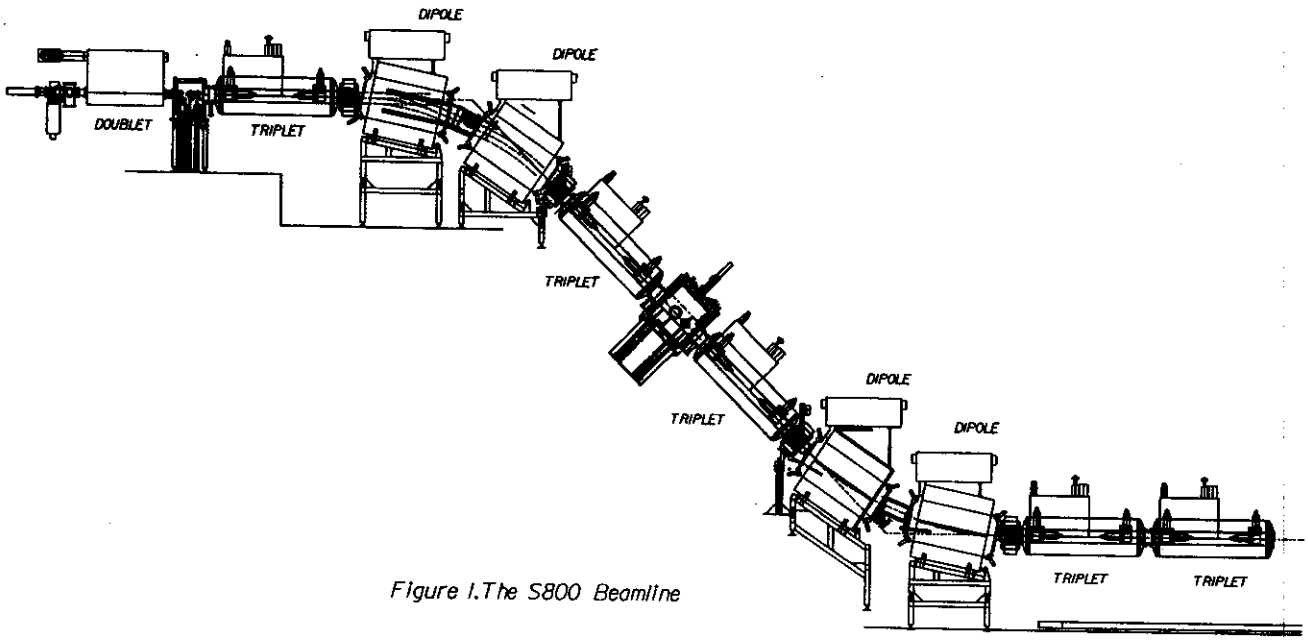

Figure 1.The S800 Beamline

Installation of the Quadrupoles

In all the installations of superconducting quadrupole magnets at the laboratory, the poletips are aligned magnetically to the centers of the vacuum flanges on each end. By installing transparent targets to the end flanges, an alignment of the targets means an alignment of the magnets. The only loose parameter is the linear position of the magnet inside the vacuum cryostat. Fortunately, the transport properties are relatively insensitive to this position and it was assumed that the magnet positions are known inside the cryostat.

During one of the cyclotron's scheduled shutdown periods, a transit was mounted at the upper corner of the beamline viewing back at the switching magnet. The internal alignment fixture for the switching magnet has a pin at the center and this was used to determine where the beam axis passed through the end of the wall plug. A horizontal and vertical displacement target was mounted at this position and the coordinates of the beam axis were recorded. This allowed the switching magnet beam hardware to be reassembled and for alignment to take place with the wall plug inserted.

With the transit in this position, the quad doublet and triplet were placed on the upper horizontal portion of the beamline. Their position along the line was set using one of the floor coordinate benchmark targets mounted in the floor throughout the laboratory. Plumb bobs were used to transfer their position to floor level.

The two triplets mounted on the steps were aligned using the same setup. Their position along the axis was determined by running a tape measure from the central axis of the transit to the entrance vacuum flange of each magnet.

The transit was moved to the pivot of the carriage to set the horizontal path at the bottom of the pit. Here, the distance from the corner of the beamline was used to set the linear positions.

Using the above methods, it was easy to position each quad horizontally and vertically to within ±0.2 mm. The error bar for the linear position is probably ±3 mm.

Installation of the Dipoles

The dipoles are positioned after the quadrupoles since targets mounted on the quad end flanges are used to adjust the optical instruments to the beam axis. Since the dipoles have identical pole tips to those in the transfer hall, the original alignment fixture was used. The fixture is an aluminum plate pinned to the pole tip with a series of dowel pins along the beam path.

At each location, the procedure is similar. The only differences are the location of the optical instrument. For the first dipole, an alignment telescope is placed at the production target position. It is adjusted to the beam axis using the targets attached to the first triplet. For the second dipole, the transit is mounted above the bottom corner of the beamline, using both of the middle triplets to set the beam axis. For the third dipole, the transit is mounted at the intermediate image position. For the last dipole, the transit is mounted above the spectrograph pivot.

For each dipole there are three coordinates and three angles to define the position of the magnet. Position left-right is set by a scale magnetically clamped to the pole tip. Position up-down is set by the dowel pins on the fixture. Position in-out is set by a plumb bob above the corner benchmark and a tape measurement to one of the pins on the fixture. Rotation about the beam axis is set by an angle plate and machinist's level clamped to the side of the return yoke. During assembly, this yoke was ground flat and parallel to the pole tip. Rotation about a horizontal axis is set by using two of the beam axis pins. Rotation about a vertical axis is set by measuring with the scale at both ends of the pole tip simultaneously.

Installation of Diagnostic Components

There are three devices along the beam path which must be aligned to work properly: the slit mechanism, the production target box drives, and the intermediate image box detectors.

The first two are aligned simultaneously. During a cyclotron shutdown, the beamtube between the switching magnet in the transfer hall and the wall plug is removed and a transit is substituted. The beam axis is recovered by installing the displacement target on the wall plug and pulling the beam tube and sextupole between the first triplet and the first dipole. This gives a clear view through the two devices to adjust the slit mechanism calibration and the location of the production target ladder.

The intermediate image detectors are much more difficult. The only way to view the interior of the box is by removing the two sextupole magnets at the ends of the triplets. Once this is done, two targets on the triplets define the beam axis. Unfortunately, there is no room for an optical instrument, so a telescope is mounted at a 90° angle to the beamline with a mirror to allow viewing of the two targets and the detectors in the box.

This report has described the installation and positioning of the active components on the S800 beamline. The techniques were able to meet the required accuracy goals without a large investment in equipment and fixturing.

AUTOMATED DATA ACQUISITION SYSTEM FOR S800 DIPOLE MAGNETIC FIELD MAPPING

J.A. Caggiano, R. Fontus II, and P.H. Johnson

Precise and accurate field maps of the two large dipoles in the S800 are important for achieving high energy resolution using ray reconstruction[1]. Precise and accurate field measurement requires a reliable data acquistion system. The present system does not differ much from the conceptual design[2]. The two large dipole magnets are arc-shaped and each one bends 75°, so data acquisition is performed in a cylindrical-coordinate system. Search coils sweep through the field in the azimuthal direction, then move radially. Five coils mounted in a straight line in the direction normal to the bending plane (z-direction) are used to measure the z dependence of the field. Only the z-component of the field is measured. Figure 1 shows a schematic of the mapper in the dipole and displays mapping coordinates.

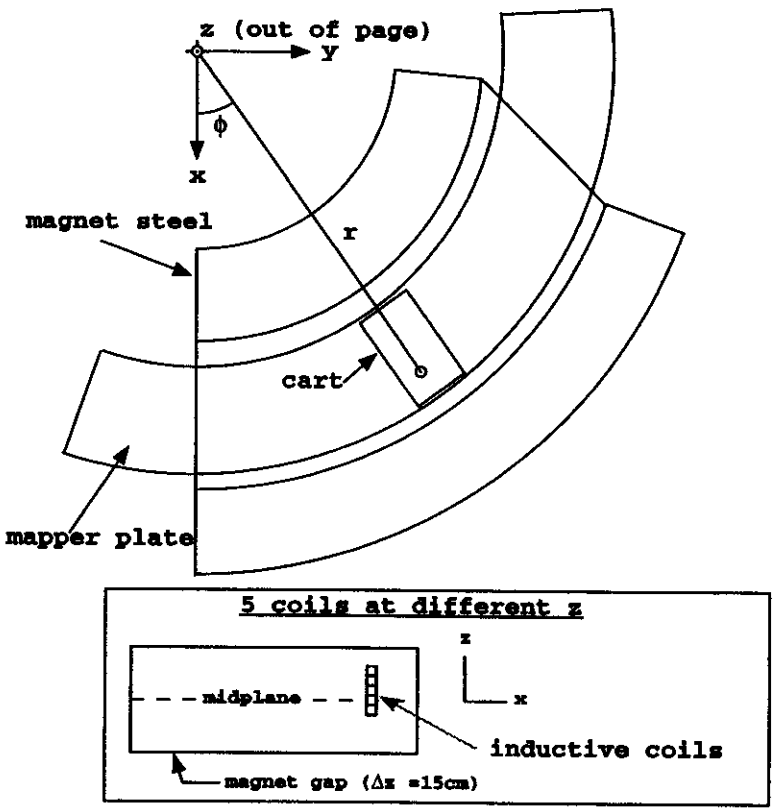

Figure 1: Schematic showing mapper coordinate system. Map data is taken in a cylindrical coordinate system. The entrance face is parallel to the xz-plane. The bottom panel shows the coils as situated about the midplane in the z-direction. One coil is in the midplane, three are above (in z) and one is below (each coil is 1/2 inch tall).

A plastic-chain driven cart is used to move the coils through the field. The cart rides on a rail which is firmly mounted to an aluminum plate which is in turn pressed to one pole face of the magnet using mechanical vacuum pumps to generate suction. Pinch rollers are used to allow the cart to ride on the rails, and 4 wheels contact each pole face to ensure the cart's motion is constrained properly along the magnetic midplane. Aluminum stabilizer bars keep the coils from tilting when moved in the radial direction.

Azimuthal position data is obtained by attaching an encoder strip to a rail, then using an infrared optosensor to detect teeth on the encoder strip. (The coils' speed is obtained by measuring the time between every third tooth edge (2.3 mm) on the strip. This has been subsequently changed to improve position resolution of the speed measurement.) Radial position data is obtained in a similar fashion with an encoder strip mounted on the cart. When using this method of position detection, it is important that the position of the encoder strip remain fixed relative to the optosensor.

The field data is gathered by moving the search coils through the field and measuring an induced voltage. The voltage induced in a coil is $V = -d\Phi_B/dt$, where Φ_B is the magnetic flux. By measuring the voltage and an appropriate time, the field is obtained simply by performing the integral. The analog voltages are converted with 18-bit integrating ADC's in the DAQ computer. The ADC integration time is measured using an integration gate signal generated by the ADC circuitry.

The DAQ computer is a 386-based system. Five ADC printed circuit boards are placed in the backplane of the computer. A PC board with two timer chips is used for timing and counting (essentially scalers with 5 scalers on each chip). Another PC board communicates with stepper motors to move the cart. Roughly 1800 lines of Turbo Pascal code control the motion of the cart and acquire data, with the timing set by the detection of the teeth on the encoder strip. Each map takes 6 hours to acquire and is 50 megabytes in size.

Several enhancements were made to the system after test mapping the first of the two dipoles. The system is now able to measure the speed of the cart every 0.38 mm as opposed to every 2.3 mm as before. This greatly reduces the uncertainty in the speed and position of the coils during the time the ADC's are integrating the voltage signal, and hence reduces the uncertainty in the field measurement. The induced voltage signals are now amplified to achieve a typical signal-to-noise ratio of about 14,000 (16 times larger than during test mapping). Improved timing techniques allow the measurement of event times to 2 microseconds (tested with a signal generator and frequency counter). (Post-processing techniques and results from test mapping are described in separate reports here[3,4].)

With the improved system, the field maps will become 12 hours long and will require roughly 180 megabytes of storage space. However, the increase in time and storage space required should be outweighed by the improvements made in the system.

References

1. M. Berz et al., "Reconstructive correction of aberrations in nuclear particle spectrographs", Phys. Rev. C 47 (2), February 1993.
2. A.F. Zeller et al., "S800 Dipole Construction", NSCL 1990 Annual Report.
3. J.A. Caggiano and B.M. Sherrill, "Data Analysis Techniques for S800 Dipole Magnetic Field Maps", NSCL 1995 Annual Report.
4. J.A. Caggiano and B.M. Sherrill, "Results from Mapping the S800 Dipole Magnets", NSCL 1995 Annual Report.

DATA ANALYSIS TECHNIQUES FOR S800 DIPOLE MAGNETIC FIELD MAPS

J.A. Caggiano and B.M. Sherrill

The goal of S800 dipole field analysis is to eventually feed the data to the computer code COSY[1] to achieve the desired spectrograph resolution through raytracing techniques. COSY doesn't just integrate the equations of motion through the fields, but rather uses differential algebra techniques to arrive at aberration terms first, then integrates the equations of motion. Consequently, noise or rapid fluctuation in the map data appears as a high order aberration, and is intolerable. Random noise of $\leq$10 Gauss is manageable due to the interpolation method used in COSY. However, random noise larger than this or systematic errors may lead to incorrect ray reconstruction and must be avoided at all costs.

The raw data is a series of voltage measurements and times, with the voltage being raw field data (first derivative) and times corresponding to position measurements from encoder strips. (The data acquisition system is described in more detail in reference 2.) The raw data are first corrected for acceleration of the search coils, and the coil voltages are integrated to produce the field. Data are taken on a polar-coordinate grid as shown in Figure 1, and only the field component normal to the bending plane is measured. Using z to denote the direction normal to the bending plane, the measurements yield $B_z(r, \theta, z)$. There are 5 planes of data; one plane is the magnetic midplane, one plane is below, and three are above. This is done to check the off-midplane expansion calculated by COSY from the midplane data and to highlight any asymmetries present.

Interpolation from Cylindrical to Cartesian Coordinates

The current version of COSY only accepts magnetic field data on a cartesian grid. Consequently the data must be interpolated from the polar grid. Several routines were tested for accuracy. The tests were performed by using a known function to determine the level of accuracy one can achieve at the interpolated points. The test function is a product of an azimuthally dependent fermi function and a radially dependent gaussian, similar to the field shapes of the real magnets. Table 1 illustrates the dependence of the reproduction accuracy as a function of routine for a few selected routines.

Table 1. Maximum percent error in function reproduction for a few interpolation routines. These results are for clean data; noisy data increases the maximum percent error by roughly 1000 times.

Grid Spacing	3rd Order Lagrange	IMSL Akima Spline	CERN Newton Divided Difference
1 cm	0.00073	0.0039	0.00074
5 mm	0.00139	0.0039	0.00139
3 mm	0.00142	0.0039	0.00142
1 mm	0.00160	0.0039	0.00162

The Lagrange interpolation routine was chosen because of its accuracy in reproducing the function and its derivatives up through 3rd order.

One unfortunate feature of most interpolation routines is inability to handle noisy data well. In fact, adding noise into the test function rapidly degraded the ability of these interpolation routines to

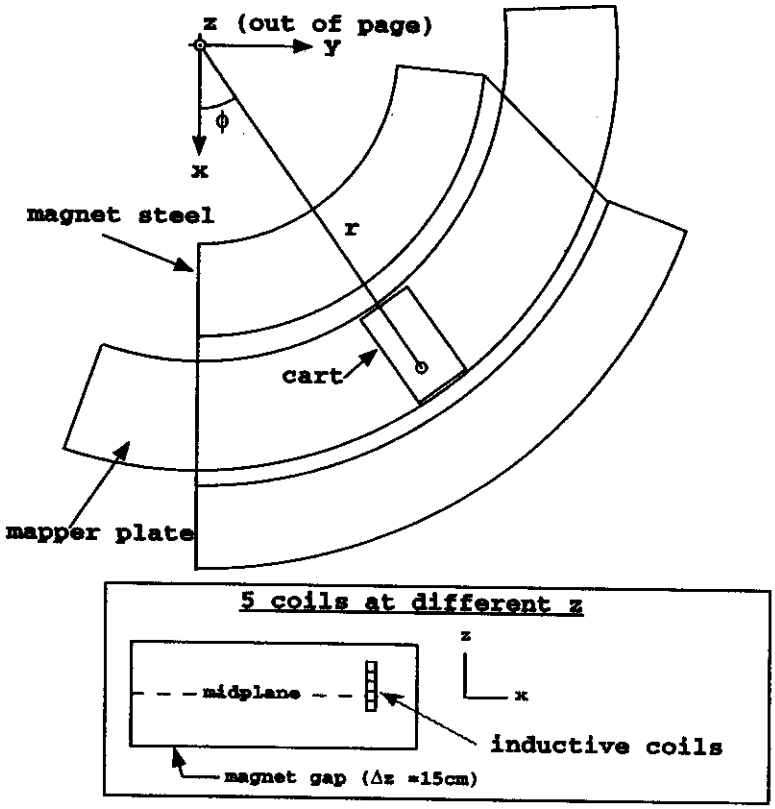

Figure 1: Schematic showing mapper coordinate system. Map data is taken in a cylindrical coordinate system. The entrance face is parallel to the xz-plane. The bottom panel shows the coils as situated about the midplane in the z-direction. One coil is in the midplane, three are above (in z) and one is below. Each coil is 1/2 inch tall.

reproduce the underlying function. It is therefore important to do any smoothing to the data before interpolation to the cartesian grid is performed.

Data Smoothing

Several fairly simple smoothing techniques were employed. Single and piecewise polynomial fits in the radial direction were tried as well as a gaussian sum fit[1] in the radial direction. Fits in the radial direction are chosen because the field gradients are relatively low in this direction compared with those in the azimuthal direction. Reproducibility of maps serves as a good evaluation tool until there is beam in the spectrograph. Raw, polynomial-smoothed, and gaussian- smoothed data were compared for two identical maps. Table 2 shows the maximum differences between two identical maps for each of the 3 cases.

Table 2. Maximum errors (in Gauss) between two identical maps (B = 1.36 Tesla) for raw, polynomial-smoothed, and gaussian-smoothed data. The maximum errors occur at the exit edge of the dipole, while errors at the entrance edge and in the flat field region are considerably smaller.

Data	Maximum error (Gauss)
Raw	100
Polynomial-smoothed	20
Gaussian-smoothed	5

Figures 1, 2, and 3 show the raw, polynomial smoothed, and gaussian smoothed data, respectively. The improvement in both appearance and reproducibility is encouraging.

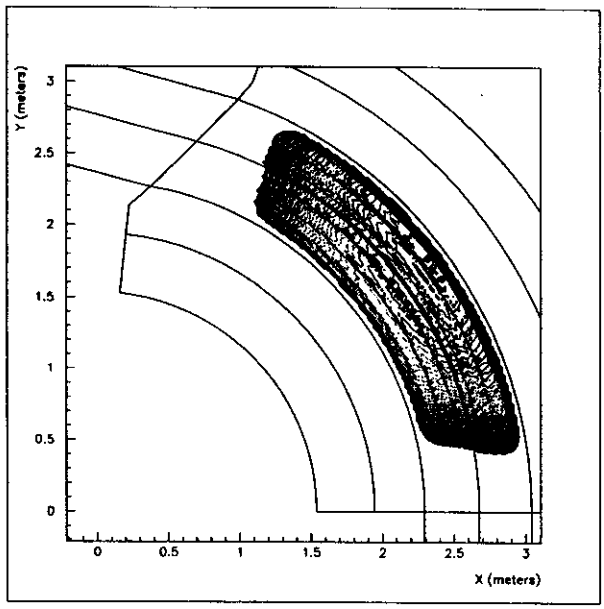

Figure 2: Raw data for 400 amp map with no current in the trim coils in the flat field region of the magnet. Contours are every 2 Gauss, starting at 1.56 Tesla and increasing. The black lines are outlines of the magnet steel and of the beam pipe and its center. The coordinates in the plot are (x,y) in meters, with the origin at the center of the arcs of the magnet steel.

Choosing Data Resolution

COSY uses a two dimensional gaussian interpolation to create the field and all of its derivatives at any point in space within the extent of the beam pipe. The grid spacing of this data matrix plays a key role in how accurately the field data can be reproduced.

Choosing the resolution of the raw data was done in the following manner. A test was done to evaluate whether the data grid spacing was sufficient for the accuracy desired. The test was done by creating a mock field using a Fermi function in one cartesian direction and a gaussian in the other. The parameters of the function are adjusted to match the maximum forseeable first derivatives in the fields. Table 3 shows how the accuracy of data reproduction depends on the grid spacing. The desired accuracy is 1 part in 10^4, so it is clear that a 2.3 mm data grid is sufficient.

Table 3. Maximum percent errors in function reproduction with different mesh sizes. The goal is $\leq$0.01%, so point spacing of $\leq$ 3mm is sufficient.

Grid Spacing	Maximum percent error
2 cm	0.30
1 cm	0.10
5 mm	0.02
3 mm	0.01

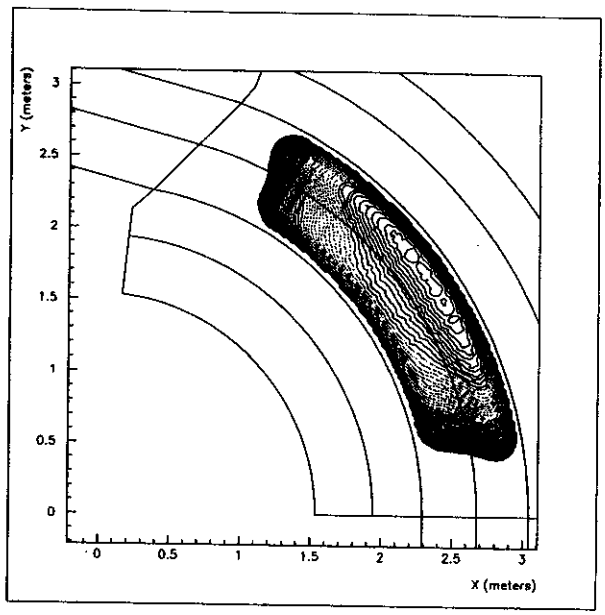

Figure 3: Similar to figure 1 except a radial polynomial smoothing routine is applied to the data. A substantial improvement over the raw data is evident.

Conclusions

Despite hardware shortcomings which may exist, it is possible to produce meaningful dipole field maps using the software techniques described here. Eliminating errors in hardware are sometimes much harder and more costly, so these techniques provide cost effective tools for repairing errors in the data.

References

1. M. Berz, et al., "COSY Infinity Version 7 User's Guide and Reference Manual", NSCL report MSUCL-977, June 1995.
2. J.A. Caggiano, et al., "Automated Data Acquisiton System for S800 Dipole Magnetic Field Mapping", NSCL Annual Report for the year 1995.

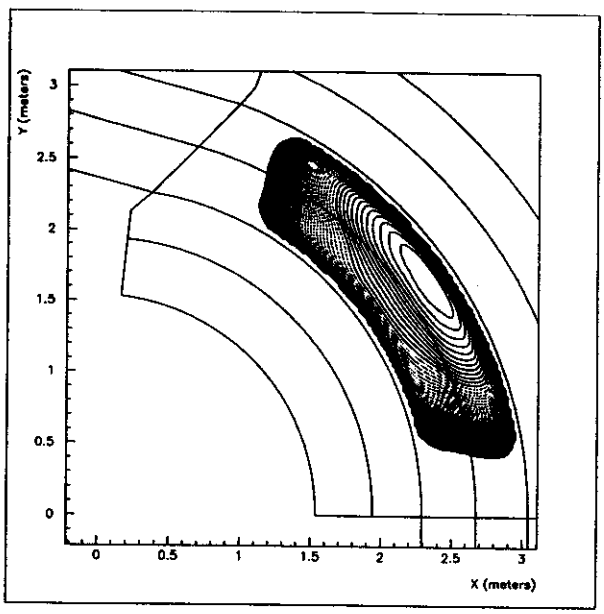

Figure 4: Similar to figures 1 and 2 except a radial gaussian sum fitting routine is applied to the data. All rapid fluctuation in the map data has disappeared.

RESULTS FROM MAPPING THE FIRST S800 DIPOLE MAGNET

J.A. Caggiano and B.M. Sherrill

In May of 1995 a large sample of field data of the first S800 dipole magnet, D1, was taken using the new magnetic field mapper. The field mapper is described in a separate annual report[1]. The maps were taken to test the data acquisition system, and to find (and eventually fix) errors in the mapping process before final mapping takes place. Some of the basic dipole properties, such as effective length, were measured also. These data, while useful in some respects such as comparison with design criteria and error detection, will eventually be replaced by field maps with both dipoles (D1 and D2) present. A few select results will be shown here.

The extent of the effective edge of the steel was measured for both entrance and exit faces. This was done by interpolating the data onto the central trajectory then integrating the field along this trajectory using Simpson's rule (see Figure 1). The effective edge at the angled face is considerably longer due to the edge angle. The positions of D1 and D2 were adjusted to reflect this.

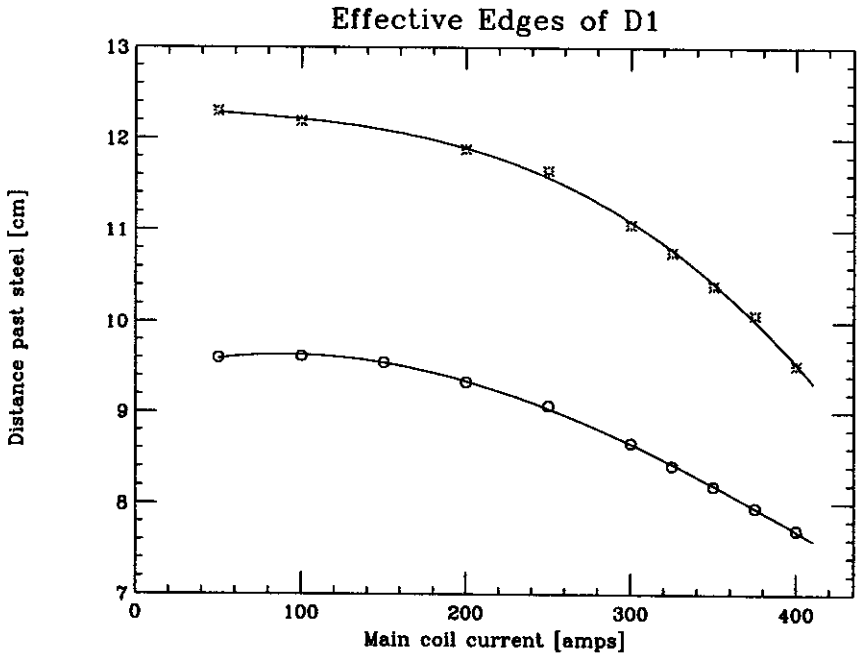

Figure 1: Effective field extension past the steel for the entrance and exit edges of D1. The top set of points are for the exit (angled) edge, and the bottom set are for the entrance edge. Lines through the data are third order polynomial fits.

Calibration of the search coil system was performed with a combination of NMR and Hall probe measurements. The NMR probe was placed at a known position in the flat field region. The Hall probes measured the initial field for the search coils, and also measured the radial shape of the field. Absolute position was determined with small magnets placed on the magnet steel. Figure 2 shows a sample plot of the field of the small magnet at the edge of the steel. This is a very accurate way of determining absolute position of the mapper in the magnet. Depending on the size and strength of the small permanent magnet

chosen, it is possible to attain absolute position calibration to $\leq 10\ \mu m$.

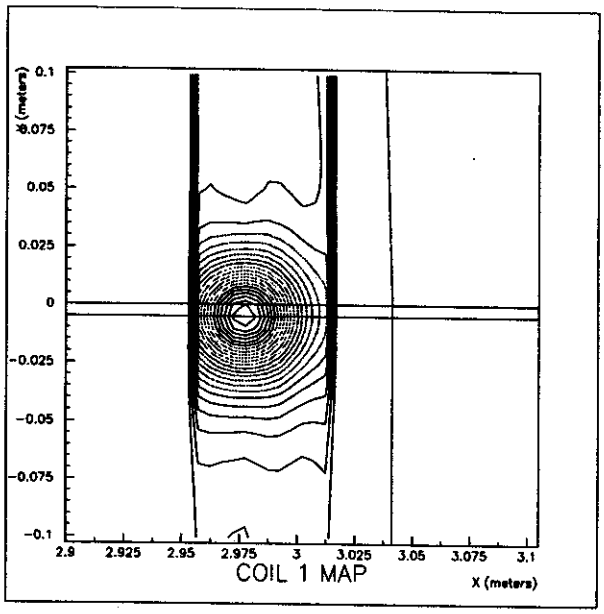

Figure 2: Local map of a small magnet used to position the mapper with respect to the steel. The axes are (x,y) coordinates in meters, with the origin of the coordinate system coinciding with the center of the arcs of the magnet steel. The line through the center of the 'bullseye' is 5 mm away from the edge of the steel, exactly where the center of the magnet is. Contours are every 3.2 Gauss.

Once the data is calibrated, then corrections to the position and shape of the field can be made. Figure 3 shows a typical full map, with outlines of the mapper and the magnet steel and central trajectory.

Trim coils are present for increasing the region of 'good' field, which enhances the resolution of the spectrograph. 'Good' field refers to a flat field region that has a radial gradient of ≤ 1 Gauss/cm[2]. Figures 4 and 5 illustrate the effect of the trim coils in the main field region of the magnet. The trim coil settings are 1% of the ampere-turns of the main coils. There is a very notable curvature of the field at the inner and outer radii of the gap, but this is corrected rather well with the trim coils.

These data taken in D1 demonstrate that the first dipole magnet in the S800 spectrograph meets or surpasses the design criteria as put forth in the S800 proposal[2]. These data also demonstrate the reliability and sensitivity of our mapper system. Errors in the mapping process were identified and eliminated as described elsewhere[1].

References

1. J.A. Caggiano, et al., "Automated Data Acquisiton System for S800 Dipole Magnetic Field Mapping", NSCL Annual Report for the year 1995.
2. J.A. Nolen Jr., et al., "A Proposal for Construction of the S800 Spectrograph", NSCL internal report MSUCL-694, July 1989.

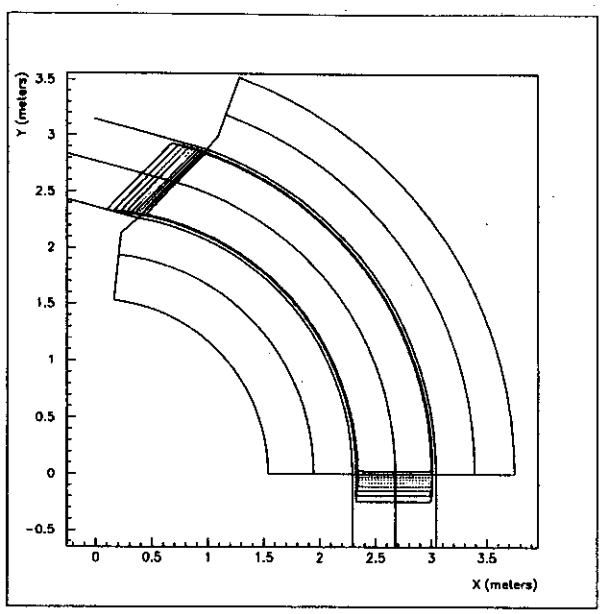

Figure 3: Typical midplane data plot for the S800 dipole field maps. These data were taken at B=1.57 Tesla, $I_{maincoil}$ = 400 Amps and $I_{trimcoils}$ = 175 Amps. The black lines are outlines of the magnet steel and of the beam pipe and its center. Contours are every roughly every 1600 Gauss.

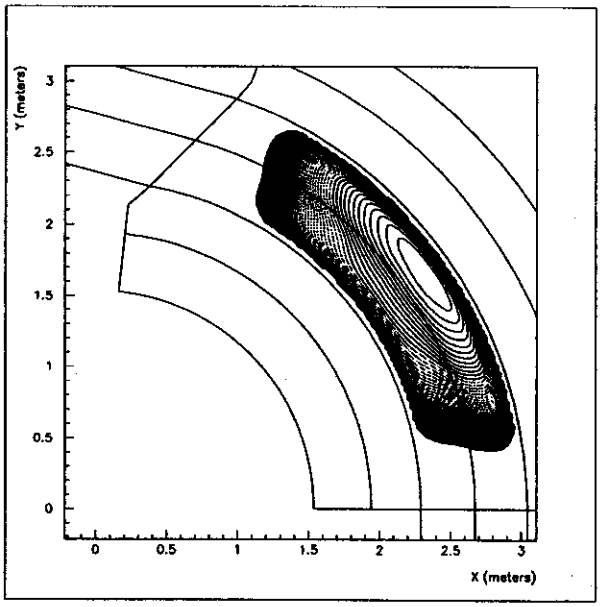

Figure 4: Midplane field data for 400 amps with no current in the trim coils. Notice the curvature of the field along the inner and outer radii. Contours are every 2 Gauss starting at 1.56 Tesla and going up.

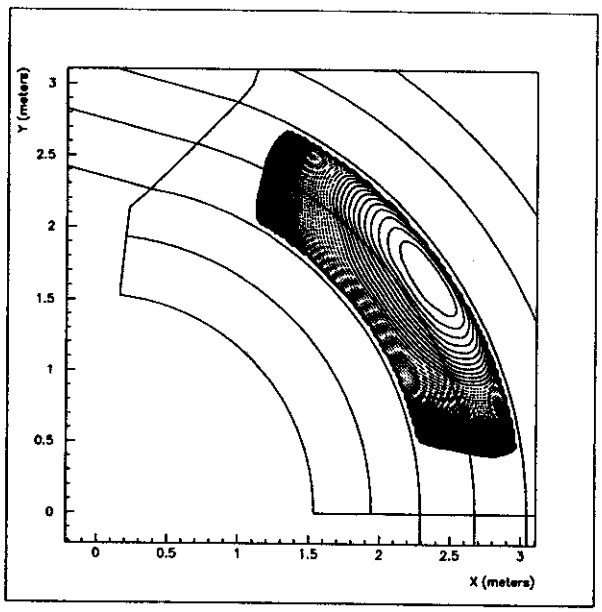

Figure 5: Midplane field data for 400 Amps (1.57 Tesla) with the trim coils at their optimum value of 175 Amps. The field is substantially flattened due to the trim coil operation. Contours are every 2 Gauss.

METHODS FOR FRINGE FIELD MODELING - APPLICATION TO THE DIPOLES OF THE S800 SPECTROGRAPH

D. Bazin and B.M. Sherrill

One of the most important issues in a high resolution spectrograph such as the S800 is the ability to correct for the high order aberrations of the system. Most of these aberrations occur in the fringe field region where the magnetic field has a large gradient, and the field caused by the bobbin gradually comes into play at large distances from the iron. The method chosen to correct for these aberrations in the S800 spectrograph is to calculate the transfer map up to a high order on the basis of the measurement of the magnetic field. The computer code COSY INFINITY [1] will be used to perform the transfer map calculation. Two different approaches to model the fringe fields are possible. The first uses an analytical function known as Enge function to fit the shape of the fringe field. The second is based on an array of gaussian functions defined such that their sum at any location is equal to the value of the magnetic field. This method is known as gaussian interpolation, the reason for choosing gaussian functions being that they are infinitely derivable. Both methods have been used to try reproducing the data taken on the first dipole of the S800 during the first mapping campaign [2].

Enge function fit

The typical shape of the fringe field measured on the first dipole of the S800 is shown in Fig. 1. In the inset is a blow-up of the tail of the field, showing that it becomes negative before converging to zero.

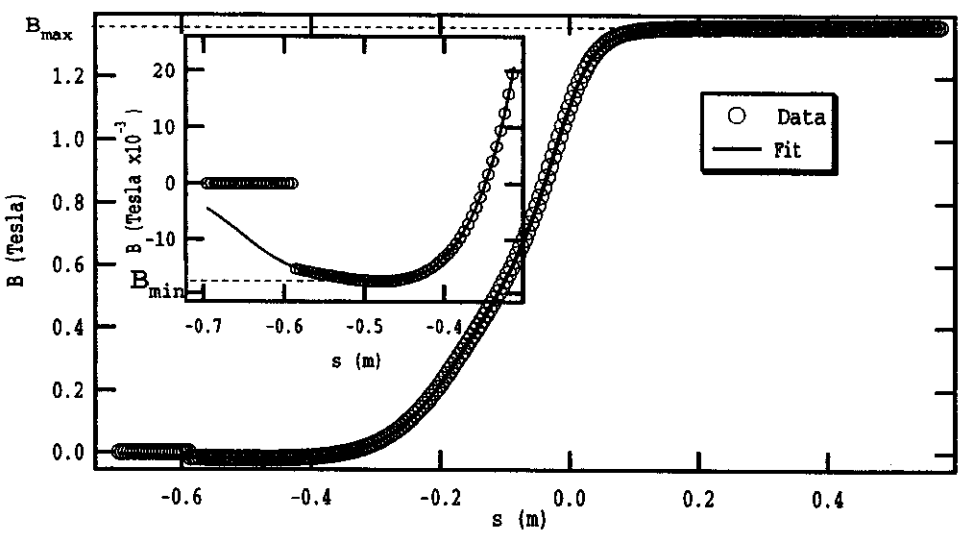

Fig 1 : Entrance fringe field of the first dipole of the S800 measured at 1.36 Tesla. The coordinate s=0 corresponds to the edge of the pole face. The inset shows the detail of the fringe field tail where the field becomes negative. The Enge+Fermi function fit is able to extrapolate the field where no measurements have been made.

This inversion is caused by the field of the bobbin which becomes larger than the fringe field of the iron at large distances from the iron. The Enge function has the functional form :

$E(z)=\frac{1}{1+\exp(\sum_{i=0}^{n} a_i (z/d)^i)}$ where z is the distance to the effective field boundary and d the full aperture of the magnet. The order n of the polynomial can be varied to adjust the number of degrees of freedom. However, such a functional form is unable to reproduce the negative overshoot of magnetic field observed in the tail of the fringe field. The shape of the fringe field was fitted using the following function: $b(z)=\left[(1-b_{min})*E(z)+b_{min}\right]*\frac{1}{1+\exp(c_0+c_1(z/d))}$ where b_{min} is the minimum value of the reduced field ($b_{min}=B_{min}/B_{max}$). Written in this form, the Enge function starts at b_{min} away from the magnet, and reaches 1 inside. It is then multiplied by a Fermi function with coefficients c_0 and c_1 fitted to reproduce the tail of the fringe field away from the magnet. As can be seen in the inset of fig. 1, not only the shape of the fringe field tail is well reproduced, but the Fermi function also provides a smooth extrapolation of the field where there is no measurement. The fitting algorithms used are a simple least square on the data transformed by the function $f(x)=\log(1-\frac{1}{x})$ for the polynomial, and a Levenberg-Marquardt algorithm for the remaining Fermi function.

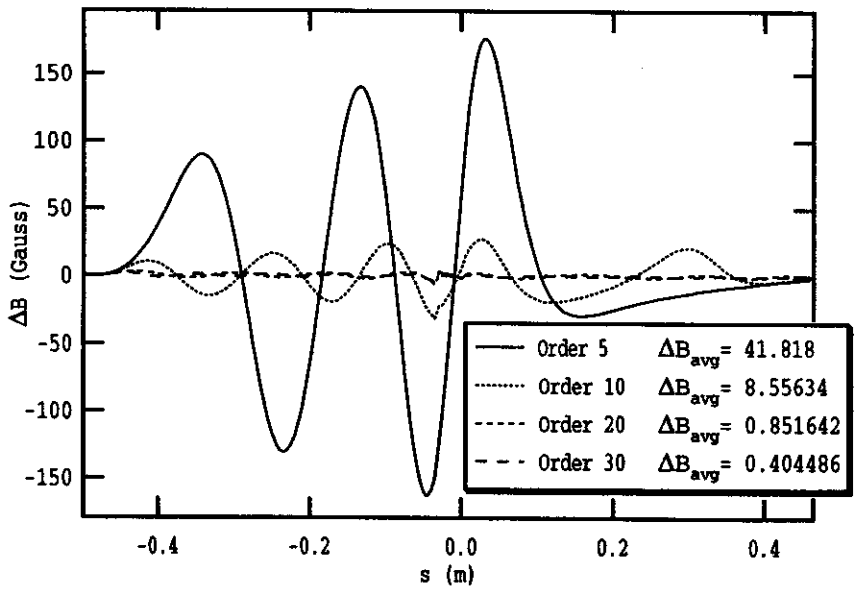

Fig. 2 : Residuals of Enge+Fermi function fits for polynomial orders 5, 10, 20 and 30 respectively. The average deviations are indicated in Gauss in the legend box.

The accuracy to which the Enge+Fermi function fit reproduces the fringe field was tested for different orders of the polynomial. The plot of residuals is shown in fig. 2 for orders 5, 10, 20 and 30 respectively. The oscillations observed correspond to the poles of the polynomial. The average deviations for each fit are indicated in the legend box, and show that an order of at least 20 is required in order to reduce the deviation below 1 Gauss in average. The results of the out-of-plane field expansion calculated with this functional are presented in [3].

Gaussian interpolation

The other method investigated for the modeling of the fringe fields uses an array of Gaussian functions. The advantage of this method is the ability to easily model the radial dependence of the field, which is the dimension relative to the central orbit, as opposed to the one-dimensional function fit where no radial dependence is assumed. The field at any location (x,s) is given by (where s is the curvilinear coordinate along the central radius, and x the radial coordinate):

$$B(x,s)=\frac{1}{\pi S^2}\sum_i\sum_j B_{ij}\exp\left[-\frac{(x-x_i)^2}{S^2\Delta x^2}\right]\exp\left[-\frac{(s-s_j)^2}{S^2\Delta s^2}\right].$$

The B_{ij} are the measured field values at x_i and s_j on a grid of spacing Dx and Ds. The parameter S is the reduced width of the Gaussians. As pointed out in [4], the choice of S is somewhat delicate, as it depends on the shape of the measured field. For small derivatives, a larger value is desirable (around 1.8) in order to prevent the structure of the Gaussians

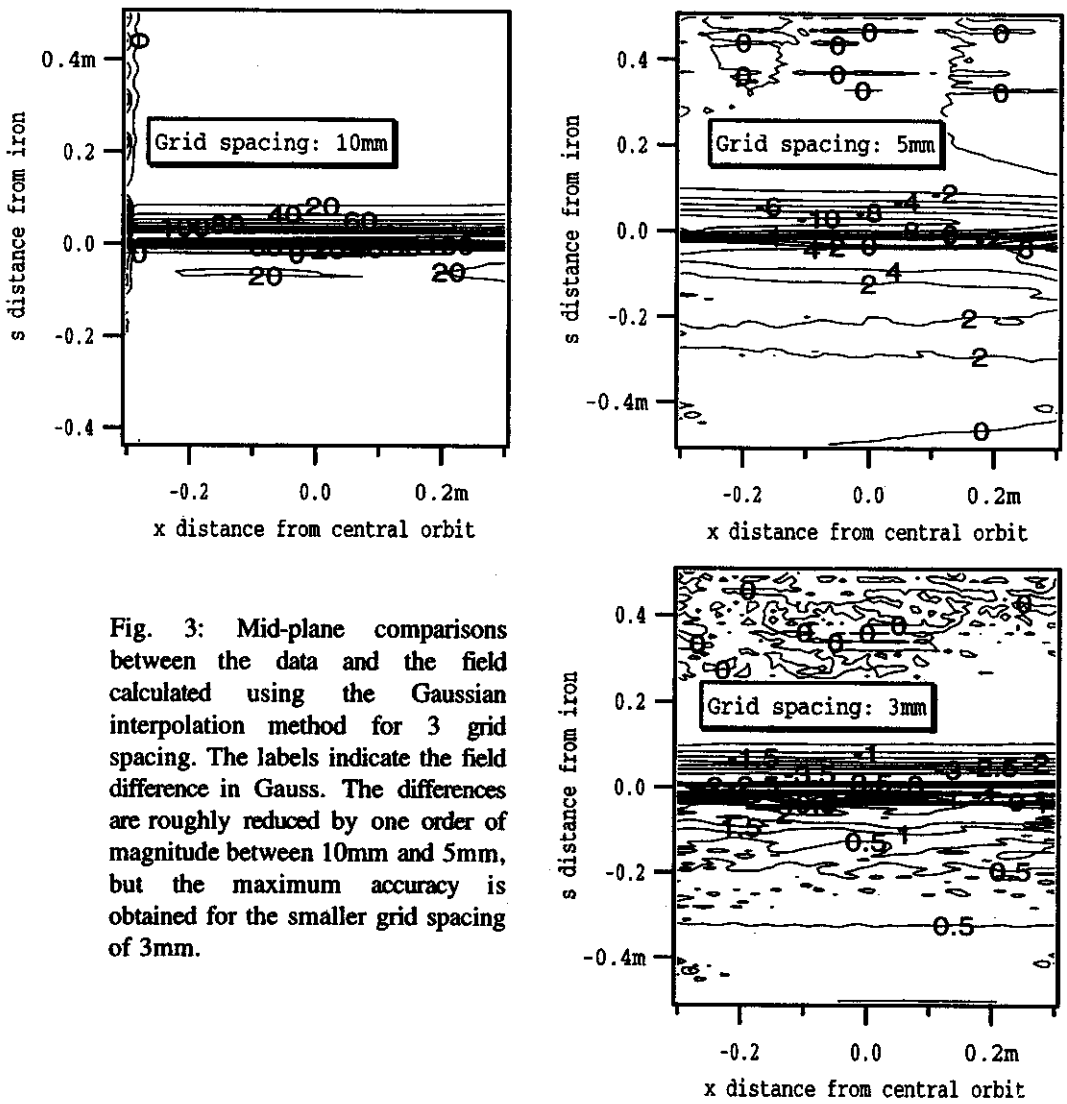

Fig. 3: Mid-plane comparisons between the data and the field calculated using the Gaussian interpolation method for 3 grid spacing. The labels indicate the field difference in Gauss. The differences are roughly reduced by one order of magnitude between 10mm and 5mm, but the maximum accuracy is obtained for the smaller grid spacing of 3mm.

from showing up, whereas for large derivatives, a smaller value (around 1.2) will follow the shape of the

data better. The choice of Gaussians (in principle any bell-shaped function could be used) is driven by the fact that they are infinitely derivable, and can therefore be used to calculate the out-of-plane expansion to any order.

The accuracy to which the Gaussian interpolation can reproduce the mid-plane field depends on the grid spacing used. The maximum accuracy attainable is given by the mapping grid spacing and is of 0.09" = 2.286 mm in both x and s directions. The comparisons between the field as calculated by COSY using the Gaussian interpolation, and the mid-plane data are shown in fig. 3 for grid spacing of 10, 5 and 3 mm. The region most sensitive to errors is located where the field gradient is maximum. In that region, discrepancies of up to 100 Gauss, or 0.7% are observed. A reduction of the spacing by a factor of 2 improves the interpolation by roughly an order of magnitude. Ultimately, the finest pitch of 3mm gives the best result with maximum deviations around 3 Gauss.

Conclusion

A comparison between the Enge+Fermi function fit and the Gaussian interpolation shows the advantages and drawbacks of each method. The Enge+Fermi function fit is able to reproduce the fringe field very accurately, provided the number of coefficients in the polynomial is increased to at least 20. The advantage of this method is the small number of coefficients needed to reproduce the shape of the fringe field. However, this method does not reproduce the radial dependence of the fringe field, which can become important at high field when the iron becomes saturated. A global two-dimensional fit assuming a radial dependence of the Enge+Fermi coefficients would be necessary to reproduce the radial component of the field. This method has not yet been investigated.

On the other hand, the Gaussian interpolation allows a full mapping of the fringe field in both x and s dimensions. However, in order to reach the same level of accuracy as for the functional fit method, the grid spacing has to be small enough to be able to reproduce the variations of field where the gradient is maximum. This leads to a rather large array of coefficients which is heavy and difficult to use in the calculations. The out-of-plane expansions based on these two methods are exposed in [3], where other considerations such as noise in the data come into play and modify the balance in the choice between them. Ultimately, both methods will be carried out to the final step where a transfer map of the full spectrograph is produced and inverted for ray-tracing reconstruction. The differences between these transfer maps, as well as the confrontation of the reconstruction with the data will tell which method is the most accurate and/or practical for achieving the high resolution goals of the S800 spectrograph.

References

1. M. Berz *et al.*, Phys. Rev. C **47**, 537 (1993)
2. J. Caggiano, contribution to this Annual Report: *S800 Dipole Magnetic Field Mapping Results.*
3. D. Bazin, contribution to this Annual Report: *Comparison between Out-of-Plane expansion and measured field on the first dipole of the S800 spectrograph.*
4. M. Berz, COSY INFINITY, Version 7, User's Guide and Reference Manual, MSUCL-977, June 1995.

COMPARISON BETWEEN OUT-OF-PLANE EXPANSION AND MEASURED FIELD ON THE FIRST DIPOLE OF THE S800 SPECTROGRAPH

D. Bazin and B.M. Sherrill

The procedure which will be used to achieve the high resolution of the S800 spectrograph involves the calculation of the out-of-plane fields in the dipoles. This expansion is internal to the COSY INFINITY [1] procedures used to calculate the transfer map of the spectrograph, and assumes a perfect mid-plane symmetry. It is therefore of crucial importance to verify this assumption, as well as test the validity of the out-of-plane expansion before any confidence can be placed in the calculated transfer maps.

The first campaign of mapping of the first dipole of the S800 spectrograph [2] has provided a measure of not only the mid-plane field of the magnet, but also the Out-of-plane field at 4 different locations. Two of those locations were equally distant from the mid-plane, hence providing a test of the mid-plane symmetry. Fig. 1 shows the difference in magnetic field (in Gauss) measured by the two sensing coils symmetric about the mid-plane for the entrance (a) and the exit (b) fringe field regions.

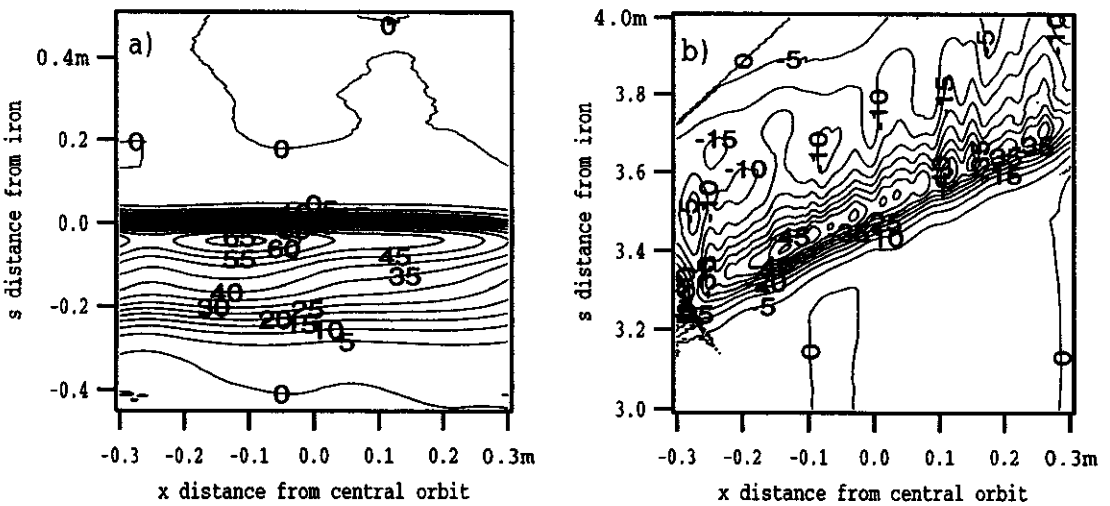

Fig. 1 : Field difference (in Gauss) between the +1/2" and -1/2" sensing coils for the (a) entrance and (b) exit fringe field regions at 1.36 Tesla. The two coordinates are the radial position x relative to the central orbit, and the circular coordinate s measured from the iron on the entrance of the magnet.

The differences observed are maximum in the fringe field regions, where the field is dominated by the bobbin, and have opposite signs from one end of the magnet to the other. These differences were first interpreted as a misalignment of the bobbin with respect to the mid-plane. However, at the time of this writing, their investigation suggests that it is rather the positionning of the sensing coils which is responsible for the observed asymmetry. The maximum field gradient in the fringe field regions being around 50 to 60 Gauss per mm, a misalignment of the order of a mm in the s direction can explain the magnitude as well as the sign of these differences. A measure of the location of each sensing coil using a locater magnet has confirmed this diagnosis. A method to precisely calibrate the position of each individual sensing coil is under development for the next mapping campaign.

As a result of this misalignment, the comparison between out-of-plane expansions based on the mid-plane field and the out-of-plane field measurements shown in the following are distorded. Two expansions were performed based on the two separate methods used to model the mid-plane field exposed in another contribution to this annual report [3]. One method uses a Gaussian interpolation algorithm, whereas the other is based on the more conventionnal Enge function fitting method.

The out-of-plane expansion calculations were performed using COSY INFINITY. A special procedure was derived from the existing procedure which calculates the potential away from the mid-plane in a Differential Algebra (DA) environment. The magnetic field is then simply deduced by taking the derivative of this potential. A set of "calculated field maps" can hence be generated by calculating the magnetic field at the location of each sensing coil. These maps can then be directly compared to the measured out-of-plane field maps. They can be calculated to any order and therefore are in principle able to reproduce any higher derivative present in the field maps.

The comparisons shown in the following were made only in the fringe field regions (mostly the in the entrance fringe field) since this is the place where the field gradients are the highest and where the high order abberations are the biggest.

Expansion from Enge function fitting

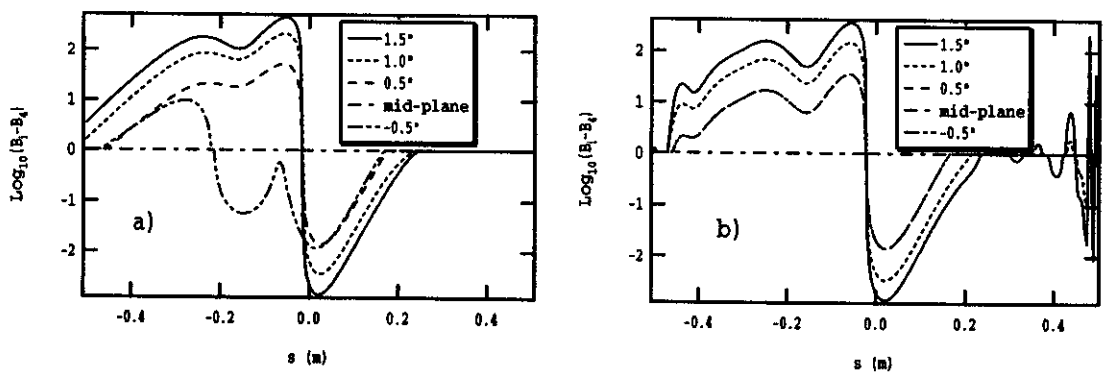

Fig. 2 : Logarithm in base 10 of magnetic field differences in Gauss between each sensing coil and the mid-plane coil for the measured data (a) and the COSY calculation (b) using the Enge+Fermi function fit. Negative logarithms correspond to negative differences, and the logarithm of differences between -1 and +1 Gauss is set to 0.

The traditional method used to simulate fringe fields is to fit them with Enge functions of typically 6 coefficients. However, as exposed in [3], the level of accuracy required for the S800 spectrograph and the fact that the fringe field becomes negative before going to zero required a more sophisticated fitting function. As exposed in [3], the number of coefficients of the Enge function was increased to 30, and a Fermi function was factorized in order to reproduce the negative part of the fringe field. Fig. 2 shows a comparison between the measured fringe field and the calculated one with the fitting function. In order to emphasize small differences, the quantities plotted are the logarithm in base 10 of the field differences in Gauss between each sensing coil and the mid-plane coil. The negative values correpond to negative differences, and the logarithm of differences between -1 and +1 Gauss is set to 0.

The data (a) show the mid-plane asymmetry mentioned earlier between the +0.5" and the -0.5" coil. The COSY calculation (b) reproduces the main features of the fringe field. However, two differences are striking. The calculation shows a small dip at the beginning of the fringe field which is not present in the data. This dip is caused by the adjunction of the Fermi function on the tail of the fringe field, which

introduces unsmoothness in the higher derivatives (the calculation shown here was done to the 5th order). At the end of the fringe field, the calculation starts to show oscillations which are due to instabilities of the 30 coefficient polynomial of the Enge function outside the fitting domain, even though it has been extended past the fringe field region.

A direct comparison of the field measured and calculated at 1.5" away from the mid-plane is shown on fig. 3 for various calculation orders. The main dip located close to s=0 can be attributed to the misalignment of the coils causing the mid-plane asymmetry. The plot shows a rapid convergence of the difference as the calculation order increases up to the 9th order, with almost no improvement between the 5th and 7th orders. However, the oscillations noticed on the previous plot become highly instable as the higher derivatives start to diverge. This problem can be solved by constraining the polynomial to remain stable further away from the fringe field region.

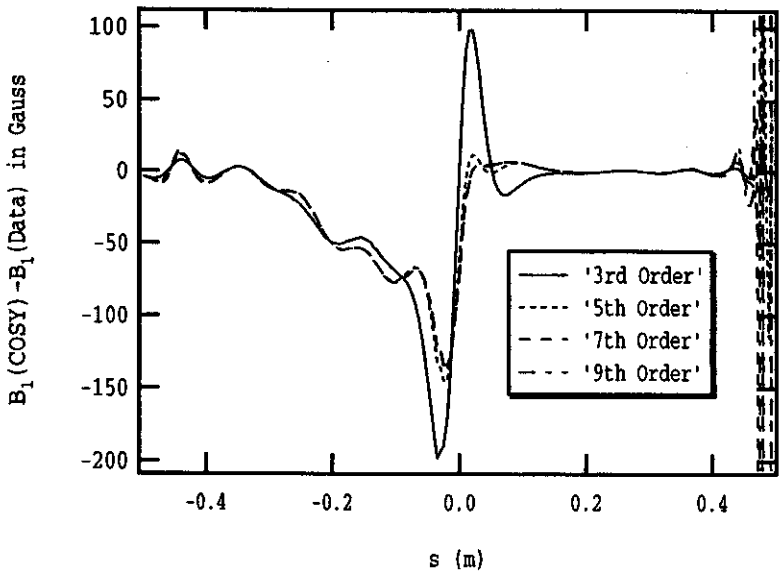

Fig. 3 : Plot of the difference between the COSY calculation and the measured field 1.5" away from the mid-plane. The different curves correspond to different calculation orders.

Expansion from Gaussian interpolation

The second method used to calculate the out-of-plane field expansion is based on the gaussian interpolation method exposed in [3]. The adjustable parameters are the grid spacing on which the interpolation is performed, and the reduced width of the individual gaussians. The advantage of this method is that the radial dependance of the field is taken into account in the calculation of the transfer map, whereas the Enge+Fermi function fit expansion assumes no dependance. It has been shown [3] that a grid spacing of 3mm, which corresponds to the maximum spacial resolution of the field map, gives the best reproduction of the mid-plane data. The out-of-plane expansions presented next were based on such a grid spacing, with a reduced width of 1.4 for the gaussians (meaning that the FWHM is 1.4 times the grid spacing).

The comparison between out-of-plane field expansion and actual measured field are shown in the next figure for the entrance fringe field region of D1. The COSY calculations were performed from 2nd to 5th order, at a distance of 1.5" away from the mid-plane. The discrepancy inherent to the misalignment of the sensing coils mentionned earlier is of course also present, and has the same magnitude as in the Enge+Fermi function fit (see fig. 3). However, as the calculation order increases, instabilities due to noise and unsmoothness in the mid-plane data start to develop. At the 5th order, the calculated field is dominated by these instabilities which are present mostly in the higher order derivatives.

There are two ways to reduce these instabilities. One could increase the reduced width of the gaussians, hence reducing the unsmoothness of the interpolated mid-plane field. Unfortunately, this method also washes out the fine details of the field map, and the calculated out-of-plane expansion eventually becomes unrealistic. The other possibility is to reduce the noise and systematic errors of the measured field data. One important source of systematic error present during the first mapping campain

was due to the unsmoothness of the mapper's cart velocity. Because the magnetic field is measured by integration of the sensing coil voltage over a given distance, this unsmoothness was directly transfered to the field data. This problem will be overcome in the next mapping campaign by accurately measuring the velocity during each integration sample [4]. Amplifiers have also been added on the sensing coil channels in order to improve the signal to noise ratio [4].

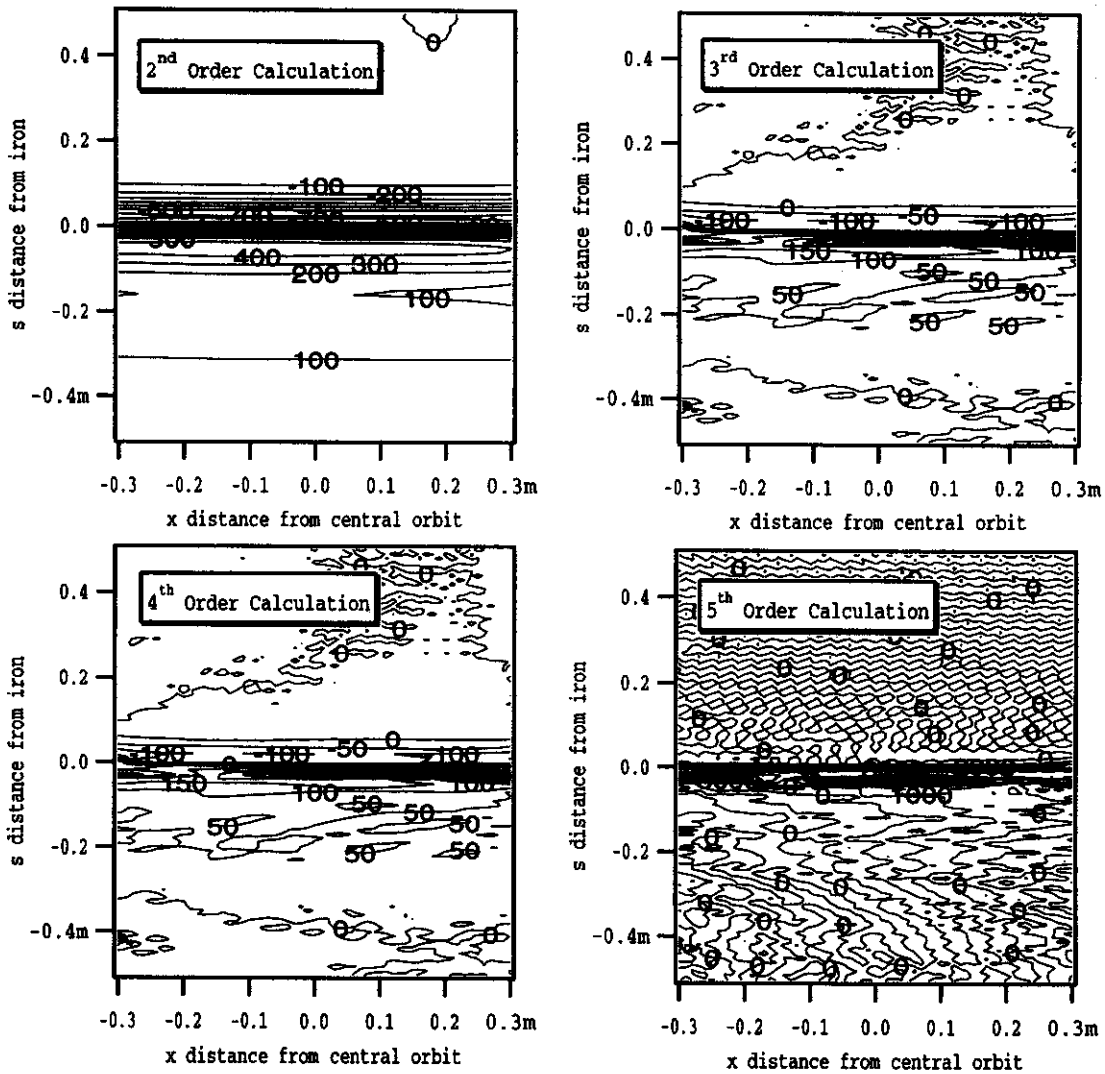

Fig. 4 : Direct comparison between calculated and measured out-of-plane field (in Gauss) for the entrance fringe field region of D1, 1.5" away from the mid-plane. The COSY calculations are based on a gaussian interpolation of the mid-plane field, from order 2 to 5.

Conclusion

The first attempts to calculate out-of-plane field expansions from the mid-plane data have shown the advantages and drawbacks of the two investigated methods. On the one hand the traditionnal fitting method using an Enge+Fermi function shows a good stability as the calculation order increases, but some discrepancies appear due to the mixing of the two function (Enge & Fermi). Also, there is no radial dependance of the field included in the fit. On the other hand, the gaussian interpolation method

is able to reproduce the whole profile of the magnetic field, but this method is very sensitive to noise and other source of discontinuities in the mid-plane data used to calculate the out-of-plane expansion. Both methods will be used with the next set of data coming from the upcoming mapping campaign, as they provide a consistency test of the final transfer maps calculated with COSY.

References

1. M. Berz *et al.*, Phys. Rev. C **47** (1993) 537.
2. J. Caggiano, Contribution to this Annual Report: *S800 Dipole Magnetic Field Mapping Results.*
3. D. Bazin, Contribution to this Annual Report: *Methods for fringe field modeling - Application to the dipoles of the S800 spectrograph.*
4. J. Caggiano, Contributions to this Annual Report: *Software technique for processing S800 Dipole Magnetic Field Mapping & Automated Data acquisition system for S800 Dipole Magnetic Field Mapping.*

HEATLOAD STUDIES OF 400 AMP CURRENT LEADS CONDUCTED IN THE 50 LITER LIQUID HELIUM CRYOVESSEL

Jeff Schubert

In 1990 J.W. Kim *et al.* constructed a 50 liter liquid helium cryovessel with an access port for easy insertion of experiments. The port is set at a 45° angle, and the vessel may be tipped 45° in either direction so that current leads may be tested in any orientation from horizontal to vertical.[1] The heatload of the vessel with the access port blanked off was found to be less than 0.1 W once the gas cooled radiation shields reached their equilibrium temperatures. This heatload varies with the shield temperature, suggesting that it is dominated by radiation. The heatload has been observed to be below .03 W immediately after filling the vessel, when the shields are still much colder than their equilibrium temperature.[2]

The first practical use of the cryovessel was to test the prototype current lead the the Eight Tesla Magnet.[3] This current lead is actually a pair of 400 A gas cooled leads and a gas cooled set of eighteen signal wires all in a 1.59 cm diameter package. Although this lead design is only used in the vertical orientation in the Eight Tesla Magnet, it is very similar to the horizontal current lead in the Harper medical cyclotron.

Early boiloff runs were very time consuming and heat loads were inferred from a relatively small set of measurements. The 500 L dewar needed to be pressurized to 12 psig in order to transfer any liquid into the cryovessel, and even then most of a work day was required to fill the vessel. Because of the high transfer pressure 20% to 25% of the vessel's 50 L inventory would be lost to flashing immediately after removing the transfer line. The remaining helium was only sufficient for 12 hours of data-taking. During the past year we identified and corrected a vacuum leak in the transfer line and we replaced several meters of bare 3/8" diameter pipe in the helium return line with insulated 1/2" pipe. These improvements reduced the flow-impedance which in turn reduced the fill time to two hours with the 500 L dewar pressure at only 7 psig. In this regime it was convenient to reduce the pressure to 3 – 4 psig before removing the transfer line, and flashing losses were limited to the liquid above the highest point on the level sensor. It is now possible to make routine heatload measurements on the current lead for more than 20 hours at a time, two to three times per week, and we have already collected a great deal of data to aid in understanding the cryovessel and lead system.

With the 400 A current leads installed in the cryovessel, the total heatload is increased by an order of magnitude from the case where the port was sealed. The additional boiloff gas lowers the equilibrium temperature of the radiation shields, and the radiation heatload of the vessel should be somewhere in the .03 – .1 W range observed with the test port blanked off. Figure 1 shows the boiloff rate and shield temperatures as a function of time for the upright vessel with the lead tilted at a 45° angle, and no current flowing through the lead (the ohmic heating of the lead when energized is plotted in figure 2). Although current leads are rarely used in this orientation, the test provides a basis for comparison which is useful when separating phenomena related to the vessel from phenomena occurring in the lead.

The dip in the temperatures of both shields during the third hour is suspected to be an effect of the connection to the lab's recycling system. The fact that this feature is not reliably manifested in the boiloff rate curve, and the fact that the boiloff rate shows no trend despite the fact that the outer heat shield never reached equilibrium, suggests that the radiation heatload on the upright vessel is negligible compared to the conduction heatload of the current leads.

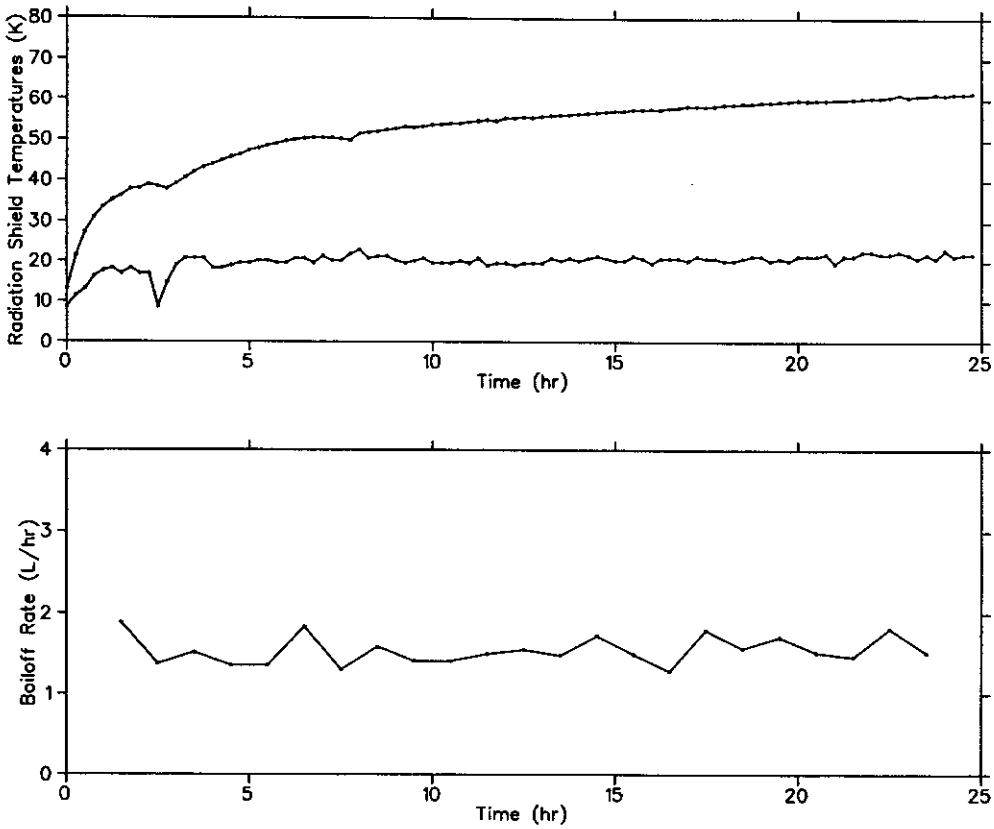

Figure 1: Radiation shield temperatures and heatload with a pair of 400 A current leads mounted in the test port, and no current in the leads. Pressure is controlled at 122 kPa (3 psig) to force roughly half of the boiled off gas through the leads. The rest cools the radiation shields.

The heatload of the current lead was tested in all three orientations. It was also useful to study the effect of coolant flow on the heat conduction through the lead. We find that for the 45° orientation and no current in the leads, the conduction heat load is minimized by a lead flow of 6 SCFH/lead. The equilibrium boiloff rates for all of the above conditions are listed in table 1. Where greater than one atmosphere of pressure was needed to force gas flow through the leads, the boiloff rates have been adjusted to an equivalent rate for the same heatload at one atmosphere. The high heatload for the horizontal lead is primarily due to the same counterflow convection that plagues horizontal vent tubes.[2] In addition, the gas flow through the lead dropped below the optimum flow after the vessel was tipped. The effect of the gas flow rate on the horizontal lead will be investigated in future experiments. The difference in heatload between the vertical and 45° orientation of the lead is believed to be an effect of the cryovessel itself. It is possible that tilting the vessel introduces an additional source of heat, which will require further experiments to identify.

References

1. J. Kim *et al.*, Cryovessel for the current leads test, *MSU-NSCL Ann. Report* 195 (1990).
2. J. Kim, Experiments with the liquid helium cryovessel, *MSU-NSCL Ann. Report* 201 (1992).
3. J. Kim, Eight tesla superconducting magnet for cyclotron studies, Ph.D. Thesis, MSU (1994).

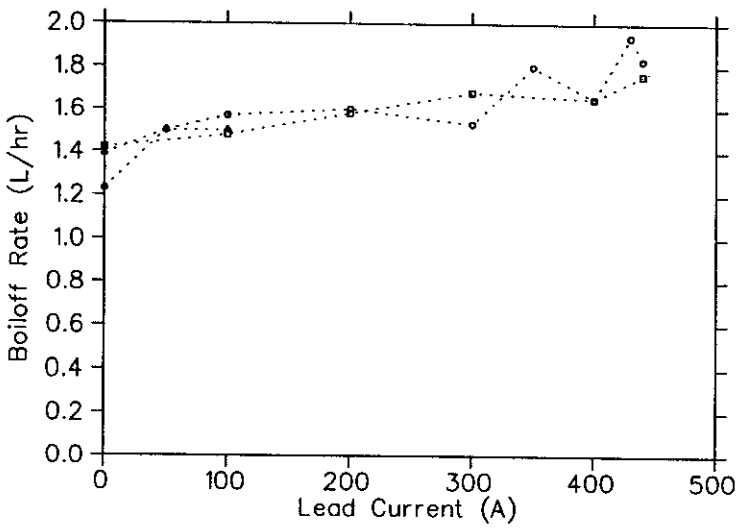

Figure 2: Heatload of vessel and lead with various currents in the leads. Each boiloff rate is the average over approximately one hour. The lead is in the 45° orientation.[2]

Table 1: Heatload due to a pair of 400 A current leads (in L/hr of boiloff)

	test port horizontal	test port at 45°	test port vertical
Optimally cooled lead	—	1.4	1.6
Overcooled lead	—	1.4	—
Suboptimally cooled lead	2.6	1.7	1.7-2.4

UPGRADES TO THE 4π DATA ACQUISITION SYSTEM

A.M. Vander Molen, R. Fox, and S. Hannuschke[a]

The 4π Data Acquisition System is based on a multinode Transputer processor farm[1]. The primary objective of its implementation was to supply a high data rate to tape as required by the 4π Detector Experimental program. The high rates come from the relatively large number of detectors signals, over 1400, and the relatively high event rate, up to 20 Kevents/sec [2]. Several factors contribute to limiting the data rates, including but not limited to, bytes/event, bus or link speed, computer speed, and recording device rates. The system before the current upgrade did improve the data rates over the previous system by offering a realtime filter option and improved link speeds. The data rates to tape were nominally raised from below 200 Kbytes/sec to over 300 Kbytes/sec or a 50% improvement in the experimental environment. Filtering also reduced the analysis time by reducing the volume of stored data. These rates were adequate but increasing the rates would allow for experiments, such as excitation functions over a large energy range, that were not practical given the available cyclotron beam time. To try and improve these rates a study was done of the system and the bottlenecks were identified and improvements were made where possible.

The frontend electronics produces data at over a Mbyte/sec. The transputer links can pass data up to 900 Kbytes/sec. Data rates, however, were well below this. Each subsystem was studied to identify and try to eliminate the bottlenecks. The first major problem identified was the link between then transputer farm and the SUN host system was not operating at the expected rates. Rewriting the software to take full advantage of the parallel architecture of the transputer reduced this problem. The next problem identified was the overhead associated with buffer handling. This problem was reduced by going to 16 Kbyte buffers from 8 Kbyte buffers. These improvements made the overhead associated with scaler reads a more pronounced effect. Increasing the default time interval for non taped scaler events reduced this effect. The scaler can be set at the beginning of each run and because of this higher scaler rates can still be used as needed for such things as beam tuning. These improvements inceased the data rates from nominally 300 plus Kbytes/sec. to over 500 Kbytes/sec. This required that the taping device be changed from a Exabyte 8500 8mm drive with a maximum write speed of 500 Kbytes/sec. to a DEC TK87 with a maximum write speed of 1000 Kbytes/sec. This change, incidentally, also reduced the analysis time. Finally, it was determined that the host system could not handle these improved rates. Rates without a load on the host would reach over 600 Kbytes/sec. but when taping and routing of data were added the data rates fell 5 to 10% for each function added. The expense associated with a new host system was determined not to be a practical investment at this time.

In conclusion the 4π Data Acquisition System's data rate was improved another 50%, allowing for a new set of experiments. Data rates to tape during an experiment will now run well over 500 Kbytes/sec. During one experiment where a filter was required data rates were over 700 Kbytes/sec. Note, because filtering reduces the data sent to the host the limitations of the host are reduced. Further improvements will probably be in the line of a new architecture to take advantage of new technologies.

a. Present address: Lufthansa Systems, gmbh., Kelstrbach, Germany

References

1. A. Vander Molen, R. Au, R. Fox, and S. Hannuschke, "A Transputer Based Parallel Processing Frontend Data Acquisition System," IEEE Trans. on Nuc. Sci. NS-41, No. 1, 80, Feb. 1994
2. A. Vander Molen, M.R. Maier, M. Robertson, and G.D. Westfall, "A fast data-bus to memory interface," Nuc. Inst. and Meth. A307 (1991) 116-118

DEVELOPMENT OF A BEAM SWEEPING DIPOLE

J. J. Kruse, A. Galonsky, C. Snow, J. Wang, and P. Zecher

The last several years have seen a great deal of effort invested in the understanding of neutron halo nuclei produced at radioactive beam facilities around the world. One such experiment involved the Coulomb dissociation of ^{11}Li into ^{9}Li and two neutrons. The measurement was kinematically complete; the energy and angle of each ^{11}Li beam particle was measured as it entered a lead target, and the energies and angles of each of the three decay products were measured after they left the target. These measurements allowed us to map the coulomb dissociation excitation function. The experiment proved successful, but before expanding this program to study other neutron halo nuclei, several upgrades have been made in the equipment used for the studies. The first improvement has been made in our neutron detection efficiency, through the development of the Neutron Walls. The second, the Beam Sweeping Dipole, is designed to reduce background events from reactions in the fragment detectors.

In the previous ^{11}Li experiment, the energy and the angle of each ^{9}Li fragment were measured by a three element charged particle telescope placed directly behind the target. The first element was a double sided silicon strip detector which was 300 μm thick. The strips on the detector provided a measurement of the fragment's angle, while the energy lost in the detector was used for particle identification in a ΔE - E plot. The second element of the telescope was a 300 μm silicon pin diode which provided additional ΔE information. Finally, the fragments were stopped in a CsI detector which measured the remaining energy of each particle. Unfortunately, only approximately one percent of the ^{11}Li particles reacted in the target, while a similar number were dissociated in the detector array. Many of the events produced in the array were indistinguishable from real target events, and so a large percentage of the beam time was used with no target in place to measure the magnitude of this effect. A dominant contribution to the width of our decay energy measurements was provided by the thickness (0.598g/cm^2) of the lead target, but to use a thinner target would cause our data to be overwhelmed by events originating in the detector stack. This provides the motivation for the development of a Beam Sweeping Dipole Magnet.

Our plan is to place the target at the entrance of a dipole magnet, so that in the case of a good event, the charged fragment will be swept through some angle to a detector array, while the neutrons leaving the target will travel straight through the field and arrive at the Neutron Walls, which are centered at zero degrees. All unreacted beam particles leaving the target will also be swept through an angle and arrive at the charged particle telescope. Neutrons produced by the dissociation of halo nuclei are largely forward focused, and so after being deflected by the magnet into the telescope, unreacted beam particles which react in the telescope will yield neutrons which miss the Neutron Wall array. Now that we no longer detect neutrons in coincidence with reactions in the telescope, this source of background has been eliminated and we can improve our decay energy resolution through the use of a thinner target.

The magnet is a former beamline dipole from the Bevalac at Lawrence Berkeley Laboratory. It is a room temperature C-shaped magnet whose pole faces measure 13x24 in^2. When we received the magnet, the vertical gap between the pole faces measured 6 inches, but has since been modified to 7.5 inches to increase the vertical opening angle for fragments and neutrons to leave the magnet. The field has been mapped in several planes, and in the midplane the peak field is more than 1.5 tesla. At full field strength, a ^{6}Li entering the magnet with an energy of 25 MeV/A will be deflected through more than 20 degrees.

In our next series of experiments, the target will be placed four inches upstream from the opening of the magnet. Six inches downstream from the target will be a pair of double sided strip

detectors 250 μm thick. These detectors, which are built with three sided frames, can be butted against each other for a continuous active area of 2 x 4 in^2. While they are thin enough that they will not produce a significant source of background events, the strip detectors will provide energy loss and angle information for the reaction fragments before they are significantly deflected by the magnetic field. 75 inches downstream from the target will be a plastic scintillator array to stop the fragments at the exit of the magnet. The array consists of 16 vertical scintillator bars 16 inches long. Each bar is two centimeters thick and 4 centimeters wide and has a two inch photomultiplier tube (PMT) glued to each end. The bars will be inside the vacuum, but the resistor chain for the PMT bases will be outside the vacuum to avoid gain shifts from resistive heating of the bases. Any other gain shifts will be monitored throughout the experiment by use of a pulsed LED system on the scintillators. The scintillators provide a measurement of the fragment's energy, and when used in conjunction with the strip detectors will give particle identification. The system produces measurements of ΔE, E, time of flight between the detectors, and magnetic rigidity of each fragment, which is enough to redundantly identify all fragments from the target. The back wall of the vacuum chamber through which neutrons will pass on their way to the Neutron Walls will be made of a light weight, high strength aluminum Hex-cell material, to provide minimal scattering of the neutrons between the target and the detectors. This system will be used in the summer of 1996 to make kinematically complete measurements of the coulomb dissociation of ^{6}He, ^{8}He, ^{11}Li, and ^{14}Be.

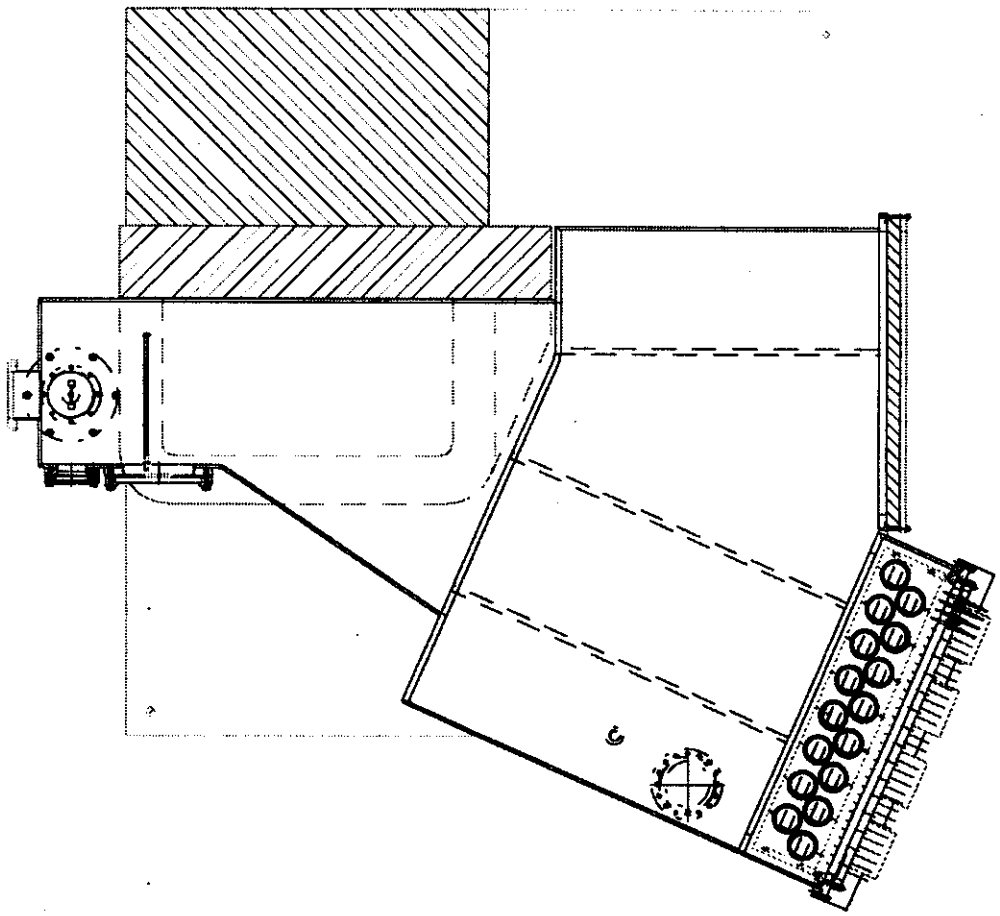

Figure 1: CAD drawing of the Beam Sweeping Dipole and vacuum chamber. The beam enters from the left and strikes the target located in the circular flange at left. The hatched region at top left represents the return yoke of the dipole and the dotted rectangles show the outlines of the coils. The strip detectors are located between the coils at left, and the phototubes for the scintillator array are shown at bottom right. The hatched region at top right represents the Hex-cell plate through which neutrons will pass on their way to the Neutron Walls.

CONSTRUCTION AND FIRST EXPERIMENT WITH A POSITION SENSITIVE PHOTON DETECTION ARRAY FOR IN–BEAM GAMMA RAY SPECTROSCOPY OF FAST MOVING RADIOACTIVE BEAMS

T. Glasmacher, H. Scheit, P. Thirolf, J. Brown, P.D. Cottle[a], M. Hellström[b], R. Ibbotson, K. Jewell[a], K. Kemper[a], D.J. Morrissey, P. Mantica, M. Steiner, and M. Thoennessen

For many years Coulomb excitation has been used to study low lying states in stable nuclei. In these experiments the incident beam energy was chosen to be below the Coulomb barrier to avoid excitations of the nuclei by the strong interaction. Stable enriched targets were bombarded with a heavy beam which excites low lying states in the target through exchange of a virtual photon. A real photon is emitted when the nucleus deexcites and can be detected in a high resolution photon detector. Alternatively, a particle beam of interest can impinge on and be stopped in a heavy target. In this case the emitted photon will be Doppler shifted and Doppler broadened; however due to the generally slow beam velocity these effects are small. In the case of exotic nuclei far from the valley of β-stability and with short lifetimes the fabrication of targets is not possible. Instead, one can produce radioactive beams of high isotopic purity with energies of several tens of MeV/A and bombard a heavy target. The projectile is excited in the Coulomb and strong fields of the target and deexcites from a bound state by emission of a discrete photon, thus establishing the existence and energy of this state. In the energy region of several tens of MeV/A the Coulomb excitation cross section can be much larger than the nuclear excitation cross section for small scattering angles. In cases where the nuclear excitation cross section is negligible (at forward angles) it is not only possible to measure the excitation energy of a state, but absolute cross section measurements of photon yields allow the determination of transition matrix elements. For example, the 2^+ state of the neutron-rich nucleus ^{32}Mg has recently been studied using a beam of ^{32}Mg at 50 MeV/A and a ^{208}Pb target at RIKEN [1]. The only other published intermediate energy Coulomb excitation experiment was a study of ^{11,12,14}Be nuclei at GANIL [2].

We have constructed and tested a high efficiency photon spectrometer to identify and measure the excitation energies of bound states in even-even nuclei far from the valley of stability. The A1200 fragment separator at the NSCL [3] is ideally suited to provide many different beams of exotic nuclei, at energies of several tens of MeV/nucleon. Our detector was designed such that measurements with beam intensities of about 1000 particles/second would typically yield sufficient statistics in a matter of hours. The detector has been successfully used with secondary beam intensities of as little as 10 particles/second. The higher beam velocity in intermediate energy Coulomb excitation experiments (a typical velocity is β=0.3c), compared to subbarrier Coulomb excitation experiments, results in large Doppler shifts and more Doppler broadening of the photo peaks. Therefore, the photon detection system requires good granularity to limit the Doppler broadening. In addition, the ideal detector should have a high photo peak efficiency in the energy region of 1-3 MeV (where most of the $2^+ \rightarrow g.s.$ transitions in even-even nuclei are located) and large geometrical coverage, since beams of the most exotic nuclei have low intensities. These considerations favor a compact array of NaI(Tl) scintillation detectors over non-position sensitive high purity germanium detectors. The intrinsic energy resolution of NaI crystals is comparable to the energy resolution due to Doppler broadening and a larger geometrical coverage is possible with NaI detectors as compared to high purity germanium (HPGe) detectors. Lastly, the cost of NaI crystals is much less than the cost of germanium crystals with similar efficiencies.

We have constructed an array of 42 position sensitive cylindrical NaI(Tl) detectors, each of which is read out by two phototubes. The energies and positions of the incident photons can be reconstructed from the two photomultiplier tube signals. The crystals are 18 cm long and 5.75 cm in diameter and arranged in three concentric rings around a 6 inch diameter beamline. The crystals were previously used in a PET imaging machine at Washington University in St. Louis. To shield the array from room background photons and to provide an environment with stable temperature the detector array is shielded by a 16.5 cm thick wall of low background lead on each side. Figure 1 shows a front and side view of the detector array, the support table and the lead shielding.

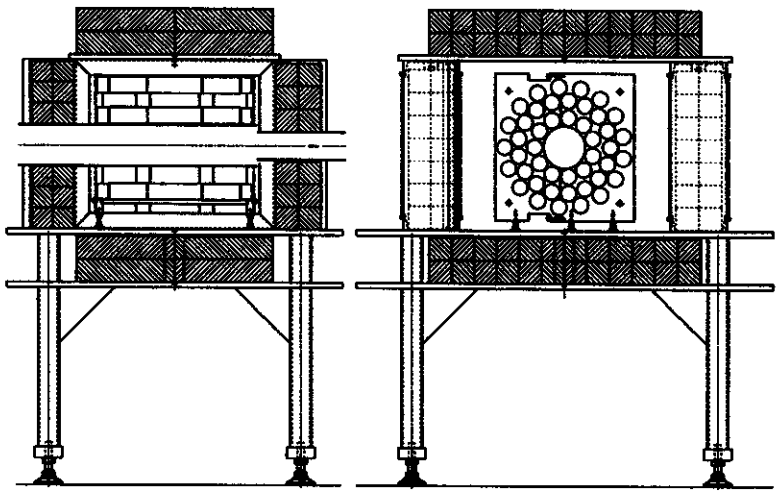

Figure 1: Mechanical setup of the NaI(Tl) detector array, the support structure and the lead shielding (hatched). In the left figure the beam moves from the right to the left, while figure on the right is looking in direction of the beam.

In the first experiment with a radioactive ion beam we detected the 1292 keV photons emitted from the known ($2^+ \rightarrow g.s.$) transition in ^{38}S. A beam of ^{40}Ar was fragmented in the A1200 fragment separator and a 40 MeV/nucleon beam of ^{38}S ions impinged on a 200 mg/cm^2 gold target located in the middle of the NaI array. The ^{38}S ions were positively identified by a time of flight measurement before interacting with the target. Fragments scattered into a lab angle of less than 4° were detected in a fast/slow plastic phoswich detector located downstream from the secondary target. The energy loss - total energy measurement allowed the rejection of events which lead to the breakup of the projectile in the target. Photons were measured in coincidence with beam particles. The photons emitted from the excited projectile can be clearly distinguished from photons coming from the target by their Doppler shift and Doppler broadening. One dimensional projections onto the energy axes are shown in figure 2. In the laboratory frame the line corresponding to the ($7/2^+ \rightarrow g.s.$) transition in ^{197}Au is clearly visible, while the photons corresponding to the transition in ^{32}S are Doppler shifted and do not form a peak. Only after transforming the energies into the projectile frame does the photopeak become visible. In figure 3 we show the energy of the detected photon (in the laboratory frame) versus the position at which it interacted in the crystal. We also show energies after being shifted into the projectile frame versus their position.

We thank Professor Lee Sobotka, who salvaged the NaI(Tl) detectors and made them available to us.

a. Department of Physics, Florida State University, Tallahassee, Florida 32306.
b. Gesellschaft für Schwerionenforschung, D-64220 Darmstadt, Germany.

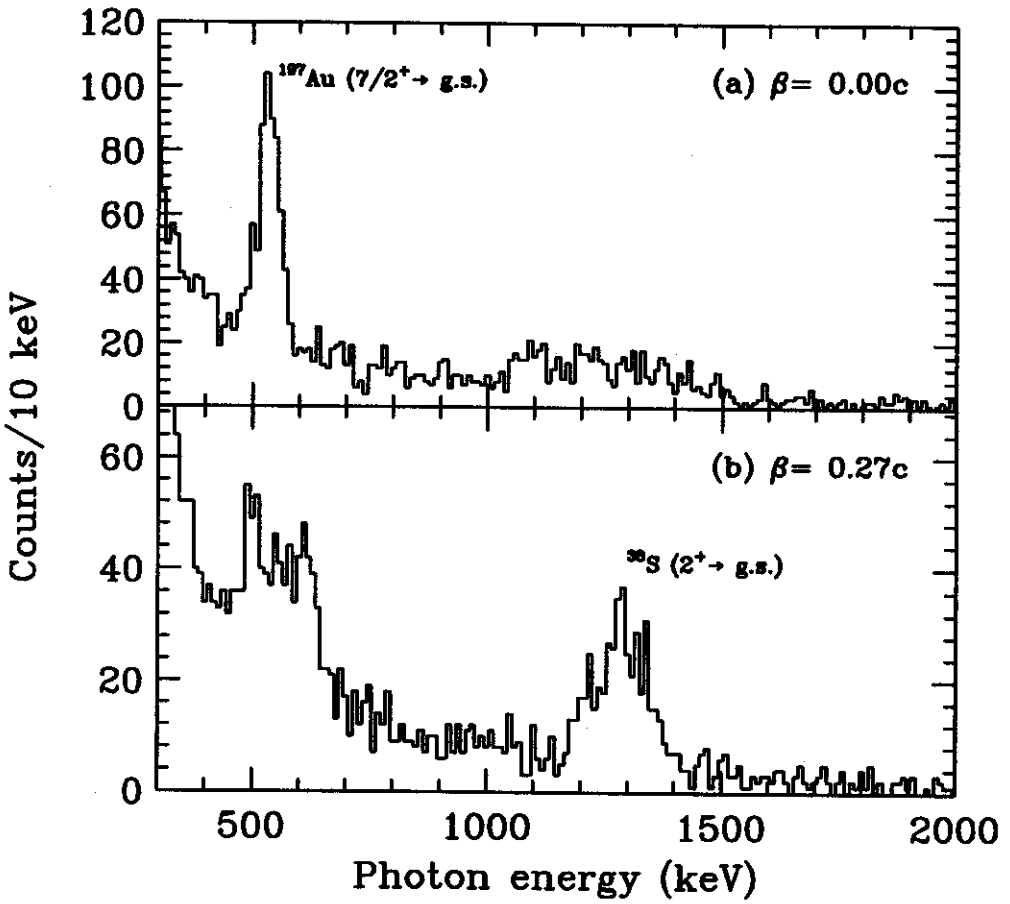

Figure 2: Observed photon energies without Doppler correction (top panel). The 545 keV ($7/2^+ \rightarrow g.s.$) transition in the gold target is visible as a peak, while the 1292 keV ($2^+ \rightarrow 0^+$) transition in ^{38}S is very broad. After shifting the data into the projectile frame (bottom panel) the photopeak of the transition in ^{38}S becomes visible and the gold peak broadens.

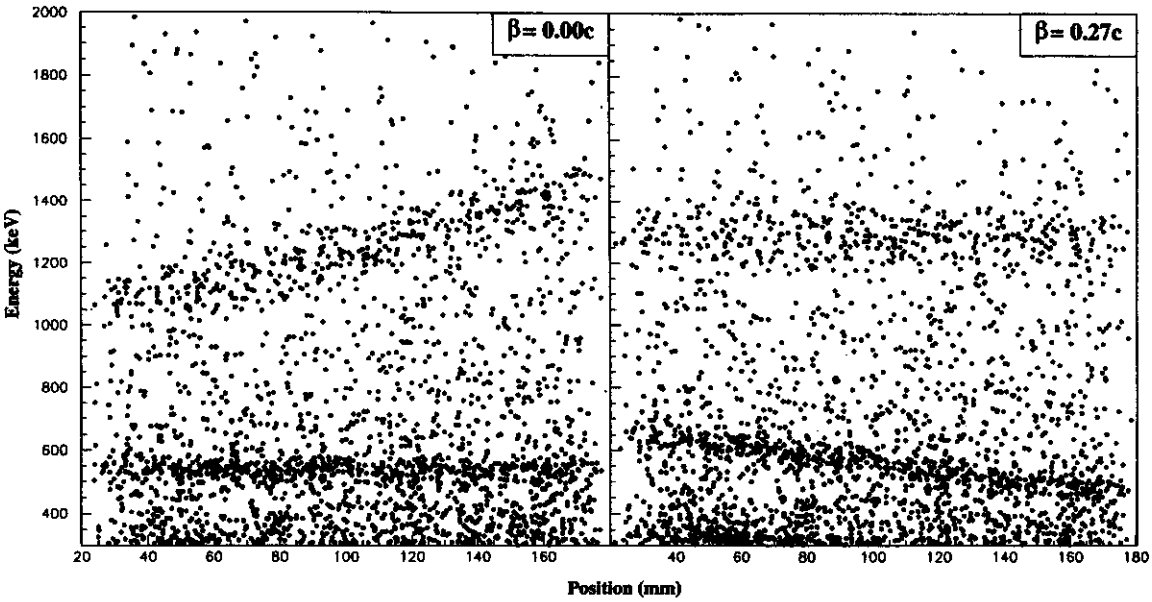

Figure 3: Observed photon energies plotted versus position in the NaI(Tl) detector array for the reaction $^{38}S+^{197}Au$ at 40 MeV/A. The target was located perpendicular to the midpoint (90 mm) of the detector. The left panel shows the energies measured in the laboratory frame. Photons emitted from the stationary target (545 keV) are in the proper restframe and their energy is independent of position. The right panel shows the same data after being shifted into the projectile frame ($\beta = 0.27c$).

References

1. T. Motobayashi *et al.*, Phys. Lett. B 346, 9 (1995).
2. R. Anne *et al.*, Z. Phys. A 352, 397 (1995).
3. B.M. Sherrill *et al.*, Nucl. Instr. Methods B56, 1106 (1991).

NEUTRON CROSS-TALK IN THE NEUTRON WALLS

J. Wang, F. Deák[a], A. Galonsky, Á. Horváth[a], K. Ieki[b], Y. Iwata[b], Á. Kiss[a], J. Kruse, Z. Seres[c], P. Zecher

The neutron walls [1,2] were built in early 1995 to improve the neutron detection system used in a 1991 experiment [3] in which ^{11}Li breakup was studied by measuring the complete kinematics of the ^{9}Li fragment and two neutrons. When the measurement has two neutrons in the final state of a reaction, we have to deal with neutron cross-talk.

Cross-talk occurs when one neutron is detected in two different detectors. A cross-talk event can look just like a real two-neutron event. Sometimes more than 30% of the two-detector events can be cross-talk events [4,5]. There are two negative effects of cross-talk: (1) causing overestimation of neutron coincidences, (2) distorting the directional correlation of the two neutrons. In order to avoid these negative effects and come to a reliable conclusion, we have to identify and reject as many cross-talk events as possible.

Detection of a neutron relies on its interactions with hydrogen and carbon in a scintillator. For E_n~25 MeV, elastic scattering on hydrogen is the major contribution to the detection efficiency [6] and, therefore, of cross-talk. That is convenient because the well known two-body kinematics then becomes our basis for neutron cross-talk identification.

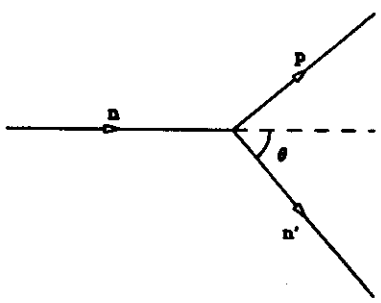

Fig. 1. The two-body kinematics of n-p elastic scattering. Two equations result from energy and momentum conservation, (1) $E_{n'} = E_n - E_p$, (2) $E_{n'} = E_n\cos^2\theta$.

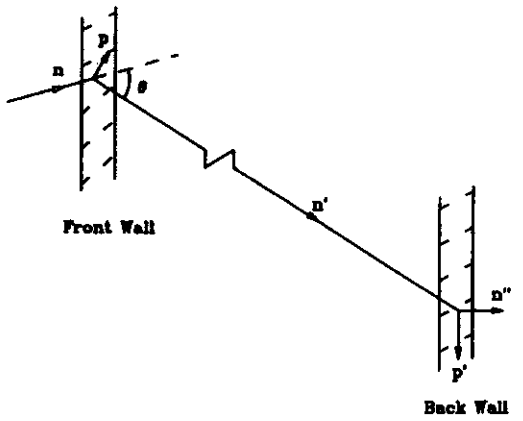

Fig. 2. An example of cross-talk between the front wall and the back wall. The neutron makes one signal in a cell of the front wall and another signal in a cell of the back wall. Both scatterings follow the two-body kinematics shown in Fig. 1.

In Fig. 1, E_n is the incident neutron energy, E_n' is the scattered neutron's energy, E_p is the recoil proton's energy and θ is the neutron's scattering angle. Energy and momentum conservation give these two relations:

$$(1)\ E_n' = E_n - E_p \qquad (2)\ E_n' = E_n \times \cos^2\theta.$$

If E_n and E_p are known, E_n' and $\cos\theta$ can be determined. It is the two-body kinematics that results in special properties of a cross-talk event as compared to a real two-neutron event.

The neutron walls are usually set next to each other in an experiment. The one close to the target is called the front wall. The one behind the front wall is called the back wall. Figure 2 shows a typical cross-talk event between the front wall and the back wall. For each detected scattering, we

measure the incoming neutron's energy, E_n, from its time of flight, the light output of the recoil proton, L_p, and the position of the scattering, (x,y). The recoil proton's energy E_p is extracted from the L_p value using the proton light response function [7]. After E_n and E_p for the first scattering are determined, we can get the scattered neutron's energy by using eq. (1). Then the cosine of the scattering angle θ can be predicted by using eq. (2): $(COS\theta)_p = (E_n'/E_n)^{1/2} = [(E_n-E_p)/E_n]^{1/2}$ if it is a cross-talk event. On the other hand, from geometry we measure $(COS\theta)_m$ by using the positions of the two scatterings, one in the front wall, the other in the back wall. $(COS\theta)_p$ should equal $(COS\theta)_m$ for cross-talk events since they follow the two-body kinematics. If we plot $(COS\theta)_p-(COS\theta)_m$ for cross-talk events, the distribution should be centered at zero with a spread caused by the uncertainty in measuring the two neutron energies and the two positions. For real two-neutron events, two neutrons from the source are detected. The $(COS\theta)_p-(COS\theta)_m$ distribution won't form a peak at zero. It should cover the range allowed by the geometry of the neutron walls.

The second characteristic of cross-talk also comes from the two-body kinematics. v_n', the velocity of the scattered neutron can be calculated after E_n' is determined from E_n and E_p. The positions of the first and second scatterings give the distance between the two scatterings, L_{12}. Then we can obtain the predicted time of fight: $(TOF)_p = L_{12}/v_n'$. Again, the time of flight between the two scatterings is measured in the experiment to give $(TOF)_m=T_2-T_1$. For cross-talk events, $(TOF)_p-(TOF)_m$ should be zero. Due to measurement uncertainties, the peak at zero in the $(TOF)_p-(TOF)_m$ distribution has a width. However, this distribution should be random for real two-neutron events.

A Monte-Carlo program [6] was written to simulate cross-talk. In order to check the program, a test experiment was performed using the ^{7}Li(p, n) reaction. In this experiment, all the two-neutron events are cross-talk events. The first neutron wall, the center of which was at 35° relative to the beam line, was put 5 m from the ^{7}Li target. The second neutron wall was 1 m behind the first one. Neutrons were produced by bombarding a 0.5 mm ^{7}Li target with 29.8 MeV protons. Forty of the 50 cells were used in the experiment, but only the data of 20 cells were analyzed due to a problem with the pulse-shape circuitry for the other 20 cells. Of the 20 analyzed cells, there were 8 cells in the front wall from no. 5 to no. 12 if counted from the bottom of the wall and 12 cells in the back wall from no. 9 to no. 20.

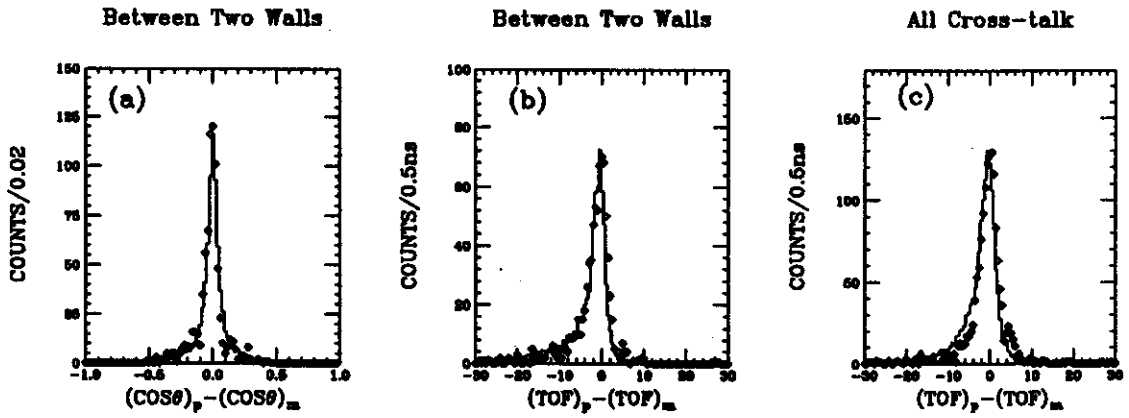

Fig. 3. The cross-talk distributions in ^{7}Li(p,n) reaction experiment. The experimental data are given by open symbols. The histograms are the results of our simulation. (a) $(COS\theta)_p-(COS\theta)_m$ distribution for the cross-talk events between the two walls. (b) $(TOF)_p-(TOF)_m$ distribution for the same events in (a). (c) $(TOF)_p-(TOF)_m$ distribution for all the cross-talk events.

The results are presented in Fig. 3. The open symbols represent the experimental data. The histograms, scaled to fit the experimental data, are the results of our Monte-Carlo simulation [6]. Plot (a) gives the $(COS\theta)_p$–$(COS)_m$ distribution for the cross-talk events between the two walls. Plot (b) gives the $(TOF)_p$–$(TOF)_m$ distribution for the same events in plot (a). Plot (c) gives the $(TOF)_p$–$(TOF)_m$ distribution for all the cross-talk events, including those within one wall. As predicted, all the cross-talk distributions peak at zero. The discrepancy in plot (c) is from the events within one wall; it is being studied.

a. Present address: Department of Atomic Physics, Eötvös University, Puskin utca 5-7, H-1088 Budapest 8, Hungary.
b. Present address: Department of Physics, Rikkyo University, 3 Nishi-ikebukuro, Toshima, Tokyo 171, Japan.
c. Present address: KFKI Research Institute for Particle and Nuclear Physics of the Hungarian Academy of Sciences, H-1525 Budapest 114, Hungary.

Reference

1. P. Zecher, et al., NSCL Annual Report, 1993.
2. P. Zecher, et al., NSCL Annual Report, 1994.
3. D. Sackett, et al., Physical Review C 48, 118 (1993).
4. P. Désesquelles et al., Nucl. Instr. and Meth. A307, 366 (1991).
5. A. V. Kuznetsov et al., Nucl. Instr. and Meth. A346, 259 (1994).
6. J. Wang, et al., paper to be sent to Nucl. Instr. and Meth..
7. V. V. Verbinski et al., Nucl. Instr. and Meth. 65, 8 (1968).

FABRICATION OF THIN SCINTILLATOR FOILS

L.W. Weathers and M.B. Tsang

In the past few years, 4 mg/cm^2 (40μm) scintillator foils have been fabricated regularly at the National Superconducting Cyclotron Laboratory. They are mainly used in the Miniball/Miniwall array, a 4π low threshold charge particle array used in many intermediate energy heavy ion experiments [1,2]. The procedure used in fabricating these foils is described here. In order to facilitate mass production of foils reliably, we have determined the relationship between the viscosity of the scintillator solution, the speed of the rotating surface and the thickness of the resulting film. Each of the foils produced with the current method typically has an area of 7x7 cm^2. Each foil is highly uniform to within 2%. Each foil is self supporting without the need of a mylar substrate. Even though most of the foils produced are about 4 mg/cm^2 thick, foils within the range of 1-8 mg/cm^2 with same quality can be fabricated.

The scintillator foil is spun using a solution of Betapaint, BC-498X plastic scintillator dissolved in xylene. Typically, a 40% by weight solution is purchased from the Bicron Corporation, Newbury, Ohio. This commercially available solution is then diluted with xylene to a solution with the appropriate viscosity, depending on the thickness of the foils desired. To standardize the viscosity measurements, Cannon-Fenske 500 viscometers, calibrated at 40° C, are used in the present work. Figure 1 shows the relationship between the viscosity (v) of the BC-498X solution as a function of the percentage of plastic scintillator by weight (W). The data points in Figure 1 can be best fit by the relationship

$$v = 2.72 \times 10^{-8} W^{6.22} \qquad (1)$$

Previous work has shown a relationship between the thickness and the angular speed used in spinning [1]. Unfortunately very few data points were taken thus a general quantitative relationship between the viscosity, angular speed and thickness could not be obtained. In the present study, we obtained a large number of data points from solutions with viscosities between 10-60 poise. Each solution was spun at various speeds to obtain foils with different thicknesses. Figure 2 shows the experimental relationship between the thickness of the foil and the spinner angular velocity. For a solution with a fixed viscosity, the experimental relationship between the foil thickness (t) in mg/cm^2 and angular speed (ω) of the spinner in rpm follows the power law [1]

$$t = k(v)\, \omega^{-0.61} \quad ; \qquad (2)$$

$$k(v) = \exp(3.49\, v^{0.11}). \qquad (3)$$

Contrary to ref. 1, only one exponent of -0.61 for the angular velocity (ω) is needed to fit all the data in Fig. 2. At low viscosity (<10 poise), k(v) deviates slightly from Eq. 3. Much lower rotational speeds than that discussed in reference [3] are used since lower angular speeds allow better control of the spinning process resulting in more reproducible fabrication of the foils.

Equation 1 or Figure 1 can be used reliably to prepare a solution of the desired viscosity. The solution must be thoroughly mixed with a magnetic stirrer, and left undisturbed overnight to remove any bubbles introduced in the mixing process. The viscosity is very sensitive to the exact amount of xylene solution used in diluting the scintillator solution or the amount of xylene lost due to evaporation. It must be measured accurately just prior to spinning. Since spinning is done at room temperature, which is not accurately controlled, the constants used in Equations 2 and 3 may change slightly. The optimum speed should be determined by spinning a couple foils at various speeds.

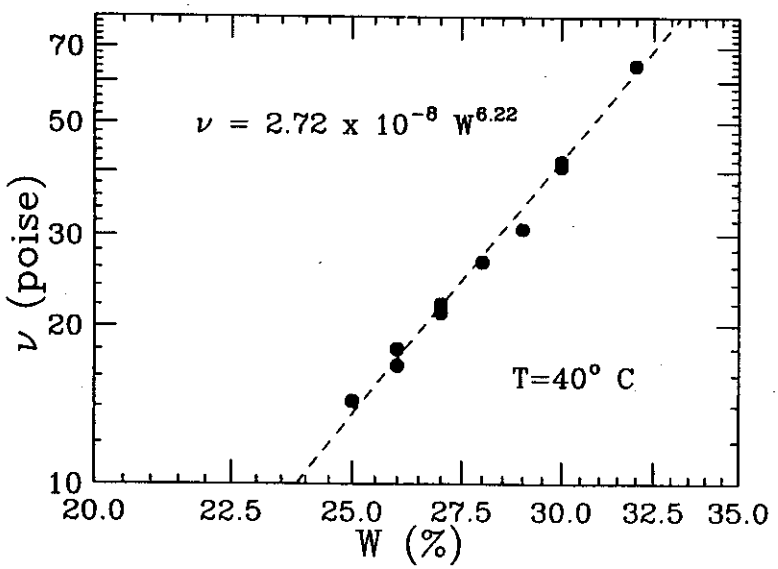

Fig. 1: The viscosity (ν) of the BC-498X solution as a function of the percentage of plastic scintillator by weight (W)

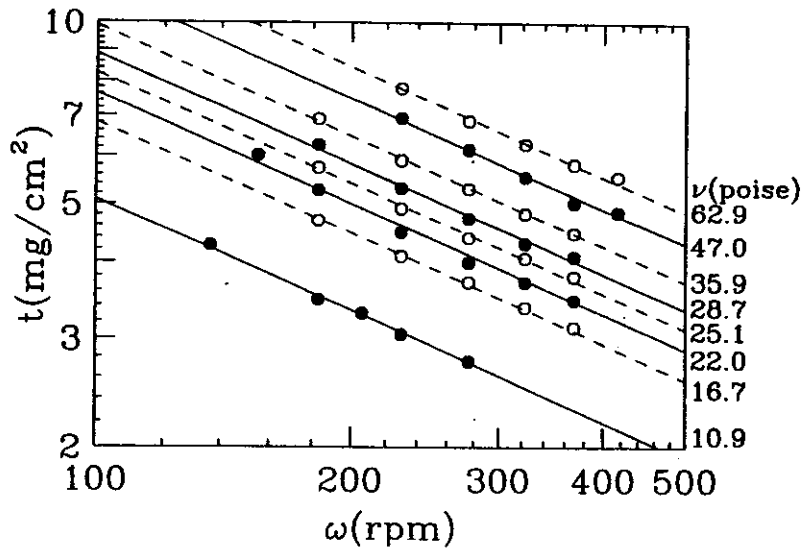

Figure 2: The experimental relationship between the thickness of the foil and the spinner angular velocity

Approximately 7 cc of the solution is poured onto the center of a 23 cm glass plate which is mounted on a spinner (a horizontal disk attached to an electrical motor drive). To facilitate eventual removal of the foil from the glass plate, the plate must be thoroughly cleaned with ethanol and distilled water before applying a final coating of Teepol 610 which acts as a releasing agent. After spinning the scintillator solution for 4 minutes, the plate is removed from the spinner and stored in a flow of dry nitrogen until completely dry (about 2 days). Once dry, the foil can be peeled from the glass plate.

Uniformity of these foils is determined by scanning each foil in vacuum using 8.78 MeV alpha particles from a collimated ^{228}Th sources. The thickness of the foil can be determined from energy loss of alpha particles [4] as well as by weight. Typically, the thickness of most foils are uniform to better than 2%.

Before large quantities of foils are produced, a foil with thickness greater than 4 mg/cm^2 is made from each bottle of the purchased Beta paint. The quality of the Betapaint is monitored by measuring

the light output of this foil using 5.48 MeV alpha particles from a collimated ^{241}Am source which will stop in a 4 mg/ cm^2 foil. The light output of these foils typically is 30-40% of the light output of a 23cc anthracene crystal.

References

1. R. T. De Souza et al., Nucl. Instr. and Meth. A295 (1990) 109.
2. G. F. Peaslee, Phys. Rev. C. 49 (1994) 2271.
3. E. Norbeck, T. P. Dubbs and L. G. Sobotka, Nucl. Instr. and Meth. A262 (1987) 546.
4. U. Littmark and J. F. Ziegler, Handbook of Range Distributions for Energetic Ions in All Elements, vol. 6 of The Stopping and Ranges of Ions in Matter, ed. J. F. Ziegler (Pergamon, New York, 1980).

FABRICATION OF THIN POLYETHYLENE FOILS

C. F. Powell, D. J. Morrissey, P. Askeland[a], J. A. Brown, and M. Steiner.

The preparation of thin foils for use as target materials is an important technique in experimental nuclear physics. Targets must be of uniform thickness, and thin enough to minimize energy straggling. In some instances targets must have a large area, and in the case of isotopically enriched targets, must be manufactured with efficient use of expensive raw materials. A recent effort to produce thin polyethylene targets at the NSCL was motivated by the desire to use ^{13}C as the target nucleus in reaction studies using radioactive nuclear beams. Enriched polyethylene (in either ^{13}C or deuterium) is commercially available from several sources, and the raw material can be fashioned into target quality films. We describe a technique developed to prepare thin foils of polyethylene meeting the above criteria.

The first succesful method used at the NSCL for fabrication of polyethylene foils is described in [1]. This technique used several stages of melting under vacuum to remove trapped air from the sample, then the sample was clamped between two heated blocks of steel. The technique was able to produce foils with thickness as small as ~40 μm (~4 mg/cm^2 polyethylene), but the uniformity was difficult to control and a minimum of 24 hours was required to produce a single foil.

Another technique developed previously to produce polyethylene foils is described in [2]. This method involves dissolving the polyethylene in xylene, pouring onto a glass plate, and heating to drive off the xylene, leaving a film of polyethylene behind. This technique was reported to produce films down to a thickness of ~10 μm (~1 mg/cm^2 polyethylene), but attempts at the NSCL failed to produce a target of acceptable quality.

Our most successful method to date to produce thin foils of polyethylene involves forming the target using a heated hydraulic press (Carver Model 2112). The raw material (~200 mg for a 30 μm target of ~10 cm^2) is placed between two pieces of highly polished steel, with brass shim stock used as a spacer between the plates to set the desired target thickness. The plates are placed in the heated press and compressed under 15,000 lbs of force at 250°F for three minutes. The heat and high pressure consistently produce foils of high quality in a very short period of time. Thicknesses as small as 30 μm (~3 mg/cm^2 polyethylene) and thickness uniformity of 3% FWHM over an area of 10 cm^2 have been prouced.

The choice of raw material is important for target fabrication. Enriched polyethylene can be purchased in either low or high-density forms. High-density polyethylene is much more rigid and has a higher melting point (>300°F), which led to difficulty in constructing quality targets. Enriched polyethylene obtained from ISOTEC, Inc. proved to be very suitable for target fabrication. The fine powder produced foils without problems caused by air inclusion.

a. Department of Chemistry, Michigan State University, East Lansing, MI 48824

References

1. M. Steiner, Ph.D. Thesis, MSU (1995)
2. W. Z. Liu, Ph.D. Thesis, University of Michigan (1991)

A SEARCH TECHNIQUE FOR γ-RAY BANDS USING SEGMENTED FFT ANALYSIS

C. V. Hampton, W. A. Olivier, Wm. C. McHarris

A band-locator technique employing Fourier spectrum analysis has been developed for γ-ray spectra. This is a purely mathematical routine based on superdeformed, hyperdeformed and normal rotational band frequency-space descriptions. The *Principle of Superposition* describes how any waveform can be unfolded into the summation of simpler parts based on linear combinations of harmonic multiples of the fundamental frequency. The mathematical technique that we employ here is dubbed a segmented FFT routine because only a small (5-19%) but very select fraction of the frequencies contained within the original spectrum are transformed back into energy space to reconstitute the band that is being sought.

An ordinary γ-ray spectrum can be unfolded by converting the energy spectrum into frequency space, then re-transforming sequential frequency-segments. The total spectrum can be separated into various, recognizable parts: discrete peaks, background profile, and noise. [1] By employing this same methodology on incrementally smaller frequency segments, it became obvious that within frequency space there are unique characteristics inherent in each type of band which, when re-transformed into energy space, can reconstitute the original peaks. In other words, the discrete peaks contained within the spectrum that are inter-related through a specific rotational band can be separated from all other discrete peaks since each rotational band exists as a unique mathematical function. [2] As an example,

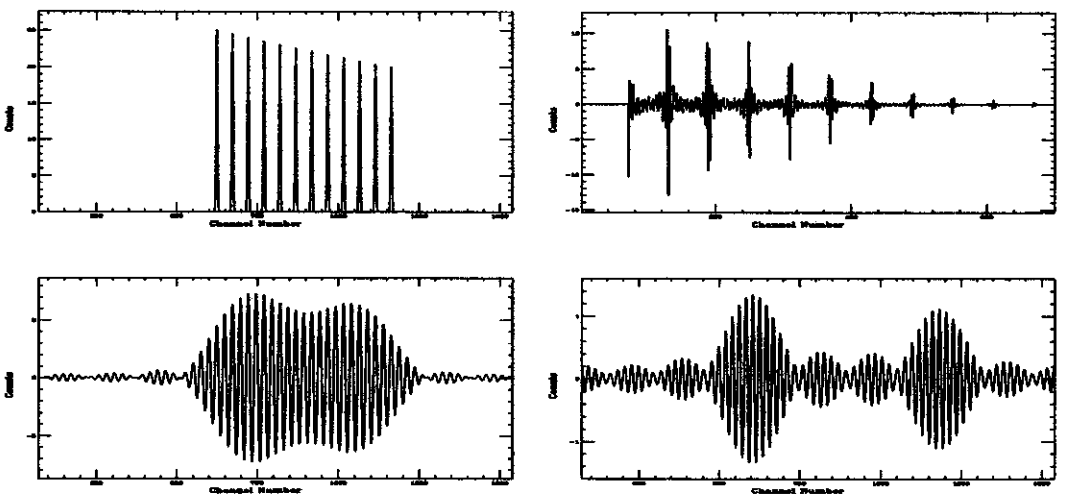

Figure 1: Spectrum synthesis in frequency space. (clockwise) The SD rigid rotor, twelve component band in a) energy space can be transformed into b) frequency space. By selecting frequency regions in b) that correspond to peak maxima or valleys and then re-transforming these small frequency region segments into energy space, only two distinct spectrum shapes result. c) An energy spectrum corresponding to a frequency space, valley segment and d) one corresponding to a peak maximum segment.

Fig.1 shows a reconstruction in frequency space of a computer-generated, rigid rotor, twelve component superdeformed (SD) band. The SD band shown in energy space in Fig.1a is transformed into frequency space in Fig.1b. By selecting frequency regions in Fig.1b that correspond to either peak maxima or valleys

and then re-transforming these small frequency region segments into energy space, only two distinct types of spectral shapes result. Fig.1c corresponds to a representative valley segment and Fig.1d corresponds to one peak-maximum segment. By summing all of the energy segments in Fig.1c that belong to the frequencies at the peak maxima, the original SD band can be reconstructed.

A signal to noise intensity study was conducted to determine the lowest signal intensity that a band would need in order to be detected by the method. Fig.2-top shows a computer-generated test spectrum in energy space that contains the SD rigid rotor band plus random-generated noise in a 1 to 3 intensity ratio. By re-transforming eleven frequency-segments in a six-channel window over the peak maximum (corresponding to approximately 5% of the total frequencies), a significant regeneration of the SD band results (see Fig.2-Bottom). The 'shape' of the resulting band depends upon the number and size of the frequency segments chosen for re-transformation. The higher the number of segments, the more recognizable the band 'shape'. However, higher numbers for the frequency segment window also admit frequencies from other bands. A balance between recognizable 'shape' and interferring bands needs to be maintained. Clearly, a band with a S/N of much less than 1 to 1 can be located with this method. Noise has no detrimental effect on locating SD bands, even if the bands are not observable in energy space.

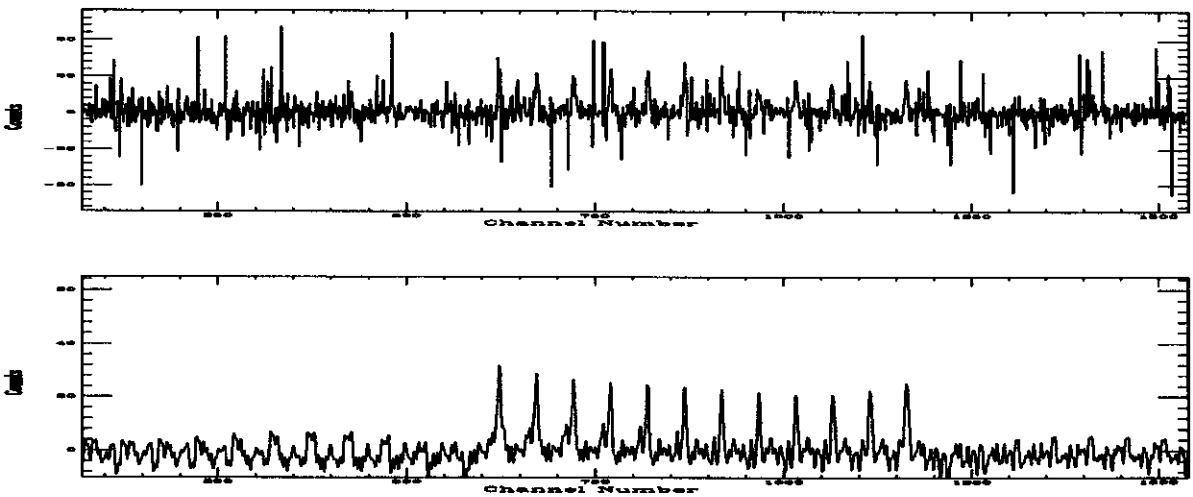

Figure 2: S/N intensity study. Top) The energy space spectrum contains the SD rigid rotor band plus computer generated noise in a 1 to 3 intensity ratio. Bottom) Re-transforming 5% of the total frequencies results in a regeneration of the SD band.

A study was performed to determine the effect of the presence of other rotational bands on locating the SD band. A multicomponent, computer-generated test spectrum was constructed using a) the SD band, b) noise at the intensity of the SD band and c) a normal rotational band with backbending. Some of the peaks within the backbending region overlapped with some SD peaks within energy space. The intensity of these interferring peaks was at least twice that of the SD peaks. Fig.3-top shows the test data spectrum in energy space. A re-transformation of segmented frequencies into energy space reconstitutes the SD band even in the presence of interferring peaks (see Fig.3-bottom). Approximately, 5% of the total frequencies were back transformed. In order to remove the harmonic contributions from the many components of the spectrum, the valley segments from the standard were added into the sum of the data segments.

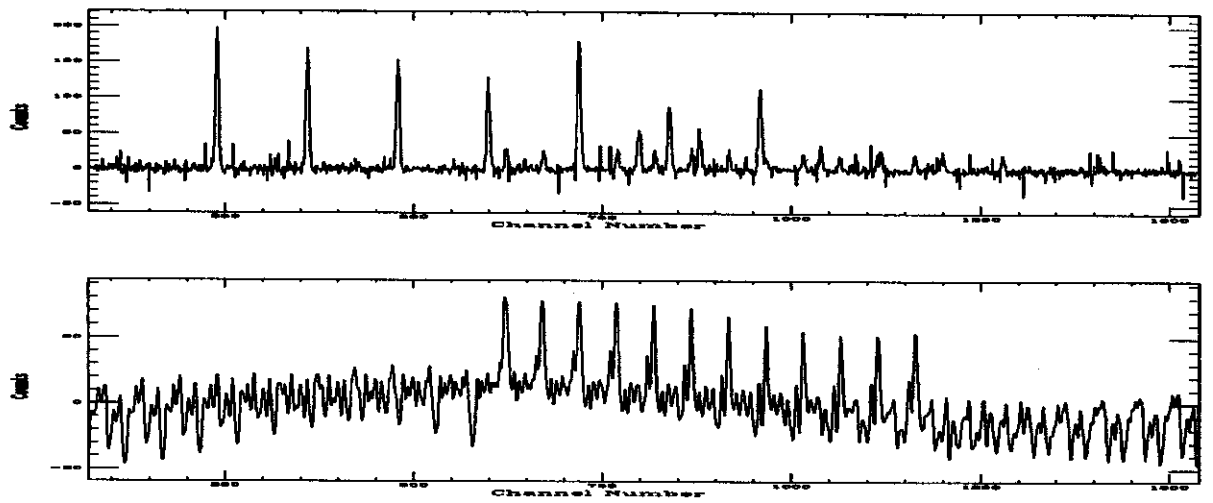

Figure 3: Top) Multicomponent test spectrum in energy space. Bottom) A re-transformation of segmented frequencies into energy space reconstitutes the SD band even in the presence of overlapping peaks in energy space.

SUMMARY

Initially, a 'standard' band with which to search is generated from a bandhead spin and rotational constant using the rigid rotor approximation formula: $E_\gamma = E_{I+2} - E_I = A(4I+6)$ where, $E_I = AI(I+1)$. The band rotational constant is A. The spin is I. For an SD band, $A = E_\gamma/[(4 \times I_{est}) + 6]$ where I_{est} is the estimated bandhead spin. The E_γ is the lowest observed energy. For a normal deformed band, the rotational constant is entered directly, not calculated. The peak shape is then designed, matching the statistical information from the actual data peaks for FWHM variation, relative peak height and calibration.

Conversion of the band into frequency space provides a pattern, segments, of which, can act as a template to be extracted from the frequency spectrum of the original data set. Peak maxima of the standard band in frequency space provide a window for the segments. These segments are then re-transformed into energy space and summed. The process is repeated with the original data set. The summed, segmented FFT spectra from both the standard band and the data are masked to eliminate spurious harmonic contributions by adding in the standard valley segments. The masked spectra are then compared to determine the probability of the search result. When confronted with a complete unknown, the presence of these segmented band frequencies provides useful information in locating the band.

This search routine has been designed to be part of a modified *DAM* program from the ORNL users-software. The Fast Fourier Transform is part of the package from *IMSL*, Inc.

References

1. C.V. Hampton, B. Lian, Wm. C. McHarris, "Fast-Fourier-Transform Spectral Enhancement Techniques for γ-ray Spectroscopy", Nucl. Instr. and Meth. in Phys. Res. A 353, 280 (1994).
2. C.V. Hampton, W.A. Olivier, Wm. C. McHarris, "A Search Technique for γ-ray Bands Using Segmented Fourier Analysis ", presented at the Workshop on Data Analysis, Joint Institute for Heavy Ion Research, ORNL, February 7-10, 1996.